Universität Hamburg
DER FORSCHUNG | DER LEHRE | DER BILDUNG

Applications of Test Masses in Uniform Circular Motion to Detect Millihertz Gravitational Waves

by

Suvrat Rajkumar Rao

A Dissertation
Submitted to the Department of Physics
Faculty of Mathematics, Informatics and Natural Sciences
University of Hamburg
For the degree of Doctor of Science

April 21, 2024

Reviewers of the dissertation:	Prof. Dr. Jochen Liske Prof. Dr. Marcus Brüggen
Members of the examination committee:	Prof. Dr. Jochen Liske Prof. Dr. Marcus Brüggen Prof. Dr. Stephan Rosswog Prof. Dr. Oliver Gerberding Prof. Dr. Günter H. W. Sigl
Chair of the examination committee:	Prof. Dr. Günter H. W. Sigl
Date of the oral defense:	14.06.2024
Chair of the Physics Doctoral Committee:	Prof. Dr. Markus Drescher
Head of the Physics Department:	Prof. Dr. Wolfgang J. Parak
Dean of the MIN Faculty:	Prof. Dr.-Ing. Norbert Ritter

Abstract

In this doctoral dissertation, starting from the first principles of the general theory of relativity, the geodesic deviation of test masses in uniform circular motion is calculated, due to the passage of gravitational waves (GWs) from astrophysical sources. The results of this theoretical analysis are used to conceive of experimental setups that could utilize this principle to detect GWs. These setups are based on, but are not limited by, the current status of technology. Mainly, circular particle accelerators in the mode of storage rings are considered. The major sources of noise for a storage ring gravitational wave observatory (SRGO) are explored, and basic noise estimates are made based on the specifications of existing facilities such as the Large Hadron Collider (LHC). A major part of the dissertation consists of numerical simulations of toy models of an SRGO. The response signal of the GW detector is explored as a function of various model parameters. Errors on estimating the model parameters are found using Markov Chain Monte Carlo (MCMC) methods applied to artificially generated data with added noise. It is shown that an ideal version of such a detector would be sensitive to millihertz GWs by design, and would be able to single-handedly obtain accurate constraints on the GW source parameters. An attempt has been made to incorporate as much physics as currently possible, which covers the essential aspects of reality without over-complicating the models for a first study of this novel experiment concept. The overall focus has been to establish a strong conceptual foundation, to obtain robust qualitative conclusions, and to make order-of-magnitude estimates. Comparisons with the theory and practices of existing GW detectors have been made throughout. Wherever possible, the results are presented in the conventions followed by the GW community at the time of writing this dissertation.

Abstract

In dieser Dissertation wird, ausgehend von den ersten Prinzipien der allgemeinen Relativitätstheorie, die geodätische Abweichung von Testmassen in gleichförmiger Kreisbewegung berechnet, die auf den Durchgang von Gravitationswellen (GW) aus astrophysikalischen Quellen zurückzuführen ist. Die Ergebnisse dieser theoretischen Analyse werden verwendet, um Versuchsaufbauten zu konzipieren, die dieses Prinzip zum Nachweis von GWs nutzen könnten. Diese Versuchsaufbauten basieren auf dem aktuellen Stand der Technik, sind aber nicht durch diesen begrenzt. Hauptsächlich werden kreisförmige Teilchenbeschleuniger in Form von Speicherringen betrachtet. Die wichtigsten Rauschquellen für ein Speicherring-Gravitationswellen-Observatorium (SRGO) werden untersucht, und es werden grundlegende Rauschabschätzungen auf der Grundlage der Spezifikationen bestehender Anlagen wie des Large Hadron Collider (LHC) vorgenommen. Ein großer Teil der Dissertation besteht aus numerischen Simulationen von Spielzeugmodellen eines SRGO. Das Antwortsignal des GW-Detektors wird in Abhängigkeit von verschiedenen Modellparametern erforscht. Die Fehler bei der Schätzung der Modellparameter werden mit Hilfe von Markov-Chain-Monte-Carlo-Methoden (MCMC) ermittelt, die auf künstlich erzeugte Daten mit zusätzlichem Rauschen angewendet werden. Es wird gezeigt, dass eine ideale Version eines solchen Detektors von vornherein empfindlich für Millihertz-GWs wäre und in der Lage wäre, im Alleingang genaue Einschränkungen der GW-Quellparameter zu erhalten. Es wurde versucht, so viel Physik wie derzeit möglich einzubeziehen, die die wesentlichen Aspekte der Realität abdeckt, ohne die Modelle für eine erste Untersuchung dieses neuartigen Experimentkonzepts zu sehr zu verkomplizieren. Der Schwerpunkt lag darauf, eine solide konzeptionelle Grundlage zu schaffen, robuste qualitative Schlussfolgerungen zu ziehen und Schätzungen in Größenordnungen vorzunehmen. Es wurden durchgängig Vergleiche mit der Theorie und Praxis bestehender GW-Detektoren angestellt. Wo immer möglich, werden die Ergebnisse in den Konventionen der GW-Gemeinschaft zum Zeitpunkt der Erstellung dieser Dissertation dargestellt.

Contents

Declaration on Oath

I hereby declare in lieu of oath that I have written this dissertation myself and have not used any aids or sources other than those stated.

If electronic resources based on generative artificial intelligence (AI) were used in the course of writing this dissertation, I hereby affirm that my own work was the main focus and that all resources used are fully documented in accordance with good scientific practice. I am responsible for any erroneous or distorted content, incorrect references, violations of data protection and copyright law or plagiarism that may have been generated by the AI.

Mumbai, April 21, 2024

Signature of the doctoral candidate

Acknowledgments

Embarking on this academic odyssey, I was acutely aware that the path of research is never solitary. There are many silent heroes and guiding lights that illuminate the journey.

Foremost, my deepest gratitude is directed towards my supervisors, Prof. Jochen Liske and Prof. Marcus Brüggen. Your guidance, patience, and passion for the world of science have been instrumental in shaping this dissertation.

Special mentions are warranted for Saloni Priya, Aravindh Swaminathan, Thorben Schmirander, Roman Schnabel, Mikhail Korobko, Florian Grüner, Wolfgang Hillert, and Velizar Miltchev. Engaging with each of you, debating the nuances, and collaboratively overcoming challenges have been pivotal milestones in this research expedition. Your insights and perspectives have enriched this work in ways words might scarcely capture.

I extend my sincere appreciation to the Deutsche Forschungsgemeinschaft (DFG, German Research Foundation) for their steadfast support, especially the EXC 2121 Quantum Universe – 390833306 initiative.

To my peers, colleagues, the esteemed members of the Cluster of Excellence Quantum Universe, and every individual who has contributed to this dissertation, your role has been invaluable. Whether it was a word of encouragement, a challenging question, or an insightful suggestion, each gesture has been a stepping stone to where this work stands today.

As part of good scientific practice, acknowledgments are also owed to the countless offline and online tools that aid the modern scientist in the research and documentation process, including but not limited to: Google, Overleaf, DeepL Translate, ChatGPT, ResearchGate, Wikipedia, Spyder, etc.

Lastly, to the countless unsung heroes of scientific history whose shoulders I stand upon, and to those who walk beside me in this journey, I owe a debt of gratitude. The world of science is a collective endeavor, and this work is a testament to that shared spirit.

Dedication

To my parents and grandparents,

Their dreams formed the foundation upon which I built mine. It's an honor to fulfill an aspiration that has long resided in our family's heart. Through this accomplishment, I hope to honor our lineage and inspire future generations.

Through the lens of physics, I venture forth on this path, seeking answers in the vast cosmos, carrying the legacy of a family rooted deeply in the pursuit of knowledge. In fulfilling this dream, I not only honor my own aspirations but also the unspoken dreams of those who came before me.

List of Prior Publications

The following listed publications have ensued from the pursuit of this doctoral study.

1. Rao, Suvrat, et al. “Detection of gravitational waves in circular particle accelerators." Physical Review D, vol. 102, no. 12, American Physical Society (APS), December 2020. https://doi.org/10.1103/physrevd.102.122006

2. Rao, Suvrat, et al. “Detection of gravitational waves in circular particle accelerators II. Response analysis and parameter estimation using synthetic data.” arXiv, January 2023. https://doi.org/10.48550/arxiv.2301.08331

The author of this dissertation is the first author of these publications, and was the chief contributor to their conception, realization and composition, with guidance for improvement and appreciable language editing having been done by the other co-authors. One of the co-authors, Julia Baumgarten, was also responsible for an appreciable contribution to the writing and testing of a computer code which was integral to the second publication. At the time of writing this dissertation, the second publication was undergoing review at the Physical Review D journal. These publications are included in the main content of this cumulative dissertation.

Chapter 1

Introduction

We stand at an intersection in astronomical exploration, where the merger lane of gravitational wave (GW) astronomy joins the highway road of classical astronomy, becoming the grand highway of multi-messenger observations.

By providing unprecedented access into the universe's most violent events, gravitational wave astronomy affirms key predictions of general relativity and reshapes our cosmic understanding. The detection of gravitational waves from phenomena such as binary black hole coalescences and neutron star mergers has peeled back layers of the cosmic mystery, illuminating the foundational elements of physics, astronomy, and cosmology [1, 2, 3, 4, 5].

Simultaneously, the rise of multi-messenger astronomy integrates diverse cosmic signals — gravitational waves, electromagnetic waves, neutrinos, and cosmic rays — into a coherent narrative that advances our grasp of the universe's high-energy processes and evolutionary pathways [6, 7, 8, 9].

Gravitational wave astronomy has witnessed substantial advancements since the initial direct detection by the Advanced Laser Interferometer Gravitational-Wave Observatory (LIGO) in 2015 [10]. The field gained further momentum with the observation of a binary neutron star merger in 2017 by Advanced LIGO and the European Advanced Virgo, an event also notable for its visibility across the electromagnetic spectrum [11, 12, 13].

The landmark observation of GW170817, marking the first instance of a binary neutron star merger detected through both gravitational and electromagnetic signals, has also significantly propelled multi-messenger astronomy. This event has enriched our understanding of cosmology, the physics of dense matter, and the testing of general relativity [14].

Current efforts in gravitational wave astronomy focus on the real-time detection of GWs and precise localization of their sources [15, 16]. This capability enriches multi-messenger astronomy, facilitating a more detailed examination of transient astrophysical phenomena through a combined lens of gravitational wave and electromagnetic data, promising profound implications for our understanding of the cosmos [17].

Leading these endeavors, the LIGO-Virgo-KAGRA Collaboration (LVK) continuously probes the higher frequency domains of gravitational waves, with detector

sensitivities now finer than sub-proton scales [18, 19, 20]. The insights garnered include the discovery of various mass black holes and the verification of general relativity's predictions to unprecedented precision.

With the initiation of the fourth observing run (O4) in May 2023, marked by a sensitivity increase of approximately 30%, the LVK collaboration aims to expand the observable universe's reach and increase the detection rates of gravitational wave events [21, 22]. The run leverages enhancements such as increased laser power, refined mirrors, and advanced quantum squeezing techniques, thereby boosting event detection and facilitating deeper exploration into the physics governing these cosmic phenomena.

The LVK collaboration's O4 observing run, along with wide-field electromagnetic instruments, has made multi-messenger astronomy more promising than ever. This includes new facilities like WINTER, an infrared survey telescope, and TESS, an exoplanet survey space telescope, which are well-suited for transient searches and expected to contribute significantly to the field [14].

The collaboration has recently unveiled a series of significant discoveries. A new catalog detailing 90 gravitational wave events, observed since the inception of detections in 2015 during the latter half of their third observing run (O3b), has been released. This compilation includes 35 new events, encompassing 32 black hole mergers and at least two mergers between a black hole and a neutron star. Notably, several black holes identified from these mergers have been categorized as intermediate-mass black holes, each surpassing 100 solar masses. This observation substantiates the presence of intermediate-mass black holes in the cosmos, a category previously hypothesized but not observed in such abundance [23].

The vast number of gravitational wave events detected allows for comprehensive studies of black hole and neutron star populations. By analyzing the entire population of binary black hole mergers, significant deviations from a simple power-law distribution in black hole masses were observed. This deviation provides insights into the formation processes of these black holes, be they from stellar deaths or previous mergers of smaller black holes. The spins of some merging black holes were found to be misaligned with their orbital angular momentum, which raises questions about their formation processes. The catalog has also enabled the tightest constraints so far on the properties of gravity in the strong, highly-dynamical regime of black hole mergers, further testing Einstein's theory of general relativity [24].

Some other recent advances in gravitational wave astronomy include identifying a unique signature in GW signals from supernovae, which correlates with the high-density state equations of massive progenitor stars, as derived from relativistic supernova models employing a quark-hadron equation of state [25]. Additionally, observations of extreme mass ratio inspirals (EMRIs) within active galactic nuclei (AGN) contexts, particularly concerning accretion disk interactions, are now possible, offering insights through Bayesian analysis [26]. Investigations into continuous gravitational waves now extend beyond neutron star astrophysics into realms including dark matter and exotic particle searches [27].

Looking forward, ambitious projects like the space-based Laser Interferometer Space Antenna (LISA) [28] and future ground-based observatories such as the Einstein Telescope [29] and Cosmic Explorer [30] are under development. In the mid-2030s, LISA is set to expand our observational reach, targeting gravitational-wave sources from microhertz to hundreds of millihertz. Additionally, pulsar timing arrays (PTAs) are delving into the nanohertz portion of the GW spectrum, using radio frequency pulse arrival times from an array of millisecond pulsars to detect gravitational-wave remnants. Recently, evidence has been found by NANOGrav of a stochastic background of gravitational waves in the nanohertz frequency range due to cosmological sources [31, 32].

These projects aim to significantly increase the sensitivity of gravitational wave detection and explore new aspects of the universe, like the early formation of black holes and compact object evolution, tracing their evolution from the primordial cosmos through the peak of the star formation era [33]. These investigations span an extensive range of the gravitational-wave spectrum, from attohertz to kilohertz frequencies [33].

In conclusion, gravitational wave astronomy and multi-messenger astrophysics have become increasingly critical to understanding the Universe's most energetic and cataclysmic processes. Future developments such as increased detector sensitivities and new observatories are poised to further enhance our understanding of the cosmos.

Thus, as gravitational wave physics is a hot topic and will remain so in the coming decades, innovative new GW detection principles and technologies will aid the field in expanding and progressing faster — covering a greater range of frequencies, sensitivities and parameter estimation capabilities. In this work, we propose a novel principle for detecting gravitational waves. This involves the precise timing of test masses performing uniform circular motion, to detect deviations in the measured times due to the passage of gravitational waves, compared to the expected times in the absence of gravitational waves. This timing deviation is a theoretical result derived using the general theory of relativity in the later chapters. The detection principle is illustrated in a cartoon schematic shown in Fig. (1.1).

Specifically, we explore the application of this detection principle to circular particle accelerators, in particular to storage rings, as storage rings are one of the only pre-existing and promising technologies where our detection principle may be suitably applied. We also conceptually discuss alternate experiment setups in the later chapters of this work.

In the main body of this work, we calculate the effects of astrophysical gravitational waves (GWs) on the travel times of proton bunch test masses in circular particle accelerators. We show that a high-precision proton bunch time-tagging detector could turn a circular particle accelerator facility into a GW observatory sensitive to millihertz (mHz) GWs, assuming that sources of noise have been dealt with. We comment on sources of noise and the technological feasibility of ultrafast single photon detectors by conducting a case study of the Large Hadron Collider

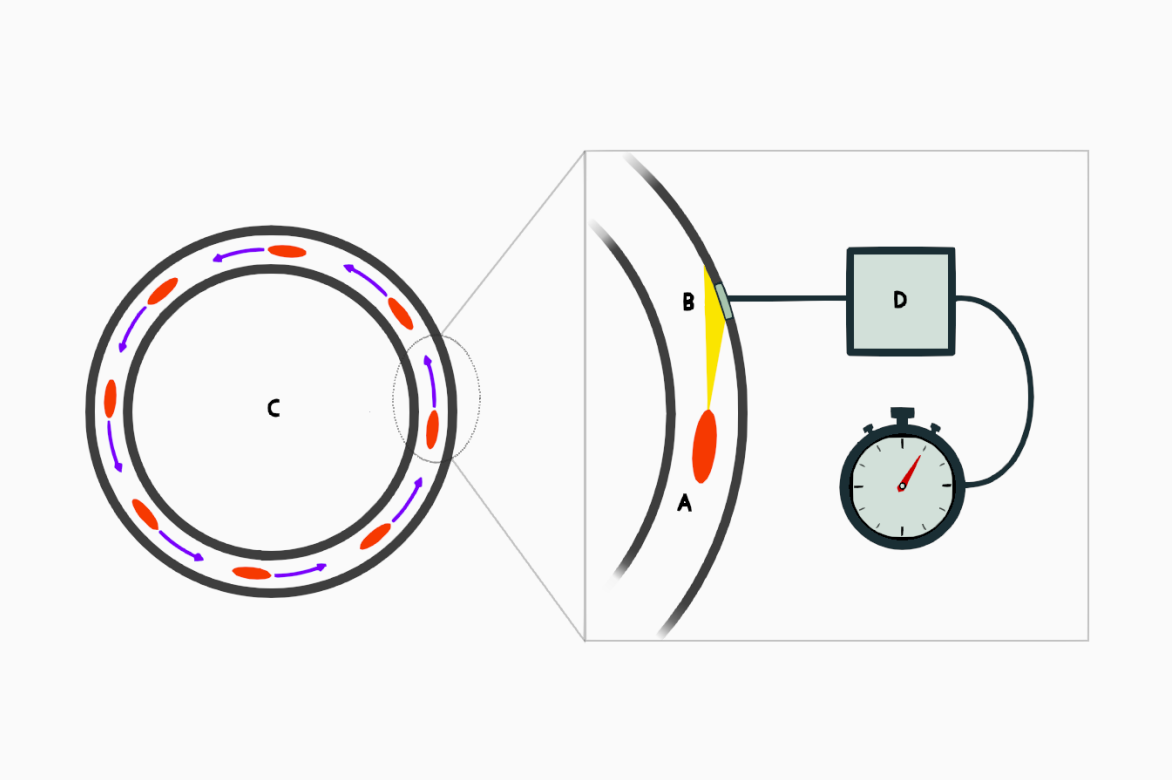

Figure 1.1: A cartoon representation of the experiment concept, where a rigid test mass (A) is performing uniform circular motion (C), and it can be timed by an atomic clock attached to a photon detector (B, D). A passing gravitational wave would cause a change in the timing data, which can be predicted by the general theory of relativity.

(LHC) at CERN.

Furthermore, we simulate the response of a Storage Ring Gravitational-Wave Observatory (SRGO) to astrophysical millihertz (mHz) gravitational waves (GWs), numerically obtaining its sensitivity curve and optimal choices for some controllable experiment parameters. We also generate synthetic noisy GW data and use Markov Chain Monte Carlo (MCMC) methods to perform parameter estimation of the source properties and their degeneracies. We show that a single SRGO could potentially localize the GW source in the sky using Earth's rotation. We also study the source sky localization area, mass and distance estimation errors as functions of noise, data sampling rate, and observing time. We also discuss, along with its implications, the capacity of an SRGO to detect and constrain the parameters of millihertz GW events.

OUTLINE: This doctoral dissertation has been organised as follows. Chap. (2) provides a concise introduction to the theoretical framework required for gravitational wave physics, including a brief historical overview of the subject. Chap. (3) acts as a handbook, listing the plethora of astrophysical sources that are expected to produce detectable gravitational waves. Chap. (4) hierarchically lists the types of gravitational wave detectors based on their detection principle, and provides comprehensive details about most of the named GW detectors spanning the past, present and future. In Chap. (5), the basic structure and functioning of storage rings

is elucidated, to prime the reader for the main body of the dissertation. Chap. (6) lays down the main theoretical underpinnings and experiment concept of this doctoral dissertation, exploring the effect of gravitational waves on the timing of test masses circulating in storage rings. Chap. (7) further expands on the previous work, with improved results based on simulations. In Chap. (8), some important sources of noise pertaining to the previous chapter are discussed. Chap. (9) is important, and conceptually explores alternate experimental setups that work on the same detection principle which is the core of this doctoral dissertation. Chap. (10) presents the robust concluding remarks distilled from the entire work. Additional information is presented in Appendices App. (A) (showing some extra results pertaining to Chap. 6); App. (B) (providing further details about the calculation of sensitivity curves of GW detectors); and App. (C) (mentioning the specifications of the computing facilities utilized for producing some of the results of this work).

Chapter 2

Overview of Gravitational Wave Theory

Gravitational waves (GWs), a fundamental prediction of Einstein's general theory of relativity, are ripples in the fabric of spacetime produced by some of the most violent and energetic processes in the universe. In some schools of thought, gravitational waves are also considered as a force experienced in the conventional sense by a test mass, albeit a non-Newtonian one i.e. a gravitational force that cannot be modeled by the classical Newtonian gravitational theory, but one that produces the same kinematics as predicted by Einstein's theory of general relativity. This section delves into the theoretical underpinnings of gravitational wave propagation, drawing from the linearized theory of Einstein's equations. Much of the material is based on [34]. Note that in the following subsections, unless explicitly mentioned, we employ the natural units system where $G = c = 1$.

2.1 A Brief History of Gravitational Waves

The theory of gravitational waves (GWs) has its roots in Albert Einstein's formulation of the general theory of relativity in 1916. Einstein's groundbreaking work, which redefined gravity as a curvature of spacetime rather than a force, implied the existence of GWs as distortions propagating at the speed of light. Initially, however, the reality of these waves was not immediately accepted, largely due to the mathematical complexity of Einstein's field equations and the conceptual challenge they posed [35].

Einstein himself, in the ensuing years, grappled with the physical interpretation of GWs, contributing to the early debates about their existence. His ambivalence reflected the broader scientific community's uncertainty. This period of skepticism and theoretical inquiry laid the groundwork for a more profound understanding of GWs, but it wasn't until the mid-20th century that significant progress was made. The advent of linearized gravity, which simplified Einstein's equations, allowed for clearer wave-like solutions and paved the way for further theoretical exploration of GWs [36].

The turning point in the journey of GWs from theoretical constructs to observable phenomena came with the discovery of the binary pulsar PSR B1913+16 by Hulse and

Taylor in 1974. Their observation of the pulsar's orbital decay over time provided the first indirect evidence of GWs, aligning precisely with the predictions of general relativity [37]. This discovery was a pivotal moment, bolstering confidence in the existence of GWs and earning the duo the Nobel Prize in Physics in 1993.

Parallel to these theoretical developments, efforts to detect GWs directly were gaining momentum, culminating in the construction of large-scale interferometric detectors. Facilities like LIGO and Virgo represented a leap in observational astrophysics, utilizing cutting-edge technology to detect the minuscule disturbances caused by passing GWs [38, 39].

The first direct detection of GWs, a landmark achievement in physics and astronomy, occurred on September 14, 2015. This detection by LIGO of GWs emanating from the merger of two black holes confirmed a key prediction of Einstein's theory and inaugurated the era of gravitational wave astronomy [40]. Subsequent detections, including the merger of neutron stars and black holes of various masses, have offered unprecedented insights into these celestial phenomena, significantly enhancing our understanding of the universe's most energetic events [11, 41].

The impact of GW detection extends across multiple scientific domains, from testing the limits of general relativity to shedding light on cosmic processes. The future of gravitational wave astronomy looks promising, with ongoing improvements to current detectors and the development of new projects like LISA. These advancements are expected to further our comprehension of astrophysical phenomena and potentially reveal new aspects of the universe [42].

2.2 Linearized Einstein Equations in Vacuum

The concept of gravitational waves emerges from considering small perturbations to the flat Minkowski spacetime. Representing the metric tensor as $g_{\alpha\beta} = \eta_{\alpha\beta} + h_{\alpha\beta}$, where $\eta_{\alpha\beta}$ denotes the Minkowski spacetime and $h_{\alpha\beta}$ symbolizes the small perturbations, allows for a linearized approach to gravitational waves. In this linearized framework, terms of order $\mathcal{O}(h_{\alpha\beta}^2)$ are neglected, and the Einstein field equations reduce to linear wave equations.

The connection coefficients, or Christoffel symbols, are defined as

$$\Gamma^{\mu}_{\alpha\beta} = \frac{1}{2} g^{\mu\nu}(\partial_\beta g_{\nu\alpha} + \partial_\alpha g_{\nu\beta} - \partial_\nu g_{\alpha\beta}) = \frac{1}{2}(\partial_\beta h^{\mu}_{\alpha} + \partial_\alpha h^{\mu}_{\beta} - \partial^\mu h_{\alpha\beta}). \tag{2.1}$$

These lead to the linearized Ricci tensor

$$R_{\mu\nu} = \partial_\alpha \Gamma^{\alpha}_{\mu\nu} - \partial_\nu \Gamma^{\alpha}_{\mu\alpha} = \frac{1}{2}(\partial_\alpha \partial_\nu h^{\alpha}_{\mu} + \partial_\alpha \partial_\mu h^{\alpha}_{\nu} - \Box h_{\mu\nu} - \partial_\mu \partial_\nu h), \tag{2.2}$$

and the linearized Ricci scalar

$$R = \eta^{\mu\nu} R_{\mu\nu} = \partial_\alpha \partial_\beta h^{\alpha\beta} - \Box h, \tag{2.3}$$

where $\Box = \partial_\alpha \partial^\alpha$ denotes the d'Alembertian operator and $h = \eta^{\alpha\beta} h_{\alpha\beta}$.

A significant aspect of linearized gravity is the freedom of gauge choice. To simplify the linearized field equations, one often employs the Lorentz gauge condition, defined by

$$\partial^\alpha \bar{h}_{\alpha\beta} = 0, \tag{2.4}$$

where $\bar{h}_{\alpha\beta} = h_{\alpha\beta} - \frac{1}{2}\eta_{\alpha\beta} h$ is the trace reversed form of $h_{\alpha\beta}$, which brings the wave equation for $\bar{h}_{\mu\nu}$ into a manifestly wave-like form. Note that under a gauge transformation, the perturbation $\bar{h}_{\alpha\beta}$ transforms as $\bar{h}_{\alpha\beta} \to \bar{h}'_{\alpha\beta} = \bar{h}_{\alpha\beta} - \partial_\beta \xi_\alpha - \partial_\alpha \xi_\beta + \eta_{\alpha\beta} \partial_\mu \xi^\mu$, where ξ^μ is a vector field characterizing the transformation. Under the Lorentz gauge condition, the vector field must satisfy $\Box \xi_\beta = \partial^\alpha \bar{h}_{\alpha\beta}$.

The Einstein field equations, $G_{\mu\nu} = R_{\mu\nu} - R g_{\mu\nu}/2 = 8\pi T_{\mu\nu}$, after applying the Lorentz gauge condition, become

$$-\frac{1}{2} \Box \bar{h}_{\mu\nu} = 8\pi T_{\mu\nu}, \tag{2.5}$$

and in vacuum (where the stress-energy tensor $T_{\mu\nu}$ vanishes) thus become

$$\Box \bar{h}_{\mu\nu} = 0. \tag{2.6}$$

2.3 Plane Wave Solutions and the TT Gauge

When the observer is far away from the GW source, which is true for all astrophysical GW sources, the general solution to the wave equation in vacuum can be represented as a plane wave. The plane wave solutions in gravitational wave theory offer significant insights into the nature of gravitational waves. We begin by considering the plane wave ansatz:

$$\bar{h}^{\alpha\beta} = \Re \left(A^{\alpha\beta} e^{i k_\alpha x^\alpha} \right),$$

where $A^{\alpha\beta}$ is the amplitude tensor, and k_μ is the wave vector satisfying the null condition $k_\mu k^\mu = 0$. The Lorentz gauge condition imposes constraints, reducing the independent components of $A^{\alpha\beta}$. Specifically, the Lorentz gauge condition requires that $\partial^\beta \bar{h}_{\alpha\beta} = 0$, which implies that $A^{\alpha\beta} k_\beta = 0$. This condition reduces the number of independent components from ten to six, as it enforces a set of four linear constraints on $A^{\alpha\beta}$.

The gravitational wave solutions are further refined by applying the transverse-traceless (TT) gauge. This gauge choice leads to a simplification of the GW solutions, where the metric perturbations are purely spatial and traceless. The TT gauge

conditions are $\bar{h}_{\alpha\beta}k^{\alpha} = 0$ and $\bar{h}^{\alpha}_{\alpha} = 0$. The first condition ensures that the wave is transverse to the direction of propagation, meaning that the physical effects of the wave occur in a plane perpendicular to the direction of wave travel. The second condition, being traceless, implies that the sum of the diagonal elements of $\bar{h}_{\alpha\beta}$ is zero. These conditions reduce the number of independent components of the gravitational wave metric further from six to two, which correspond to the two physical degrees of freedom of the gravitational wave.

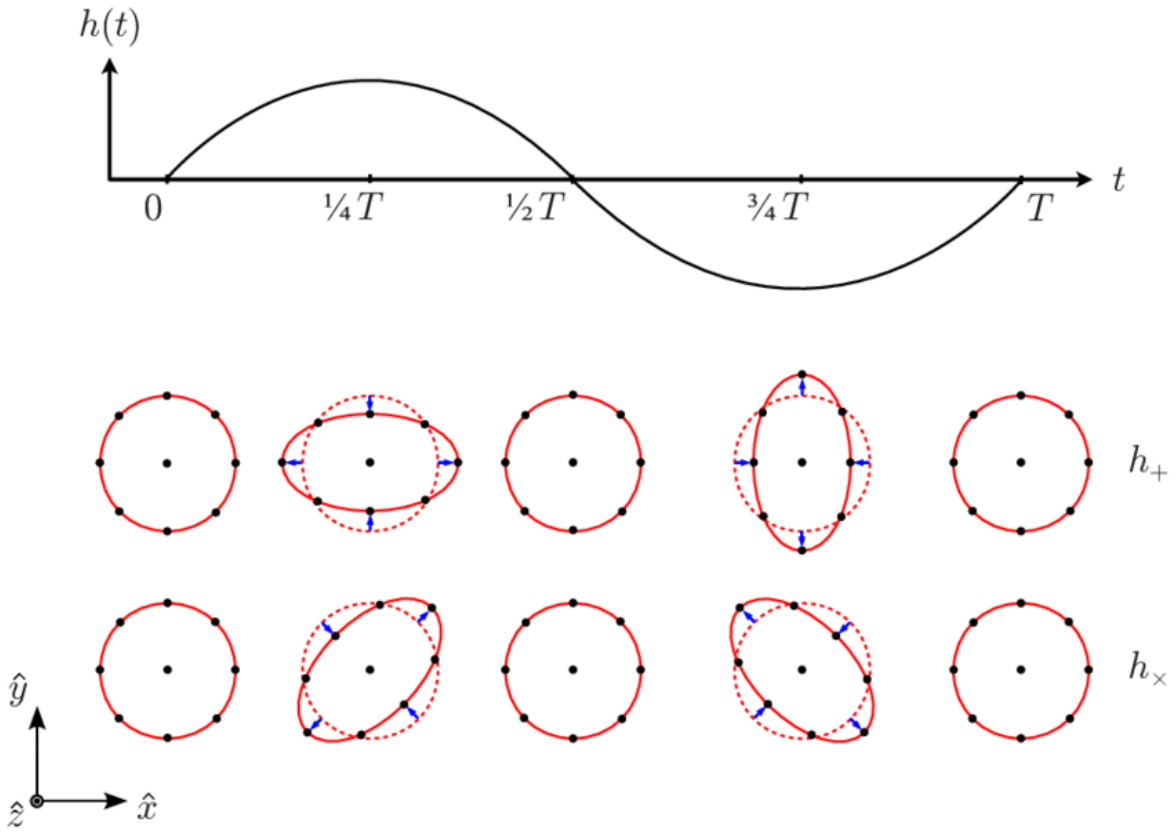

Figure 2.1: The effect of a GW propagaring perpendicular to the plane of a ring of test masses, showing the individual effects of the two GW polarizations as a function of time. This figure has been adapted from [43].

The final form of the metric in the TT gauge, showing the two polarization states, is expressed as:

$$h_{\mu\nu} = \begin{pmatrix} 0 & 0 & 0 & 0 \\ 0 & h_{+} & h_{\times} & 0 \\ 0 & h_{\times} & -h_{+} & 0 \\ 0 & 0 & 0 & 0 \end{pmatrix}. \tag{2.7}$$

These two components, h_{+} and $h_{\times}$, represent the two polarization states of the gravitational wave, often referred to as the plus and cross polarizations. This compact representation of the gravitational wave field encapsulates the essential physics of gravitational waves as predicted by general relativity, highlighting their transverse

and traceless nature.

The TT gauge provides an intuitive understanding of the physical effects of gravitational waves. In this gauge, a gravitational wave passing through a ring of test particles would cause the ring to oscillate in a characteristic "plus" and "cross" pattern, reflecting the two polarization states of the wave. This has been shown schematically in Fig. (2.1).

The Riemann curvature tensor associated with the wave demonstrates that spacetime is indeed curved in the presence of a gravitational wave, even though the linearized approximation treats the deviations from flat spacetime as small.

In summary, the propagation of gravitational waves in general relativity is elegantly captured through linearized field equations and the imposition of the TT gauge. This formalism yields a clear understanding of the wave nature of these spacetime perturbations and reveals their polarization properties, pivotal in gravitational wave detection and analysis.

2.4 The Quadrupole Formula

The general solution to the linearized Einstein field equations in the presence of matter, specifically the wave equation Eq. (2.5), is given by:

$$\bar{h}^{\mu\nu}(t, \mathbf{x}) = 4 \int \frac{T^{\mu\nu}(t - |\mathbf{x} - \mathbf{x}'|, \mathbf{x}')}{|\mathbf{x} - \mathbf{x}'|} d^3x', \tag{2.8}$$

where $T^{\mu\nu}$ is the stress-energy tensor of the matter, $\mathbf{x}$ and $\mathbf{x}'$ are spatial points, and the integration is over the volume of the matter distribution.

When considering gravitational wave generation far from the source, particularly for sources like binary systems, certain simplifications are applied. These include the assumption that the source's spatial extent is small compared to the distance to the observer and that the matter velocities within the source are significantly less than the speed of light. Under these assumptions, the integral simplifies to the Quadrupole Formula:

$$\bar{h}^{ij}(t, \mathbf{x}) = \frac{2}{d_L} \frac{d^2 I^{ij}(t - d_L)}{dt^2}, \tag{2.9}$$

where I^{ij} is the quadrupole moment of the mass distribution and d_L is the distance to the observer. The amplitude of a gravitational wave in the TT gauge is proportional to the second time derivative of the mass quadrupole moment of the source. This relates the physical motion of matter in the source to the emitted gravitational radiation.

For an equal mass circular binary system, upon calculating its quadrupole mo-

ment, we get:

$$\bar{h}^{ij} = -\frac{2Mr^2\omega^2}{d_L} \begin{pmatrix} \cos 2\omega(t-d_L) & \sin 2\omega(t-d_L) & 0 \\ \sin 2\omega(t-d_L) & -\cos 2\omega(t-d_L) & 0 \\ 0 & 0 & 0 \end{pmatrix}, \tag{2.10}$$

where M is the mass of each orbiting object, r is the orbit radius, and ω is the angular frequency.

The above equation represents the gravitational wave strain in the case of an equal mass binary system with a circular orbit, observed from a specific vantage point. To generalize this to an arbitrary observation point, we consider the binary's orientation relative to the observer. This leads to a transformation of the gravitational wave strain components to the h_+ and $h_\times$ forms, which are more convenient for observational purposes. These forms are given by:

$$h_+ = \frac{4}{d_L}\left(\frac{G\mathcal{M}}{c^2}\right)^{\frac{5}{3}}\left(\frac{\pi f}{c}\right)^{\frac{2}{3}}\frac{1+\cos^2(i)}{2}\cos(2\pi f t + \delta_0), \tag{2.11}$$

$$h_\times = \frac{4}{d_L}\left(\frac{G\mathcal{M}}{c^2}\right)^{\frac{5}{3}}\left(\frac{\pi f}{c}\right)^{\frac{2}{3}}\cos(i)\sin(2\pi f t + \delta_0). \tag{2.12}$$

If m_1 and m_2 are the masses of the objects in the binary, then $\mathcal{M} = \frac{(1+z)(m_1 m_2)^{\frac{3}{5}}}{(m_1+m_2)^{\frac{1}{5}}}$ is the redshift-corrected chirp mass. d_L is the luminosity distance of the GW source and z is its redshift. i is the inclination angle between the observer's line of sight to the GW source and the angular momentum vector of the GW source. δ_0 is the initial phase of the GW at the start of the observing time, t_0. The redshift-corrected, time-varying GW frequency is $f = (1+z)^{-1}\left(f_0^{-\frac{8}{3}} - \frac{8}{3}k(t-t_0)\right)^{-\frac{3}{8}} = (1+z)^{-1}\sqrt{G(m_1+m_2)}/\pi r^{\frac{3}{2}}$, where r is the separation between the objects in the binary; f_0 is the GW frequency at $t = t_0$, corresponding to an initial separation of $r = r_0$; and $k = \frac{96}{5}\pi^{\frac{8}{3}}\left(G\mathcal{M}/c^3\right)^{\frac{5}{3}}$. G and c are respectively, the gravitational constant and the speed of light. Here, h_+ corresponds to the "plus" polarization and $h_\times$ to the "cross" polarization. This representation encapsulates the dependence of the observed gravitational wave signal on the observer's relative position and orientation with respect to the binary system.

As the system evolves, particularly as the binary components spiral closer together, the Quadrupole Formula alone becomes insufficient. Post-Newtonian methods extend this approximation by incorporating higher-order corrections in terms of the gravitational field and velocities. This refinement is crucial for accurately describing the gravitational waveforms, especially during the late inspiral phase before the merger.

The time to coalescence, t_c, for a binary system in a circular orbit, significantly

influenced by gravitational wave emission, is expressed as:

$$t_c = \frac{5r_0^4}{256M^2\mu}, \tag{2.13}$$

where μ is the reduced mass of the binary system, and M is the mass of the components of the binary.

The frequency of the wave is determined by the dynamical timescale of the source. For systems like binary star systems, the orbital frequency directly influences the frequency of the emitted gravitational waves, which is, in fact, equal to twice the orbital frequency.

In summary, the generation of gravitational waves, as described by the linearized Einstein equations with matter, the Quadrupole Formula, and further enhanced by post-Newtonian methods, provides a comprehensive understanding of the dynamics in massive binary systems. These theoretical insights are vital for the study of gravitational waves and their role in astrophysical phenomena, particularly binary inspirals and mergers.

2.5 Summary of GW strain models

The standard quadrupole formula, while providing a fundamental framework for gravitational wave (GW) theory, finds its limitations when applied to scenarios where velocities approach the speed of light and gravitational fields intensify. In such cases, notably in the late stages of compact object mergers, an extension beyond the quadrupole approximation is necessary to accurately depict the GW phenomena. A pictoral representation of the different phases of the GW strain in compact object mergers, and the type of modeling approach used based on the source properties, is shown in Fig. 2.2.

Post-Newtonian Methods: The post-Newtonian (PN) approach serves as an advanced extension of the quadrupole formula [44, 45]. It utilizes a series expansion where the leading term aligns with the quadrupole result. This method treats the expansion in powers of v/c, where v is the velocity and c the speed of light. In PN formalism, a term of the order $1/c^{2n}$ is considered as the n-th post-Newtonian order. The PN approach is particularly efficient in depicting the inspiral phase of compact binaries, offering the convenience of rapid computational analysis through analytic formulas. However, as the system nears merger, the PN approximation's accuracy diminishes under the strain of increased nonlinearities and relativistic velocities.

Numerical Relativity: Numerical relativity comes into play when the gravitational fields are highly nonlinear and the velocities approach relativistic scales. In this approach, the full Einstein equations are numerically solved, often employing a spacetime foliation into 3D hypersurfaces [46]. Numerical relativity is indispensable for studying the late stages of inspiral and the merger phase, providing accurate

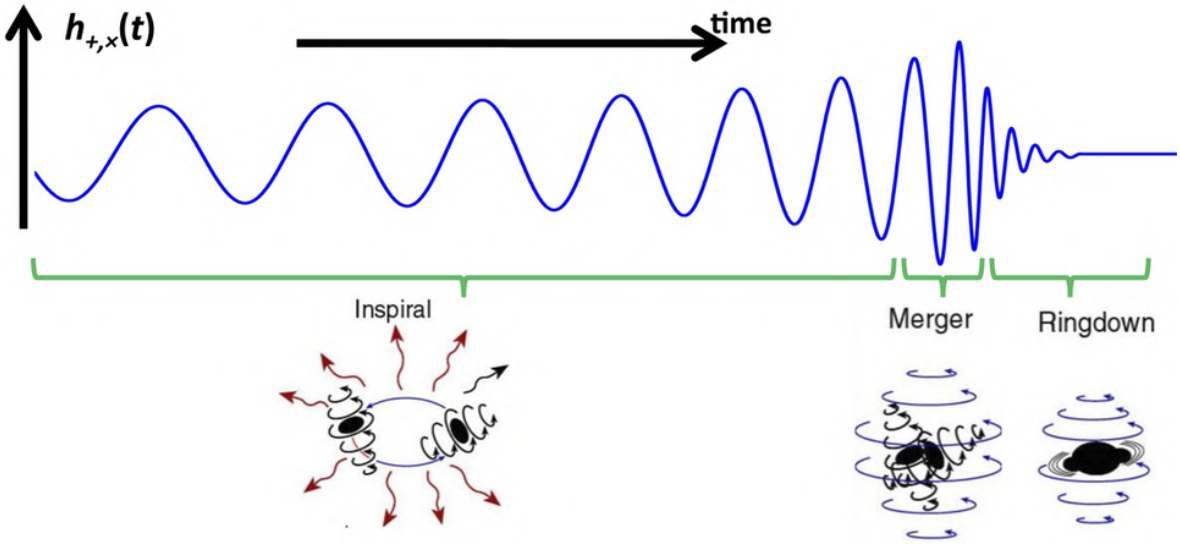

(a)

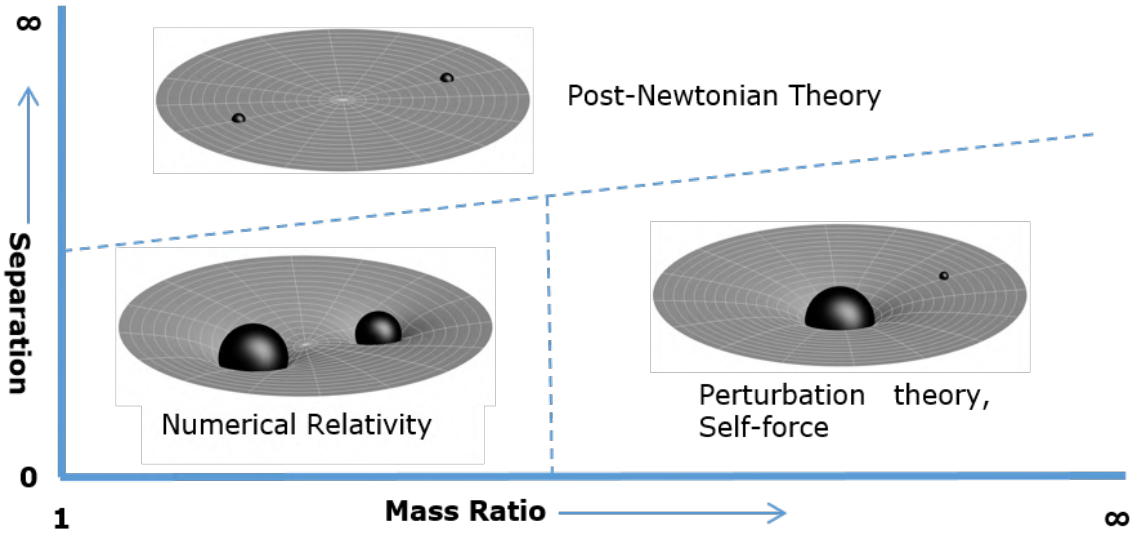

(b)

Figure 2.2: The top panel shows the typical evolution of the GW strain due to a compact binary inspiral. It can be divided into the inspiral phase, the merger phase, and the ringdown phase. The bottom panel shows the approach to modeling the strain depending on the mass and separation of the binary components.

results albeit at a significant computational cost. Consequently, the inspiral phase is often analyzed using PN methods, followed by numerical relativity to simulate the final stages and the merger [47].

Quasinormal Modes: Post-merger, particularly in scenarios leading to a black hole, the system emits GWs characterized by quasinormal modes. These are perturbations on a Kerr black hole background, assuming regularity conditions at the event horizon and infinity [48]. The GW frequency and decay rate in this phase depend solely on the mass and angular momentum of the resultant black hole, representing the system's transition from a distorted state to the stationary Kerr solution [49].

Hybrid Approaches: The generation of waveform templates for GW detection, especially for binary mergers, requires incorporating results from numerical relativity into more computationally manageable frameworks. Methods like the effective one-body approach [50] and phenomenological waveform models have been developed for this purpose [51]. These methods utilize limited results from numerical simulations to parameterize formulas in PN theory or algebraic models, enabling the rapid generation of waveform templates [52].

Extreme Mass Ratio Inspirals (EMRIs): EMRIs involve a compact binary system where one companion is significantly less massive than the other [53]. These systems are expected to be observed by future missions like LISA, offering insights into the dynamics of such unique binaries [54]. Modeling the GW strains of EMRIs usually consists of approximating the small compact object as a test mass following a geodesic of the spacetime caused by the much larger black hole.

The Newman-Penrose Scalars and Spin-Weighted Spherical Harmonics: In gravitational wave analysis, ψ_4, a complex Newman-Penrose scalar related to the Weyl tensor and null tetrad, is often employed. It is associated with the GW polarizations h_+ and $h_\times$ [55]. The spin-weighted spherical harmonics, ${}_sY^{\ell,m}$, facilitate the representation of vector and tensor fields on the unit sphere, crucial for describing quadrupolar GWs [56].

In essence, these advanced methodologies and theoretical developments in gravitational wave physics enable a more comprehensive and precise understanding of GW phenomena, particularly in regimes where traditional quadrupole formulas are inadequate.

Chapter 3

Overview of Gravitational Wave Sources

This section elucidates the diverse array of astrophysical and cosmological sources that generate gravitational waves, delineating them into two broad categories: Resolvable and Stochastic sources, based on whether individual sources can be detected. The Resolvable sources are further classified into Transient sources, where the GW signal (which may or may not be periodic), has a secular evolution over time and comes to an end eventually, as opposed to Continuous sources, where the GW signal is periodic, has no secular evolution, and lasts for an indefinite duration.

3.1 Resolvable Sources

In the realm of detectable, individual events, gravitational waves offer a unique lens to observe astrophysical phenomena. Among these, transient events stand out for their dramatic and cataclysmic nature.

3.1.1 Transient Sources

- **Supernova Explosions:** Supernovae are cataclysmic astronomical events signifying the explosive end of a star's lifecycle. They are broadly classified into core-collapse supernovae (Types II, Ib, and Ic), marking the explosive demise of massive stars, and thermonuclear supernovae, typically involving white dwarfs. Core-collapse supernovae are the final act of massive stars, occurring when the core's nuclear fuel is exhausted, leading to a gravitational collapse and a subsequent explosion. These spectacular events are observed through various electromagnetic wavelengths, from radio to gamma rays, and are detectable across vast cosmic distances. They are relatively rare occurrences, with about one supernova explosion estimated per galaxy per century. The gravitational waves from supernovae predominantly arise from protoneutron star oscillations, with the frequency range generally lying in the audio band, making them potential targets for current and future gravitational wave detectors. The gravitational wave strain from these events, however, is expected to be relatively weak, potentially marginally visible with current detectors for a source within our galaxy. The rapidly rotating models that develop non-axisymmetric instabilities may be visible up to a megaparsec distance with third-generation

detectors [57].

- **Compact Binary Coalescences:** These sources consist of two orbiting compact astrophysical objects, such as white dwarfs, neutron stars or black holes. Their GW signals usually consist of an inspiral, merger and ringdown phase, which is periodic in nature but also shows a secular evolution over time. Depending on several parameters, the detectable GW signal may last for seconds, up to several weeks or more.

  - *Binary Neutron Stars (BNS):* Binary neutron stars (BNS), pivotal in the realm of astrophysics, represent tightly bound binary systems composed of two neutron stars. Their formation is a consequence of the evolutionary trajectory of binary star systems, where both stars, massive enough, ultimately collapse into neutron stars. As gravitational wave sources, BNS are particularly noteworthy for their role in multi-messenger astronomy. The landmark detection of GW170817 by the LIGO-Virgo collaboration, followed by observations across the electromagnetic spectrum, marked the first instance of multi-messenger astronomy involving gravitational waves. This event not only corroborated the association of BNS mergers with short gamma-ray bursts but also provided compelling evidence of kilonovae phenomena and r-process nucleosynthesis, whereby heavy elements are synthesized. The rarity and distribution of BNS in the universe are subjects of ongoing research, with current observations suggesting a diverse population of such systems. Observationally, BNS are primarily detected via gravitational waves and, subsequently, through their electromagnetic counterparts, offering a rich tapestry of data across various wavelengths. These observations have been instrumental in testing general relativity in strong gravity regimes and have opened new avenues in fundamental physics and astrophysics. BNS within the galaxy may be observed at millihertz frequencies during their early inspiral phase by future space-based interferometric GW detectors such as LISA, as individually resolvable sources or as part of a stochastic background. At higher redshifts and kilohertz frequencies, their late inspiral, merger and ringdown phases are frequently observed by the current and future generations of terrestrial interferometric detectors such as the Ligo-Virgo collaboration [1, 6, 7, 8, 11, 12, 13, 58].
  - *Binary Black Holes (BBH):* This group consists of GWs emitted from the inspiral, merger and ringdown of a binary system consisting of two black holes, which eventually coalesce into a single black hole. Probing such systems offer insights into fundamental physics, black hole physics, and gravitational physics [59]. However, it is rare for such systems to have multi-messenger signals, although there are proposed mechanisms and candidate events which retain such possibilities [60, 61]. Based on the masses of the black holes, they can be further classified as:
    - Stellar-Mass Binary Black Holes: These are formed from the collapse of extremely massive stars and weigh between 5 to 10 times the mass of

the sun. Their mergers are commonly observed by terrestrial interferometric detectors such as LIGO, and several dozens of such detections have been made as of present [23]. Stellar-mass BBHs as detected by LIGO fall in the high-frequency GW range, i.e. around the kilohertz range.

* Intermediate-Mass Binary Black Holes: Mergers that fill the gap between stellar-mass and supermassive black holes, being a class of black hole with mass in the range $10^2 - 10^5$ solar masses. The postulated formation channels for such systems include the merging of stellar mass black holes and other compact objects via accretion; runaway collisions of massive stars in dense stellar clusters leading to a collapse of the collision product into an intermediate mass black hole (IMBH); the possibility of being primordial black holes formed during the Big Bang. These may be present in globular clusters and near the central region of galaxies. Binaries consisting of two IMBHs would be rare, and they would mostly be detected in extreme mass ratio inspirals (EMRIs). An IMBH within a globular cluster would be the more massive component of an EMRI if it captures stellar mass compact objects, otherwise it would be the lighter component if IMBHs at the centers of galaxies are captured by the central supermassive black hole (SMBH). Most scenarios involving IMBH mergers would produce GWs in the millihertz frequency range, but the lightest ones are usually observed by the Ligo-Virgo-Kagra collaboration in the higher frequency range [4, 62, 63, 64, 65].
* Supermassive Binary Black Holes: These are black holes with masses above 10^5 solar masses, usually present at the centers of galaxies. Their binary mergers, therefore, are generally associated with the merging of two galaxies. These may be observed as far as redshifts of $z = 10$ [66], when the first galaxies started merging, and pertain to the strongest resolvable GW strains that could possibly be detected. SMBH binaries that can be resolved, would emit primarily in the millihertz frequency range, and are therefore expected to be detected by space-based interferometric GW detectors such as LISA [4]. But as part of a stochastic background, they would fall in the nanohertz frequency range, and have been possibly detected by pulsar timing experiments [67].

– *Neutron Star-Black Hole Binaries (NSBH):* Such systems may also be extreme mass ratio inspirals, but they are classified separately if the black hole is of stellar mass, i.e. not much larger than the mass of the neutron star [68]. These sources may also produce electromagnetic counterparts, however, since one of the objects is a black hole, this is less likely as compared to BNS mergers, and no such observation has been made as of yet [69]. NSBH mergers are observed by LIGO at kilohertz frequencies [23].

– *White Dwarf Binaries:* Binary systems comprising at least one white dwarf have garnered considerable attention as sources of gravitational waves.

Formed from the remnants of binary stars, where one or both components evolve into white dwarfs post nuclear fuel exhaustion, these systems provide a window into the intricate mechanics of stellar evolution. Their detection predominantly relies on electromagnetic methods due to their faint luminosity and considerable cosmic distances. The frequency and spatial distribution of these binaries in the universe, while not exceedingly rare, present challenges in detection. The advent of multi-messenger astronomy, which synergizes electromagnetic, neutrino, and gravitational wave observations, significantly enhances our understanding of these celestial phenomena. Galactic white dwarf binaries, particularly those in tight orbits, are reliable sources of gravitational waves in the mHz frequency band for space-based detectors like LISA. A few thousand to a few tens of thousands of these systems will be individually resolvable by LISA, depending on the final detector configuration. Observations of these binaries through decihertz detectors would illuminate the evolutionary path of Type Ia supernovae, one of the most energetic events in the universe. The gravitational wave signals in the decihertz regime could play a crucial role in probing the nature and properties of the progenitors of Type Ia supernovae. Furthermore, coincident detections of merging white dwarfs may be utilized to calibrate SN Ia luminosities, thus offering a new avenue for understanding the dynamics of the universe and the behavior of these compact objects [70, 71, 72, 73, 58].

  - *Extreme Mass Ratio Inspirals (EMRIs):* These sources consist of a black hole, usually an IMBH or SMBH, into which a much smaller compact object, such as a stellar mass black hole, neutron star or white dwarf, inspirals. The lighter mass usually follows the geodesic of the spacetime caused by the much larger black hole. Since one of the objects may not be a black hole, there are proposed mechanisms which increase the probability of an electromagnetic counterpart associated with the GW signal [74]. EMRIs are expected to be detected by space based interferometers in the millihertz frequency range [58, 75].

- **Exotic compact objects:** This pursuit also opens the door to potentially discovering and understanding exotic compact objects, like quark stars, which could exhibit distinct gravitational wave signatures. For instance, GWs may be emitted during the phase transition of a neutron star to a quark star [76]. Apart from these, magnetars, a type of neutron star with extremely strong magnetic fields, often exceeding 10^{14} Gauss, are also intriguing targets for GW astronomy. The decay of these magnetic fields powers irregular bursts in X-rays and gamma-rays. The catastrophic rearrangements of the magnetic field in magnetars can lead to the emission of gravitational waves [77].

3.1.2 Continuous Sources

- **Rotating Compact Objects:** Rotating neutron stars and pulsars, as continuous gravitational wave sources, offer a unique avenue for astrophysical exploration.

These objects, which are dense, compact remnants formed from the evolutionary end points of main-sequence stars, can rotate at speeds of several hundred times per second. Unlike the transient gravitational waves produced by binary coalescences, continuous waves from these sources are likely to exhibit a well-defined, steady frequency, yet they are expected to be weaker in amplitude. Despite this, current gravitational wave detectors such as LIGO are capable of detecting these signals, especially following their recent sensitivity enhancements. The gravitational wave emission from these neutron stars primarily arises from rotational asymmetries. These asymmetries could be due to surface irregularities, often referred to as 'mountains', or from distortions caused by the neutron star being part of an accreting binary system, or due to precession resulting from misalignments in the star's rotation axis. However, a perfectly symmetric neutron star would not produce such gravitational waves; an enduring, non-axisymmetric distortion is necessary. Although continuous gravitational waves from these sources have not been directly detected yet, their discovery would mark a significant milestone in gravitational wave astronomy and offer invaluable insights into the interiors and evolution of these astrophysical objects [78]. Continuous GW sources are broadly of the following types:

- *Isolated Neutron Stars:* Isolated neutron stars can emit gravitational waves due to their own asymmetries and oscillation modes. Particularly r-modes in neutron stars, which are toroidal modes of oscillation where the restoring force is the Coriolis force, can be significant sources of gravitational waves. These modes are generically unstable to the Chandrasekhar–Friedman–Schutz (CFS) instability in rapidly rotating stars, making them potential GW sources [79, 80].

- *Pulsars:* These are rapidly rotating neutron stars emitting beams of radio waves. Their impeccable timekeeping abilities make them potential sources for GW detection. The distortions in space caused by passing gravitational waves can impact the arrival times of a pulsar's pulses, offering a multi-messenger approach to understanding these phenomena. In other words, the same isolated pulsar could be a source of continuous, high-frequency GWs, while also being detected electromagnetically as a radio pulsar. Note that a pulsar-timing experiment operates at very low frequencies (nanohertz), so timing the pulsar cannot practically be used to detect its own potential continuous-GW emission, which would be around the LIGO frequency range [81].

- *Neutron Stars in Binaries:* In binary systems, neutron stars can accrete matter from a companion star, leading to continuous gravitational wave emissions. The accretion dynamics can be affected by the neutron star's magnetic field, leading to larger gravitational waves detectable by detectors like aLIGO [82, 83].

3.2 Stochastic Sources

Beyond the resolvable sources lie the stochastic backgrounds, akin to the cosmic hum of gravitational waves. These backgrounds are formed by a superposition of innumerable, often indistinguishable, sources. The stochastic gravitational wave background (SGWB) [84, 85, 86] is a fascinating subject, encompassing a variety of astrophysical and cosmological phenomena. These phenomena can produce stochastic GWs over the entire frequency range, including and even well beyond the domain of existing and planned GW detectors. However, for such frequency ranges, indirect methods of detecting the SGWB have also been conceived [87].

3.2.1 Cosmological Background

- **Inflationary Processes:** During the inflationary epoch, quantum fluctuations in the early universe are amplified, leading to the generation of gravitational waves. These waves from inflation are vacuum fluctuations of the graviton, magnified during the universe's exponential expansion. The stochastic background from these processes can have unique signatures, potentially detectable across a wide frequency range by future experiments. This could provide valuable insights into the dynamics of inflation [88].

- **Cosmic Phase Transitions:** Cosmological phase transitions in the early universe can produce anisotropic SGWBs, similar to the cosmic microwave background (CMB). These transitions, especially first-order ones, can lead to significant gravitational wave production. The gravitational waves from these events, such as from supercooled phase transitions, electroweak phase transition and the QCD phase transition, are influenced by factors like thermal corrections and Barrow entropy. These contributions add complexity and richness to the SGWB landscape [89].

- **Cosmic Preheating/Reheating Periods:** The SGWB signals emanating from the preheating and reheating phases following the inflationary epoch are pivotal in understanding the early universe's dynamics. The preheating stage is characterized by strong non-perturbative field excitation, leading to exponentially growing particle densities, which in turn generate gravitational waves. The subsequent reheating phase, marking the universe's transition to a hot, radiation-dominated state, further contributes to the SGWB. The gravitational waves produced during this period offer insights into the mechanisms that drove inflation and the early universe's evolution, with their spectrum bearing distinct characteristics similar to those from a first-order phase transition. These insights, gleaned from the SGWB, are crucial for a deeper understanding of the fundamental processes during the universe's infancy [90, 91].

- **Topological Defects:** Theoretical entities such as cosmic strings, monopoles, or domain walls, which are predicted in some extensions of the standard model of particle physics, can generate gravitational waves. Cosmic strings, predicted

in many grand unified theories (GUTs) combined with cosmic inflation, may contribute significantly to the SGWB. These strings can generate strong gravitational wave (GW) signals across a broad frequency range, detectable by experiments like LIGO and LISA. The stochastic background they produce is potentially accessible to current and planned gravitational wave detectors, as well as being constrained by big bang nucleosynthesis (BBN), the cosmic microwave background (CMB), and pulsar timing [92, 93, 94].

- **Dark Matter:** The contributions of dark matter to the Stochastic Gravitational Wave Background (SGWB) are an intriguing aspect of cosmological research. Dark matter, particularly when interacting with supermassive black hole binaries within dense structures like dark matter spikes, is theorized produce detectable gravitational wave signals in the nanohertz frequency range. These interactions provide a unique window into the gravitational influence of dark matter in cosmic structures. Moreover, the role of ultralight bosons, potential dark matter candidates, is significant in this context. They are hypothesized to cause superradiant instabilities around spinning black holes, forming "bosonic clouds" that dissipate energy through gravitational waves. This phenomenon suggests a distinct gravitational wave signature that could unveil the elusive properties of dark matter. The exploration of these signals with future space-based gravitational wave detectors and pulsar timing arrays is expected to enhance our understanding of dark matter and its role in the cosmos [95, 96, 97]. However, this is an area of active theoretical exploration with many uncertainties. Direct detection and attribution to dark matter remain challenging.

3.2.2 Astrophysical Background

The astrophysical background of stochastic gravitational waves, distinct from its cosmological counterpart, arises from the superposition of a myriad of astrophysical processes and events throughout the universe's history. This background is dominated by the cumulative effect of several classic astrophysical GW sources. It is a gravitational wave symphony composed of distant, unresolved sources such as binary mergers, supernovae, and white dwarf binaries, creating a continuous, stochastic gravitational wave background. Future space-based GW detectors such as LISA would be able to detect an astrophysical GW background due to unresolvable sources within our galaxy [58]. An interesting potential contribution could come from Primordial Black Holes.

- **Primordial Black Holes (PBHs):** The gravitational waves (GWs) from PBHs encompass a broad spectrum, contributing to both resolvable and stochastic backgrounds. For instance, the incoherent sum of unresolved GW signals from PBH mergers across the universe's history could result in a stochastic GW background (SGWB), particularly relevant in the nanohertz frequency range. This was suggested by data from pulsar timing arrays, which may have detected a SGWB at nanohertz frequencies, potentially indicative of primordial density

perturbations that could be the origin of stellar-mass PBH formation. PBHs, spanning a wide range of masses, consequently cover various GW frequency ranges. Upcoming missions like LISA (Laser Interferometer Space Antenna) are expected to be sensitive to GWs from PBHs, especially in the millihertz frequency band, offering a complementary perspective to ground-based GW detectors. The SGWB from PBHs formed in the radiation-dominant era of the universe can be used to discover or constrain their existence. Furthermore, PBHs are speculated to have left clear signatures in the coalescence of supermassive black hole seeds in the late universe, detectable by observatories like LISA. This range includes PBHs of asteroid-mass, with LISA poised to probe GW backgrounds from various sources like ultralight, evaporated PBHs, early and late PBH binaries, and hyperbolic encounters. Gravitational waves from individual sources, such as intermediate-mass PBH mergers at high redshifts, inspirals with extreme mass ratios, and even quasi-monochromatic continuous waves from subsolar-mass PBHs, are expected to be within LISA's detection range [98, 59].

In summary, the universe's gravitational wave arena is vast and varied, encompassing a multitude of sources ranging from the cataclysmic and transient to the persistent and stochastic. The study of these sources not only furthers our understanding of gravitational waves but also unravels the mysteries of the cosmos.

Chapter 4

Overview of Gravitational Wave Detectors

This chapter presents a detailed overview of the existing and future gravitational wave detectors, including their detection principles, operational statuses, technological advancements, and significant achievements in the field of astrophysics. Fig. (4.1) shows a comprehensive overview of the sensitivity curves of many of the prominent existing and future GW detectors covered in this section.

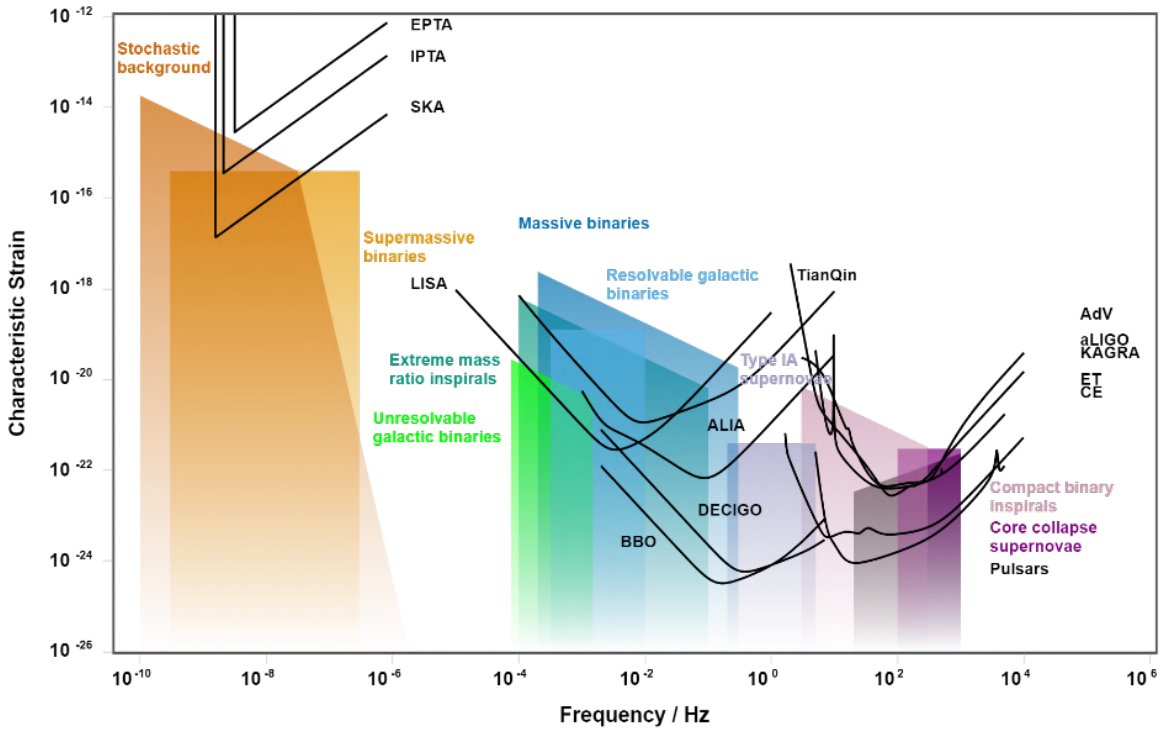

Figure 4.1: A comprehensive overview, in a characteristic strain versus frequency plot, of the expected gravitational wave sources overlaid with the sensitivity curves of several existing and proposed future gravitational wave detectors. This figure has been generated using gwplotter.com [99].

4.1 Existing Gravitational Wave Detectors

4.1.1 Resonant Mass Detectors

Resonant Mass Detectors (RMDs) utilize large, solid masses shaped into cylinders or spheres, typically made of metals like aluminum or niobium, that are cooled to cryogenic temperatures to reduce thermal noise. These masses are expected to resonate in response to gravitational waves. Extremely sensitive transducers attached to the masses detect minute vibrations and translate them into electrical signals.

- EXPLORER (Cryogenic Explorer, CERN, Switzerland, operational since 1985): A pioneering detector in the field, using a cryogenically cooled cylindrical bar to detect kilohertz frequency gravitational waves. No detections have been reported, but it has been valuable for setting upper limits on gravitational wave strength [100].

- GEOGRAV (Genius Observer of Gravitational Waves, Italy, operational since the 1980s): Specializes in resonant mass detection using a horizontal cryogenic bar, contributing to early gravitational wave research. It targets GWs in the kilohertz range, but no detections have been reported to date [101].

- ALTAIR (Advanced Large-scale Transducer for Antimatter Inspection and Research, Italy, operational since 1990): Features innovative resonant mass detection technology, targeting kilohertz frequency gravitational waves. No detections have been reported as of yet [102].

- ALLEGRO (Acoustical Levitation Ground Gravitational-wave Observatory, USA, 1991-2008): Utilized a unique resonant mass design with an aluminum cylinder, targeting kilohertz GWs. Though now defunct, it provided valuable data and insights into detector design [103].

- NIOBE (Nuclear Interference Observation with a Bar Experiment, Australia, operational since 1993): Employs a large Niobium bar detector, cooled to enhance sensitivity to gravitational waves in the kilohertz range. No confirmed detections have been made [104].

- NAUTILUS (Nuclear Tautological Utilitarian Interferometer, Italy, operational since 1995): Utilizes a cryogenic resonant bar, contributing significant data towards the understanding of gravitational waves in the kilohertz frequency range. No direct detections have been made yet [105].

- AURIGA (Antenna Ultracryogenic Resonating in Genoa, Italy, operational since 1997): A key player in the resonant mass detector arena, using a large aluminum bar at cryogenic temperatures for enhanced sensitivity to kilohertz GWs. No direct detections have been reported yet [106].

- Mario Schenberg (Brazil, operational since 2003): A spherical resonant mass detector, unique in its design, aiming to enhance sensitivity and omnidirectional detection capabilities in the kilohertz range. No detections have been reported to date [107].

- MiniGrail (Miniature Gravitational Radiation Antenna in Leiden, Netherlands, operational since 2003): Another spherical resonant mass detector focusing on kilohertz gravitational waves. It serves as a testbed for advanced detector technologies. No detections have been reported yet [108].

4.1.2 Interferometers

These detectors use laser interferometry, where laser beams are split along two perpendicular paths. Variations in the path lengths, caused by gravitational waves, are detected through oscillations of the interference patterns in the recombined beams.

- TAMA 300 (Tokyo Advanced Medium-scale Antenna, Japan, operational since 1995): An early endeavor in laser interferometry, providing valuable data and operational experience for future interferometric detectors. It was designed to probe the kilohertz frequency range. No direct detections have been made, but it has been instrumental in refining detection methods [109].

- GEO600 (Germany, operational since 1995): Known for its unique design and use of advanced technologies like squeezed light to improve sensitivity. An important contributor to collaborative gravitational wave research. It operates in the kilohertz frequency range. No direct detections have been made, but it plays a crucial role in technology development [110, 111].

- LIGO (Laser Interferometer Gravitational-Wave Observatory, USA, operational since 2002): A landmark project in gravitational wave astronomy, consisting of two detectors in Hanford and Livingston respectively. It targets GWs in the low to several kilohertz frequency range. LIGO's advanced detectors made the first-ever direct observation of gravitational waves in 2015, a breakthrough in the field [18].

- CLIO (Cryogenic Laser Interferometer Observatory, Japan, operational since 2006): A prototype for future cryogenic interferometers, CLIO tested technologies critical for reducing noise at low temperatures. It has been designed for the kilohertz GW frequency range. No detections have yet been reported, but it has been vital for technology advancement [112].

- Virgo (Virgo Interferometer, Italy, operational since 2007): With its 3-kilometer arms, Virgo complements the LIGO detectors, enhancing the global network's sensitivity and sky coverage. It has jointly observed several gravitational wave events with LIGO, and is sensitive to GWs at low to kilohertz frequencies [19].

- KAGRA (Kamioka Gravitational Wave Detector, Japan, operational since 2019): Notable for its underground location and use of cryogenic technology, KAGRA adds to the global network of detectors, improving the localization and understanding of gravitational wave sources. No independent detections have been reported yet, but it aims to detect GWs in the low several kilohertz frequency range [20].

4.1.3 Pulsar Timing Arrays (PTAs)

PTAs use the regularity of radio pulses from pulsars. Gravitational waves cause variations in the arrival times of these pulses, detectable by studying timing residuals from several pulsars.

- IPTA (International Pulsar Timing Array, established in 2004): Combines data from several pulsar timing projects, targeting nanohertz gravitational waves. Status: Operational. No direct detections have been made yet [67].

- EPTA (European Pulsar Timing Array, established in 2004): Uses European radio telescopes for nanohertz gravitational wave detection. Recently, marginal evidence for a gravitational wave background has been found [113].

- NANOGrav (North American Nanohertz Observatory for Gravitational Waves, founded in 2007): Monitors pulsars for nanohertz gravitational waves, with recent evidence suggesting a possible detection of a gravitational wave background [31, 32].

- PPTA (Parkes Pulsar Timing Array, Australia, operational since 2004): Observes pulsars using the Parkes radio telescope, focusing on nanohertz gravitational waves. Recent reports suggest evidence for a gravitational wave background [114].

- InPTA (Indian Pulsar Timing Array, operational since 2015): Enhances low-frequency gravitational wave detection capabilities, focusing on nanohertz range. Status: Operational. No detections have been reported yet [115].

4.2 Future Gravitational Wave Detectors

4.2.1 Space-Based Interferometers

Designed to observe low-frequency gravitational waves in space, these detectors offer longer baselines and freedom from terrestrial constraints, enabling detection of waves from massive astronomical events.

- LISA (Laser Interferometer Space Antenna, International Collaboration, launch expected in 2034): A space-based mission with a constellation of spacecraft, aiming to detect gravitational waves in the millihertz range [28].
- DECIGO (Deci-hertz Interferometer Gravitational wave Observatory, Japan, planned for 2027): A proposed space mission to detect gravitational waves in the decihertz range, bridging the gap between LISA and ground-based detectors [116].
- TianQin (China, 2030s): A planned space-based laser interferometric gravitational wave detector project, aiming to detect millihertz frequency gravitational waves [117].
- Taiji (China, 2030s): This is a laser interferometric detector proposed to complement LISA, focusing on millihertz frequency gravitational wave detection from space [118].
- BBO (Big Bang Observer, International Collaboration, proposed): A proposed far future successor to LISA, it aims to extend the frequency range of space-based gravitational wave observations, targeting decihertz to millihertz frequencies. BBO will be focused on ultra-precise measurements of cosmological parameters, designed primarily to search for inflation-generated stochastic gravitational waves in the band 0.03 Hz to 3 Hz [119].
- ALIA (Advanced Laser Interferometer Antenna, International Collaboration, proposed): Proposed to target gravitational waves from intermediate-mass black hole mergers and intermediate-mass ratio inspirals between few mHz and 0.01 Hz [120].

4.2.2 Ground-Based Interferometers

These advanced detectors aim to detect gravitational waves from a wide range of sources, with enhanced sensitivity compared to current ground-based detectors.

- Einstein Telescope (European Collaboration, 2030s): An ambitious project proposing a triangular-shaped underground detector, aiming for unprecedented sensitivity across a broad frequency range including LIGO's range and beyond. Status: Proposed [29].
- Cosmic Explorer (USA, 2030s): Planned as a next-generation ground-based detector with long arm lengths, aiming to observe a wide range of gravitational wave sources including LIGO's range and beyond. Status: Proposed [30].
- LIGO-India (India, 2030s): A collaborative project extending LIGO's capabilities to India, aiming to enhance the global network of gravitational wave interferometers. Status: Under construction [121].

4.2.3 Atom Interferometers

Similar to laser interferometers, these proposed detectors aim to use the wave property of matter to detect GWs using atomic interferometry.

- AION (Atom Interferometer Observatory and Network, United Kingdom): AION is an innovative gravitational wave detector that employs cold strontium atoms in an atom interferometer to detect gravitational waves. Its primary focus is on the mid-frequency range, bridging the gap between the peak sensitivities of detectors like LISA and LIGO. AION aims to explore gravitational waves from intermediate-mass black hole mergers and early-universe cosmology [122].
- MIGA (Matter-wave laser Interferometric Gravitation Antenna, France): Combines atom interferometry with laser interferometry. It aims at probing gravitational waves in the frequency band of approximately $0.1 - 10$ Hz, a range not thoroughly covered by future long baseline optical interferometers. This project is still in the development phase [123].
- ELGAR (European Laboratory for Gravitation and Atom-interferometric Research): ELGAR is a proposed European underground facility designed for gravitational wave detection in the infrasound band (0.1–10 Hz). It plans to utilize advanced atom-interferometric techniques to fill the sensitivity gap between future space-based instruments like LISA and third-generation ground-based detectors. This facility will be a culmination of progress in atomic physics and large-scale atom interferometry, fostering new collaborations across European research centers specializing in quantum sensors [124].
- MAGIS-100 (Matter-wave Atomic Gradiometer Interferometric Sensor-100, USA): Utilizing atomic gradiometer interferometric techniques, MAGIS-100 is poised to contribute to the evolving landscape of gravitational wave astronomy and related research in fundamental physics. It aims to detect gravitational waves in the unexplored frequency range of 0.01 Hz and 3 Hz, between the sensitivity ranges of LISA and LIGO/Virgo [125].

4.2.4 Novel Detection Methods

These rely on novel GW detection principles and associated technologies, to open new avenues in gravitational wave astronomy.

- LSD (Levitated Sensor Detector, International Collaboration): Investigates the use of optically trapped and cooled microspheres to detect gravitational waves through the motion of these spheres. This innovative method aims to detect gravitational waves in the high-frequency range, higher than that of traditional laser interferometer detectors like LIGO. Potential GW sources targeted are

coalescences of primordial black holes or annihilation of dark matter particles. Status: Under construction [126].

- TOBA (Torsion Bar Antenna, Japan): A novel approach using suspended bars to detect gravitational waves by measuring induced torsion. Being Earth based, its sensitivity range is from tens of millihertz to 0.1 Hz, targeting intermediate mass black holes at cosmological distances. Status: Prototype under development [127].

Chapter 5

Overview of Storage Rings

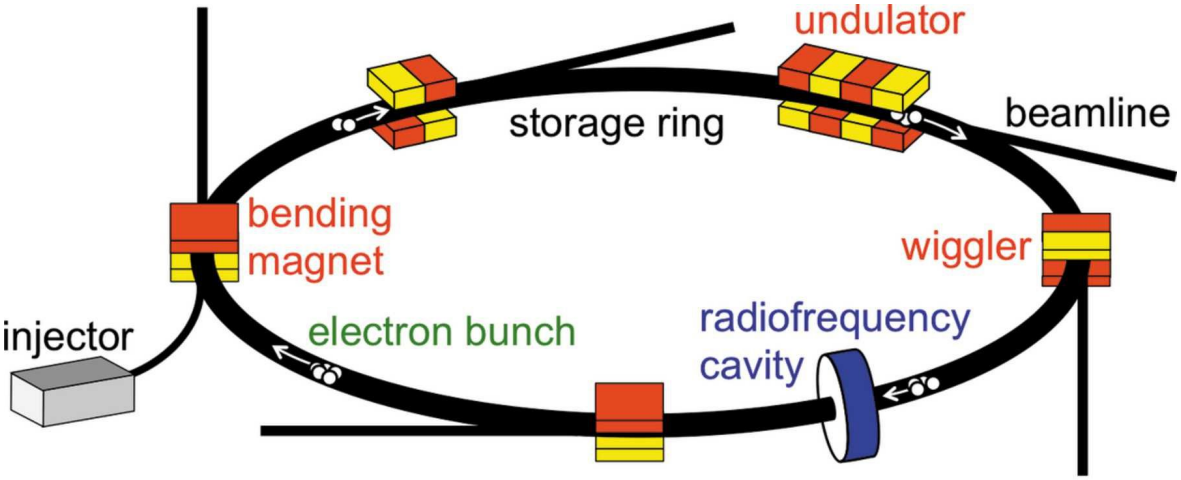

Figure 5.1: The rough schematic of a typical storage ring, adapted with permission from [128]

Storage rings, a sophisticated class of circular particle accelerators, represent a culmination of sophisticated engineering and deep understanding of fundamental physics. Serving as the backbone of numerous groundbreaking experiments, these circular particle accelerators are marvels of human ingenuity, pushing the boundaries of our knowledge about the universe.

Particle storage rings, while distinct from traditional accelerators, play a pivotal role in the landscape of particle physics. Essentially a synchrotron in a static state, these structures are designed not for accelerating particles, but for maintaining their orbits over prolonged periods, often exceeding several hours.

Storage rings are uniquely designed to maintain a continuous or pulsed beam of particles, such as electrons, positrons, protons, or heavy ions, circulating for many hours. The ability of storage rings to stabilize particle beams at high energies makes them invaluable for various scientific investigations.

The inception of the storage ring dates back to 1941, a collaboration between Bruno Touschek and R. Wideroe. Their work, though conducted under constrained circumstances at the University of Hamburg, marked a significant leap in high-energy physics. Their concept was innovative: to use storage rings for colliding beams of particles and antiparticles, thereby facilitating the study of complex elementary particle processes [129, 130].

5.1 Major Components of a Storage Ring

Storage rings are composed of several essential components, each contributing to the effective operation of the facility. Some of them are shown in Fig. (5.1). A typical storage ring consists of the following key components: vacuum chamber, bending magnets, multipole magnets, RF (Radio Frequency) cavities, and beam injection and extraction systems.

5.1.1 Vacuum Chamber

The physics and technology of vacuum chambers in storage rings are crucial for maintaining stability and quality in particle accelerators like synchrotron light sources. Advanced vacuum technology is used to achieve an ultra-high vacuum (UHV) environment, typically around 10^{-9} Torr, essential for preventing electron interference. In certain cases, pressures are maintained between 10^{-8} to 10^{-11} Torr [131, 132].

In terms of gas density, at ultra-high vacuum conditions (10^{-12} mbar), the gas molecule density is approximately 26,500 molecules per cubic centimeter, signifying vast spaces between molecules [133]. This low density is critical for the mean free path of gas molecules, ensuring minimal collisions and interactions within the storage ring's vacuum chamber.

Future advancements in vacuum technology are expected to include incremental improvements in vacuum pumps, particularly cryogenic pumps, and fundamental research on seals and outgassing [134]. There will likely be developments in vacuum gauges, calibration techniques, and leak detectors with enhanced sensitivities. The application of microprocessors and computers in vacuum systems is anticipated to increase [134].

5.1.2 Dipole Magnets

Dipole magnets are the cornerstone of storage rings, responsible for bending the path of charged particles and keeping them in a circular trajectory. These magnets are crucial for maintaining the particles on a circular path. They generate a magnetic field perpendicular to the velocity of the particles, providing the necessary centripetal force. The Lorentz force equation governing the motion of charged particles in a magnetic field is:

$$\vec{F} = q(\vec{v} \times \vec{B}) \tag{5.1}$$

where $\vec{F}$ is the force on a particle with charge q, moving with velocity $\vec{v}$ in a magnetic field $\vec{B}$.

The advent of superconducting technology marked a paradigm shift in storage ring design. Superconducting magnets, due to their ability to conduct electricity without resistance at low temperatures, allow for the generation of significantly

stronger magnetic fields than conventional electromagnets. This advancement is particularly advantageous in bending magnets, where higher magnetic fields permit tighter bending radii, leading to more compact storage ring designs and higher particle energies [135].

5.1.3 Multipole Magnets

Quadrupole magnets play a crucial role in focusing the particle beam, correcting its natural dispersion in both the horizontal and vertical planes. They operate by creating a gradient magnetic field, which varies linearly across the beam path, effectively focusing or defocusing the beam depending on the direction of particle motion relative to the field gradient. Sextupole magnets are employed to correct for chromatic aberrations (a variation in focusing strength with particle energy), thus ensuring beam stability and uniformity.

Beyond quadrupoles and sextupoles, storage rings also utilize higher-order multipole magnets, such as octupoles, to further refine beam dynamics. Octupole magnets are particularly effective in correcting nonlinear beam distortions and improving the overall stability of the beam. The advent of superconducting magnet technology has significantly enhanced the performance of these multipole magnets, allowing for stronger magnetic fields and more compact storage ring designs.

Recent advancements in magnet technology emphasize the importance of precise beam control in achieving high luminosity and minimizing beam loss, key factors in the efficiency and safety of particle accelerators [136, 137].

5.1.4 RF Cavities

RF cavities in storage rings are used to replenish the energy lost by charged particles, primarily due to synchrotron radiation [136]. RF systems in storage rings have evolved significantly, featuring advancements such as higher harmonic cavities and sophisticated feedback mechanisms. These innovations are not merely enhancements; they are pivotal in addressing the challenges posed by higher energy beams. Higher harmonic cavities, for instance, help in flattening the bunch distribution, thereby reducing beam instability and energy spread. They supply an oscillating electric field that imparts energy to the particles in sync with their orbital frequency

$$U_{\mathrm{RF}} = qV_{\mathrm{RF}}\cos(\phi) \tag{5.2}$$

where U_{RF} represents the energy gain per turn, V_{RF} is the RF voltage, and ϕ is the phase angle.

5.1.5 Beam Injection and Extraction Systems

These systems are responsible for inserting particles into the storage ring and extracting them for use in experiments or for directing them to other sections of the accelerator complex.

Injection of particles into a storage ring is a critical procedure. It is usually achieved using pulsed deflecting dipole magnets, known as injection kicker magnets, to steer an incoming train of particles onto the stored beam path. For example, in multi-turn injection, each pulse is carefully placed into the stored beam's phase space, considering factors like radiation damping and beam coherence. The timing of these injections is crucial for maintaining beam stability and size.

5.2 Beam Dynamics and Stability

The operation of storage rings hinges on precise control over beam dynamics. Factors such as synchrotron radiation, beam-beam interactions, and instabilities pose significant challenges. Synchrotron radiation, in particular, is a double-edged sword: while it is a valuable source of X-rays for research, it also leads to energy loss in the particles, necessitating constant acceleration.

$$P_{\text{synch}} = \frac{e^2 c}{6\pi\epsilon_0}\left(\frac{E}{m_0 c^2}\right)^4\left(\frac{v}{R}\right)^2 \tag{5.3}$$

where P_{synch} is the power radiated by a relativistic particle, E is the particle energy, v is the velocity, and R is the radius of curvature of the particle's path.

The stability of particle beams in storage rings is a complex interplay of various forces and interactions. Key to this stability is the concept of radiation damping, which counteracts the spread in particle trajectories due to synchrotron radiation. The radiation damping force can be approximated by:

$$F_{\text{damping}} = -\frac{e^2}{6\pi\epsilon_0 c^3}\gamma^4\left(\frac{d\vec{v}}{dt}\right)^2 \tag{5.4}$$

where γ is the Lorentz factor, and $\frac{d\vec{v}}{dt}$ is the rate of change of velocity.

Beam Cooling Techniques: An essential aspect of modern storage rings is the implementation of beam cooling techniques, crucial for enhancing beam quality by reducing emittance. Electron cooling, where a cold electron beam is merged with the circulating beam to transfer energy and reduce the velocity spread, and stochastic cooling, which employs feedback systems to correct particle distribution, are pivotal in maintaining high-quality, stable beams for prolonged periods. These techniques are increasingly relevant in light of the demand for higher precision in experiments [138].

5.3 Relativistic Considerations

In the realm of storage rings, relativistic effects play a significant role due to the high speeds of circulating particles. Relativistic dynamics are essential for understanding the behavior of particles and for accurate timing measurements, especially in the context of gravitational wave detection. The relativistic energy-momentum relation is given by:

$$E^2 = (pc)^2 + (m_0c^2)^2 \tag{5.5}$$

where E is the total energy, p is the momentum of the particle, c is the speed of light, and m_0 is the rest mass of the particle.

5.4 Beam Diagnostics and Monitoring

The realm of beam diagnostics and monitoring is integral to the efficient operation and safety of storage rings. Modern storage rings are equipped with an array of diagnostic tools, which provide real-time feedback, essential for fine-tuning the accelerator's parameters and ensuring optimal beam quality.

- **Beam Position Monitors (BPMs):** Utilized to precisely measure the position of the beam within the vacuum chamber. BPMs are crucial for aligning the beam and correcting any deviations from the desired trajectory.

- **Beam Emittance Detectors:** These detectors measure the emittance of the beam, a parameter that quantifies the spread of particle trajectories in phase space. Lower emittance is desirable for achieving higher beam quality and brightness.

- **Beam Loss Monitors (BLMs):** Placed along the beam path, BLMs monitor deviations or losses of particles from the main beam, ensuring the safety and efficiency of the accelerator. By identifying the rate and location of particle losses, they enable prompt corrective actions to adjust beam parameters or initiate shutdown procedures, thus preventing damage to accelerator components and ensuring personnel safety. Moreover, data from BLMs are invaluable for optimizing beam performance and providing insights into beam dynamics under different operating conditions.

- **Beam Arrival Time Monitors:** These monitors are key to ensuring the precise timing of the beam's arrival at various points along the storage ring. Accurate beam timing is crucial for synchronization in experiments, especially those requiring time-resolved measurements. By measuring the arrival time of the beam with high precision, these monitors help in maintaining the temporal stability of the beam, enabling experiments that depend on precise timing and synchronization.

5.5 Applications and Future Directions

Storage rings are instrumental in a myriad of applications, from fundamental research in particle physics to practical uses in medicine and industry. They are crucial in studies involving electron-positron collisions and in the generation of synchrotron radiation for materials science, biology, and chemistry. Looking ahead, advancements in storage ring technology, such as novel acceleration techniques and improvements in beam quality and energy efficiency, promise to broaden their scientific and practical applications.

Fundamental Research: Storage rings have been instrumental in numerous scientific breakthroughs, particularly in the field of particle physics. The Large Electron-Positron Collider (LEP) and the Large Hadron Collider (LHC) are prominent examples, where storage rings have facilitated high-energy collisions leading to significant discoveries, including the observation of the Higgs boson [139, 140].

Environmental Science Applications: The application of storage ring technology extends into environmental science, where synchrotron radiation facilitates the analysis of atmospheric particles and environmental pollutants. This research provides critical insights into the mechanisms of climate change and pollution, highlighting the versatility of storage rings beyond traditional physics [141].

Cultural Heritage Science: Synchrotron radiation has also found unique applications in cultural heritage science, offering non-destructive methods for analyzing artworks and archaeological artifacts. This technology has unveiled hidden details in historical paintings and manuscripts, contributing to the preservation and understanding of our cultural heritage [142].

Medical and Industrial Applications: The utility of storage rings extends beyond fundamental research. In the medical field, synchrotron radiation generated by storage rings is used in advanced imaging techniques and targeted radiation therapy, offering new avenues in cancer treatment. In industry, storage rings contribute to material science research and semiconductor manufacturing.

Looking ahead, the evolution of storage ring technology is closely linked to advancements in accelerator physics [143]. Emerging concepts like plasma wakefield acceleration and laser-driven acceleration hold the potential to dramatically reduce the size and cost of storage rings. These novel technologies could democratize access to high-energy physics experiments, paving the way for a new era of scientific discovery. Recent advancements in acceleration technology, such as dielectric laser acceleration (DLA), propose a radical miniaturization of accelerator components. By leveraging the electric field of lasers within dielectric structures, DLAs offer a pathway to significantly more compact and efficient accelerators, promising to revolutionize storage ring technology and its applications in various fields [144].

Chapter 6

Detection of Gravitational Waves in Circular Particle Accelerators

6.1 Preface

This chapter is largely the verbatim presentation of the original research paper (with the same name as the chapter title) of the author of this dissertation and collaborators [145], that has been edited to fit into the structure of this dissertation. The edits consist of some statements written entirely in italics, that have been inserted at the appropriate places within the paper.

6.2 Abstract

Here we calculate the effects of astrophysical gravitational waves (GWs) on the travel times of proton bunch test masses in circular particle accelerators. We show that a high-precision proton bunch time-tagging detector could turn a circular particle accelerator facility into a GW observatory sensitive to millihertz (mHz) GWs. We comment on sources of noise and the technological feasibility of ultrafast single photon detectors by conducting a case study of the Large Hadron Collider (LHC) at CERN.

6.3 Introduction

In 2016, the first direct detection of gravitational waves (GWs) from the merger of two black holes was reported by LIGO [10]. LIGO [18] uses laser interferometry to measure the GW-induced changes in the path length (equivalently, travel time) of light signals. While Earth-based interferometers such as LIGO are sensitive to high-frequency gravitational waves from compact binary mergers, the planned space-based interferometer LISA [28], to be launched in 2034, will be sensitive to millihertz (mHz) GWs [58]. Millihertz GWs are produced by the inspiral, merger and quasi-normal modes of massive black hole binaries, and of extreme and intermediate mass ratio binaries (massive black hole - lighter compact object). They are also produced by white dwarf binaries within our Galaxy, which may be detected as individually

resolved sources or as an unresolved stochastic background [146].

In laser interferometry, the light signals in the interferometer arms carry information about the respective test mass geodesics, making it one possible technique of comparing two or more geodesics, which is the fundamental requirement for detecting any gravitational phenomenon [146]. However, this technique imposes certain design limitations for detecting mHz GWs: first, the test mass mirrors at the ends of the interferometers are subject to gravity gradient (GG) noise (tiny tidal gravitational forces caused by perturbations of the local Newtonian gravitational potential due to human activity, seismic and atmospheric activities, etc.) which increases steeply below 1 Hz [146]. Second, the path length of the laser beams determines the frequency of the GW to which the interferometer is sensitive. The laser path length required for detecting mHz GWs is too large to be realized on Earth, even with multiple reflections of the laser beam between mirrors to fold the path length into a smaller physical space, as this increases the thermal noise [146]. Such path lengths can only be realized with space-based laser interferometers that are relatively free from GG noise.

However, both of the above limitations can be overcome by considering a circular particle accelerator, such as the Large Hadron Collider (LHC) at CERN [147]. Here, the proton bunches act as test masses that are freely falling with a constant speed along the instantaneous tangent to the circular trajectory, and whose circular motion is affected by GWs, which leads to a periodic change in their travel time from its nominal value. Therefore, a fundamental difference between laser interferometry and this GW detection technique is that the former uses stationary test masses confined to rectilinear free-fall along the interferometer arms, while the latter uses moving test masses confined to circular tangential free fall in a particle accelerator.

In an accelerator, two geodesics are compared by the transfer of information via light signals that travel between two clocks which measure time differently: One clock is made up of the circulation of proton bunches, and the other can be a high-precision optical clock connected to a single photon detector. Geodesic information is transferred from the proton bunch clock to the detector clock via visible synchrotron radiation photons emitted by the proton bunches due to the magnetic field. GWs affect the proton bunch clock by changing the geodesics of the proton bunch test masses. This is detected by comparison with the optical clock, which is not affected by GWs in the same way. Here, the travel time of the light signal does not change much due to GWs because the proton bunch is very close to the detector when it transmits photons. This is different from laser interferometry where the GWs induce a change in the light travel time over long distances.

Since the proton bunches in the particle accelerator can, in principle, be confined to a circular trajectory for a very long time, their geodesics can be monitored over a sufficiently long period for mHz GWs to cause a measurable change in the proton bunch travel time.

6.4 Effect of GWs on proton bunch travel times

A GW of astrophysical origin that propagates along the $z_{\rm GW}$-axis in a reference frame $(t, x_p, y_p, z_{\rm GW})$, distorts spacetime in a manner given by the linearized gravity metric in the transverse-traceless gauge [148, 149],

$$dS^2 = -dt^2 + \big(1 + h_+(t)\big)dx_p^2 + \big(1 - h_+(t)\big)dy_p^2 + 2h_\times(t)dx_p dy_p + dz_{\rm GW}^2. \tag{6.1}$$

The $+$ and $\times$ symbols denote the two possible polarizations for the time-varying GW strain. The purely temporal dependence of the GW strain is precise within a region about the origin with a length scale that is small compared to the GW wavelength, otherwise the GW strain would also have a spatial dependence of the form $h_{+,\times}(t, z) = h_{+,\times}(t)\, e^{i(kz-\omega t)}$.

In an observer's reference frame (t, x, y, z), where the GW propagation direction has an azimuth ϕ, inclination θ, and polarization angle ψ, the metric is found by performing a coordinate transformation from $(t, x_p, y_p, z_{\rm GW})$ to (t, x, y, z) via suitable elemental rotations. After doing so and switching to cylindrical coordinates (t, r, α, z), if we set $r = R$, $dr = 0$ and $dz = 0$, we see the effect of GWs along a circular arc of radius R.

Mathematically, this involves tediously substituting into Eq. (6.1), the following coordinate transformation relation,

$$\begin{pmatrix} dt \\ dx_p \\ dy_p \\ dz_{\rm GW} \end{pmatrix} = \begin{pmatrix} 1 & 0 & 0 & 0 \\ 0 & \cos\psi & -\sin\psi & 0 \\ 0 & \sin\psi & \cos\psi & 0 \\ 0 & 0 & 0 & 1 \end{pmatrix} \begin{pmatrix} 1 & 0 & 0 & 0 \\ 0 & \cos\theta & 0 & \sin\theta \\ 0 & 0 & 1 & 0 \\ 0 & -\sin\theta & 0 & \cos\theta \end{pmatrix} \begin{pmatrix} 1 & 0 & 0 & 0 \\ 0 & \cos\phi & -\sin\phi & 0 \\ 0 & \sin\phi & \cos\phi & 0 \\ 0 & 0 & 0 & 1 \end{pmatrix} \begin{pmatrix} dt \\ -R\sin\alpha d\alpha \\ R\cos\alpha d\alpha \\ 0 \end{pmatrix}. \tag{6.2}$$

The effective metric takes the form,

$$dS^2 = -dt^2 + \big(1 + h_{\theta\phi\psi}(t, \alpha)\big)R^2 d\alpha^2, \tag{6.3}$$

and the effective GW strain, $h_{\theta\phi\psi}(t, \alpha)$, has the complex expression,

$$\begin{aligned} h_{\theta\phi\psi}(t, \alpha) = h_+(t)\Big(f_s^+ \sin^2\alpha + f_c^+ \cos^2\alpha + f_{sc}^+ \sin 2\alpha\Big) + \\ h_\times(t)\Big(f_s^\times \sin^2\alpha + f_c^\times \cos^2\alpha + f_{sc}^\times \sin 2\alpha\Big), \end{aligned} \tag{6.4}$$

where,

$$\begin{aligned}
f_s^+ &= (\cos^2\theta\cos^2\phi - \sin^2\phi)\cos 2\psi - (\cos\theta\sin 2\phi)\sin 2\psi,\\
f_c^+ &= (\cos^2\theta\sin^2\phi - \cos^2\phi)\cos 2\psi + (\cos\theta\sin 2\phi)\sin 2\psi,\\
f_{sc}^+ &= \big(\tfrac{1}{2}(1+\cos^2\theta)\sin 2\phi\big)\cos 2\psi + (\cos\theta\cos 2\phi)\sin 2\psi,\\
f_s^\times &= (\cos^2\theta\cos^2\phi - \sin^2\phi)\sin 2\psi + (\cos\theta\sin 2\phi)\cos 2\psi,\\
f_c^\times &= (\cos^2\theta\sin^2\phi - \cos^2\phi)\sin 2\psi - (\cos\theta\sin 2\phi)\cos 2\psi,\\
f_{sc}^\times &= \big(\tfrac{1}{2}(1+\cos^2\theta)\sin 2\phi\big)\sin 2\psi - (\cos\theta\cos 2\phi)\cos 2\psi.
\end{aligned} \tag{6.5}$$

The travel time of test masses in a circular particle accelerator is thus calculated by integrating the timelike geodesic equations of the effective metric,

$$\begin{gathered}
\tfrac{d^2t}{d\tau^2} + \tfrac{1}{2}\tfrac{dh_{\theta\phi\psi}(t)}{dt}\big(\tfrac{dl}{d\tau}\big)^2 = 0,\\
\tfrac{d^2l}{d\tau^2} + \tfrac{1}{1+h_{\theta\phi\psi}(t)}\tfrac{dh_{\theta\phi\psi}(t)}{dt}\big(\tfrac{dl}{d\tau}\big)\big(\tfrac{dt}{d\tau}\big) = 0,\\
-\big(\tfrac{dt}{d\tau}\big)^2 + \big(1+h_{\theta\phi\psi}(t)\big)\big(\tfrac{dl}{d\tau}\big)^2 = g_{\mu\nu}\dot{dx^\mu}\dot{dx^\nu} = -1.
\end{gathered} \tag{6.6}$$

$Rd\alpha = dl$ represents the arc length; $\frac{dt}{d\tau} = \gamma$ is the Lorentz factor; $\frac{dl}{d\tau} = \gamma v$, where v is the circular velocity. Here we write the GW strain as a function of time only, with the foresight that the geodesic solution for the angular coordinate would be a function of time in a circular trajectory, $\alpha = \alpha(t)$. Solving the first and third geodesic equations gives the time-variation of the test mass velocity due to the GWs.

After making the substitutions $\frac{dt}{d\tau} = \gamma$; $\frac{dl}{d\tau} = v\gamma$; $\frac{d^2t}{d\tau^2} = \gamma\frac{d\gamma}{dt}$, the third geodesic equation gives us

$$\gamma^2 v^2 = \frac{\gamma^2 - 1}{1 + h_{\theta\phi\psi}(t)}. \tag{6.7}$$

Substituting the above into the first geodesic equation and rearranging the terms leads to the integrable expression,

$$\frac{2\gamma d\gamma}{\gamma^2 - 1} = \frac{-dh_{\theta\phi\psi}}{1 + h_{\theta\phi\psi}}. \tag{6.8}$$

Upon integrating the above and expressing the Lorentz factor, γ, in terms of the velocity, v, with the limits of the integration going from the initial values, $h_{\theta\phi\psi}(t_0)$, $v(t_0)$, to the final values, $h_{\theta\phi\psi}(t)$, $v(t)$, followed by rearranging the terms, we get the final expression for $v(t)$,

$$v^2(t) = \frac{\big(1 + h_{\theta\phi\psi}(t_0)\big).v^2(t_0)}{\big(1 + h_{\theta\phi\psi}(t_0)\big).v^2(t_0) + \big(1 + h_{\theta\phi\psi}(t)\big).\big(1 - v^2(t_0)\big)}. \tag{6.9}$$

We note that $v(t_0)$, the velocity of the particles at the beginning of the observation run, t_0, differs from that of the nominal case, v_0, and are related as $v^2(t_0) = v_0^2\big(1 + h_{\theta\phi\psi}(t_0)\big)$. This is a result of the frame dependence of velocity measurement for timelike signals. This issue does not exist for lightlike signals, which have a frame-independent, constant velocity. The travel time of the test masses is found by

integrating the third geodesic equation, written as,

$$\big(1 + h_{\theta\phi\psi}(t)\big)dl^2 = v^2(t)dt^2. \tag{6.10}$$

We make the substitution for $v^2(t)$ and use the binomial approximation, as $h_{\theta\phi\psi}(t)$ is small. We revert back to metric units from natural units. Thus, in terms of the constant velocity, v_0, of the nominal case, we get the relation,

$$dl = v_0 dt\left(1 - \Big(1 - \frac{v_0^2}{2c^2}\Big)\big(h_{\theta\phi\psi}(t) - h_{\theta\phi\psi}(t_0)\big)\right). \tag{6.11}$$

In the nominal case, the travel time of a test mass with constant circular velocity v_0, making n (not necessarily whole) turns in a circular accelerator of radius R, is $T = \frac{2\pi nR}{v_0} = \frac{L}{v_0}$. We integrate Eq. (6.11) over the nominal travel time and make the interpretation that for the same travel time, the test mass covers a slightly different path length, by ΔL, in the presence of GWs. Thus, we have,

$$L + \Delta L = v_0 T - v_0\Big(1 - \frac{v_0^2}{2c^2}\Big)\int_{t_0}^{t_0+T}\big(h_{\theta\phi\psi}(t) - h_{\theta\phi\psi}(t_0)\big)dt. \tag{6.12}$$

The change in travel time from its nominal value is therefore, the extra time that the test mass would take to cover the length ΔL, with the final velocity $v(t_0 + T)$. Even so, since we neglect terms of $\mathcal{O}(h^2)$ and higher, the calculation reduces to simply $\frac{-\Delta L}{v_0}$. Thus, in the presence of GWs, the deviation of the test mass travel time from its nominal value is given by the general expression,

$$\Delta T_{\rm GW} = \Big(1 - \frac{v_0^2}{2c^2}\Big)\int_{t_0}^{t_0+T}\big(h_{\theta\phi\psi}(t, \alpha(t)) - h_{\theta\phi\psi}(t_0, \alpha_0)\big)dt. \tag{6.13}$$

The detector is located at an initial angular coordinate α_0, and begins observing at time t_0. Here, we take the angular coordinate of the circulating test mass to vary with time as in the nominal case, $\alpha(t) = \alpha_0 + \frac{v_0}{R}(t - t_0)$, since all terms of order $\mathcal{O}(h^2)$ and higher can be neglected. We may arbitrarily set $\alpha_0 = 0$, since the relative orientation of the GW can be compensated in the choice of the azimuth, ϕ.

We obtain an explicit expression for Eq. (6.13) by making the ansatz, for simplicity, of a linearly polarized sinusoidal GW (see Appendix 6.9 for detailed calculations). Using this assumption, we find that the order of magnitude of the travel time variation over a GW period, $1/f_{\rm GW}$, is

$$\Delta T_{\rm GW} \sim a\frac{h_0}{f_{\rm GW}}, \tag{6.14}$$

where a is a constant of order $\sim 10^{-2}$. Strong mHz GWs with characteristic strain and frequency of order $h_0 \sim 10^{-18}$, $f_{\rm GW} \sim 10^{-4}$ Hz, respectively, would cause, at best, $\Delta T_{\rm GW} \sim 10^{-16}$ s, which corresponds to a shift in test mass positions by $\sim 10^{-8}$ m.

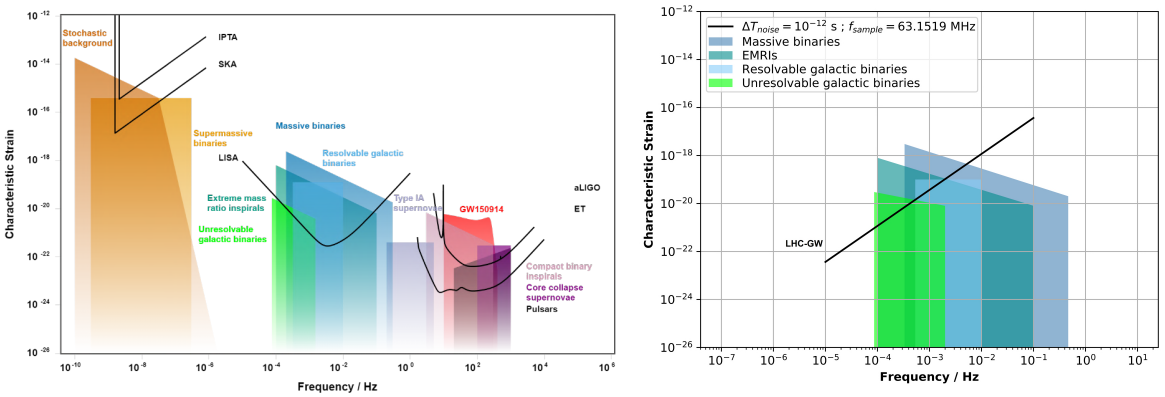

Figure 6.1: The GW sensitivity curves of other GW detectors and the LHC (left panel adopted from [150]). With an overall noise magnitude of $\sim 10^{-12}$ s due to noise sources, and the maximum LHC sampling rate of ≈ 63.1519 MHz, we see that it would be possible to detect the strong mHz GWs produced by extreme mass ratio inspirals, massive black hole binaries and Galactic binaries, resulting in some overlap with the LISA sensitivity curve. GWs from binary supermassive black holes are also accessible in principle, but detecting them would require continuous measurements over unfeasibly long periods ($> 10^6$ s).

6.5 GW Sensitivity Curve

Separate timing detectors would need to time-tag the proton bunches constituting the counter-rotating, ultrarelativistic proton beams in the two LHC vacuum tubes, which can be made to circulate without collisions. The LHC utilizes superconducting electromagnets along with beam collimators to impose a highly precise circular trajectory of the proton bunches in the focused proton beam. Further, the LHC Radiofrequency (RF) system [151] keeps the proton bunches circulating at a constant speed and also maintains the bunch length (≈ 30 cm) of the 2808 proton bunches separated by ≈ 25 ns travel time. In the presence of strong mHz GWs, the travel time of all proton bunches will periodically deviate from its nominal value of $\approx n \times 89\,\mu$s (n being the fractional number of revolutions and $89\,\mu$s the revolution period) in a continuous manner by up to $\Delta T_{\rm GW} \sim 10^{-16}$ s, with a frequency of $f_{\rm GW}$. Every timing measurement is, therefore, a sample of the continuous, time-varying GW signal.

Each LHC vacuum tube can contain 2808 proton bunches, circulating at $\approx 11,245$ Hz. Hence, the maximum sampling rate (i.e. the rate at which the detectors time-tag the proton bunches) at the LHC is $\approx 2 \times 2808 \times 11245 = 63.1519$ MHz. A high sampling rate improves signal detection by improving noise filtering techniques such as matched filtering [146], thus potentially enabling the detection of the GW signal even if it is buried within the noise caused by various error sources which perturb the proton bunch travel time or its measurement. To detect GWs, the travel time difference magnitude due to GWs given by Eq. (6.14), must be greater than the overall noise magnitude, $\Delta T_{\rm noise}$. However, employing matched filtering, the effective noise is reduced by the square root of the number of data-points taken within the observing

time i.e. the sampling rate, $f_{\rm sample}$, times the observing time, T_{obs}. Hence, we have

$$\Delta T_{\rm GW} \gtrsim \frac{\Delta T_{\rm noise}}{\sqrt{f_{\rm sample}\, T_{\rm obs}}}. \tag{6.15}$$

We assume that the significant portion of the GW signal lasts for a duration of 10 times its period, i.e. $T_{\rm obs} \sim 10/f_{\rm GW}$. Inserting this in the above inequality, and the time-difference magnitude estimate Eq. (6.14) for a circular accelerator GW observatory, we obtain the LHC-GW sensitivity curve, shown in Fig. 6.1,

$$h_0 \gtrsim \frac{b\,\Delta T_{\rm noise}}{\sqrt{f_{\rm sample}}}(f_{\rm GW})^{3/2}, \tag{6.16}$$

where b is a constant of order 10.

Our initial construction of the sensitivity curve, although conveying the correct information within its context, was not aligned with the convention followed by the GW community. This was later updated in Sec. 7.6.2, and further details can be found in App. B.

6.6 Noise sources

Below, we estimate the magnitudes of various sources of noise in terms of the nominal proton bunch travel time, T:

6.6.1 Quantum noise

The uncertainty principle sets a lower limit on the proton bunch timing uncertainty. The uncertainty in the relativistic momentum of the test mass, in terms of the uncertainty in its velocity, is given by,

$$\Delta p = m_0 \Delta(\gamma v)\Big|_{v=v_0} = m_0\Big(1-\frac{v_0^2}{c^2}\Big)^{-3/2}\Delta v. \tag{6.17}$$

Therefore, the uncertainty relation reads,

$$\Delta L \sim \frac{\hbar}{2}.\frac{1}{m_0\Delta v}\Big(1-\frac{v_0^2}{c^2}\Big)^{3/2}. \tag{6.18}$$

Since the travel time is $T = L/v_0$, the uncertainty in timing due to uncertainties in position and velocity measurements is given by,

$$\Delta T = \frac{\Delta L}{v_0} + \frac{L\Delta v}{v_0^2}. \tag{6.19}$$

Substituting ΔL and $L = v_0 T$, we get,

$$\Delta T \sim \frac{\hbar}{2m_0 v_0}\left(1 - \frac{v_0^2}{c^2}\right)^{3/2}\frac{1}{\Delta v} + \frac{T}{v_0}\Delta v. \tag{6.20}$$

The timing uncertainty can be minimized for a suitable uncertainty of velocity measurement, giving,

$$\Delta T \sim \sqrt{\frac{2\hbar T}{m_0}}\frac{1}{v_0}\left(1 - \frac{v_0^2}{c^2}\right)^{3/4}. \tag{6.21}$$

In the LHC, protons circulate with a period of $\approx 89\,\mu$s at a speed which is approximately 3 m/s slower than the speed of light. Assuming that a detection takes place every revolution, then the quantum noise is,

$$\Delta T_{\text{quantum}} \sim 10^{-20} s. \tag{6.22}$$

6.6.2 Gravity gradient (GG) noise

GG noise, unlike GWs, is a tidal gravitational effect. For interferometric GW detectors, GG noise mimics the effect of a stochastic background of GWs, and is dominant at low frequencies [152, 153]. In the LHC, ultra-relativistic proton bunches circulate with a frequency of $\approx 11,245$ Hz, at an underground depth of 50-175 m. The travel time change caused by tidal gravitational forces due to terrestrial and non-terrestrial masses acting directly on the proton bunches would be greatly attenuated by their high frequency circulation. To show this, we make a simple estimate using a classical treatment, by considering the tidal gravitational acceleration on the proton bunches due to a mass M, at a distance R. For terrestrial masses close to the LHC, we find,

$$\Delta T_{\text{GG}} \sim \left(\frac{GM}{2hv_0^2}\right)T, \tag{6.23}$$

where h is the depth of the LHC below the mass, and v_0 is the circular speed of the proton bunches, close to the speed of light. For a typical 250,000 ton skyscraper of a few hundred meters height, the GG noise over a duration of $T = 10^4$ s is $\Delta T_{\text{GG}} \sim 10^{-18}$ s, but in reality this value would be roughly averaged out due to all the masses surrounding the LHC, making the GG noise due to nearby terrestrial objects negligible compared to the effect of mHz GWs. On the other hand, for masses far away from the LHC, we find,

$$\Delta T_{\text{GG}} \sim \left(\frac{2GML^2}{R^3\pi v_0^2}\right)T, \tag{6.24}$$

where L is the circumference of the LHC (≈ 26.7 km). Over a duration of $T = 10^4$ s, the tides due to the Sun and Moon (even if assumed to be aligned during New Moon and having a fixed, edge-on orientation with the LHC ring), would cause $\Delta T_{GG} \sim 10^{-18}$ s. Actually, this value would be even smaller due to a changing orientation caused by Earth's rotation and misalignment between the Sun and the Moon. However, the tides also cause a slight deformation of the LHC tunnel (by ≈ 1

mm), over the period of a day [154]. A radial feedback loop allows the RF system to continuously correct the proton beam orbit, keeping it centered [155, 156]. The long-term proton bunch travel time variation due to this effect can therefore be fully predicted and accounted for. Finally, we find that the Alps mountains located closer than a few hundred kilometers from LHC can also cause a significant GG noise. For the Mont Blanc, which is roughly 100 km away from the LHC, assuming a typical mass of 10^{14} kg, we estimate $\Delta T_{\rm GG} \sim 10^{-16}$ s over a duration of $T = 10^4$ s. However, the local gravity gradient across the LHC can be mapped in detail to completely account for the net GG noise due to all stationary terrestrial mass distributions.

6.6.3 Seismic noise

Incoherent ambient seismic activity is the major source of mechanical vibrations that can cause relative motion between the LHC dipole magnets, leading to small deformations (by $\sim \mu$m) of the proton beam orbit [157, 158, 159, 160]. However, mechanical vibrations cannot affect the longitudinal dynamics of the proton bunches since they couple only via the magnetic field. We make a simple estimate of seismic noise on the proton bunch travel times: If laid out in a straight line, the deformed orbit can be modelled as a sine wave about the ideal orbit. The deviation of the deformed orbit from the ideal orbit at a position x and time t is given by

$$y = y_0 \sin\left(2\pi f_s t\right) \sin\left(\frac{n\pi x}{L}\right), \tag{6.25}$$

where L is the circumference of the ideal orbit (≈ 26.7 km for LHC); f_s is the frequency of seismic waves; n is the harmonic number (number of antinodes of the deformed orbit with respect to the ideal orbit when laid out in a straight line over one revolution). The small deviation of travel time is proportional to the difference in path lengths of the deformed and ideal orbits,

$$v_0 \Delta T = \frac{1}{2} \int_0^T \left(\frac{dy}{dx}\right)^2 \Big|_{x=v_0 t} v_0 dt. \tag{6.26}$$

For low-frequency seismic waves, we find the estimate,

$$\Delta T = \frac{n^2 \pi^2 y_0^2}{8L^2} \left(T - \frac{\sin\left(4\pi f_s T\right)}{4\pi f_s}\right). \tag{6.27}$$

For mHz seismic waves causing an orbit deformation of $y_0 \sim \mu$m with low harmonic number, and a duration of $T = 10^4$ s, the seismic noise is,

$$\Delta T_{\rm seismic} \sim 10^{-17} s. \tag{6.28}$$

An orbit correction mechanism such as the radial feedback loop of the RF system, which can reduce the orbit deformation amplitude, will further reduce the seismic noise on the proton bunches. Lastly, the detector itself will also be directly affected by seismic vibrations, causing a significant seismic noise. To overcome this issue,

a technological solution may be employed similar to the VIRGO interferometer, whose Superattenuators can attenuate seismic vibrations by more than 10 orders of magnitude [161].

6.6.4 Radiofrequency phase noise

The precision of the RF system implementation (responsible for controlling the constant speed of the proton bunches, the bunch length, the separation between the bunches and their arrival in-phase with the oscillating electric field) leads to a jitter of the proton bunch travel times, causing a noise with a magnitude of $\Delta T_{\mathrm{RF}} \sim 10^{-12}$ s on the timescale of the measurement [162]. A correction for bunch elongation over time of around 8 ps/hr in the stable beam [162] must also be taken into account in the models.

6.6.5 Detector noise

The Longitudinal Density Monitor (LDM) [163] is an existing detector at the LHC, suitable for this GW detection technique. It is a single photon counting system with a timing jitter of $\Delta T_{detector} = 50$ ps and dead time (duration of instrument unresponsiveness between two consecutive detections) of 77 ns that detects the visible synchrotron radiation emitted by the proton bunches to measure their longitudinal profile.

6.6.6 Photon shot noise

The inverse of the average photon arrival rate at the detector is the additional jitter on the proton bunch time-tagging, as the arrival time of a photon at the detector can roughly vary by this value for every proton bunch. The synchrotron radiation emission pattern for ultrarelativistic protons is sharply collimated forward along the velocity of the proton, with an opening angle of $1/\gamma \sim 10^{-3}$ degrees. For a proton bunch of ≈ 30 cm traversing the $L \approx 26.7$ km LHC circumference, the emission patterns of the constituent $\sim 10^{11}$ protons significantly overlap. From the Liénard-Wiechert formulation of synchrotron radiation due to a bending magnetic field, the average power received by the detector over all frequencies and all solid angle as the synchrotron radiation from a proton bunch sweeps across the detector, is

$$\langle P \rangle_{\mathrm{sync}} \sim 10^{11} \times \frac{2\pi e^2 c \beta^4 \gamma^4}{3\epsilon_0 L^2} \sim 10^{-1} W. \tag{6.29}$$

Where $\beta = v_0/c$ and γ is the Lorentz factor. Considering the frequency distribution of the radiated energy, we obtain the equivalent frequency, ν_{eq}, which gives for the total energy radiated, the same total number of photons:

$$\nu_{eq} \sim \frac{\gamma^3 c}{L} \sim 10^{16} Hz. \tag{6.30}$$

Thus, the inverse of the average arrival rate of photons at the detector, which is the photon shot noise, is estimated to be

$$\Delta T_{\text{photon}} \sim \left(\frac{\langle P \rangle_{\text{sync}}}{h\nu_{eq}} \right)^{-1} \sim 10^{-17} s. \tag{6.31}$$

Since the above calculation is over all frequencies, we interpret that increasing the bandwidth of the detector can reduce the true noise below the required threshold. Moreover, the time-tagging would be less accurate near the edges of the emission pattern, where the power per solid angle is much less.

6.7 Discussion

Presently, the significant noise at LHC is due to the detector timing jitter of 50 ps, and the sampling rate is limited by the detector dead time of 77 ns, which is longer than the bunch length ($\approx$ 1 ns) and the separation between proton bunches ($\approx$ 25 ns). But already, new technology such as superconducting nanowire single-photon detectors (SNSPDs) offer a low timing jitter of a few ps [164], high photon count rate (inverse of the dead time) of a few GHz [165], low dark count rate (rate of recording false counts) of 10^{-3} Hz [166] and high detection efficiency (probability of detecting a photon which arrives at the detector) of around 98% [167], while also showing the potential for realizing a single device with all these merits [168]. Moreover, SNSPDs can function over a broad wavelength range [169] including the visible-UV range, even in the presence of strong magnetic fields [170]. A high-efficiency, broadband detection system with $\approx$ 1 ps timing jitter and $\approx$ 1 GHz count rate which can detect a few photons per proton bunch, would allow the accurate time-tagging of every LHC proton bunch consecutively and continuously, thus reaching the sampling rate of $\approx 63.1519/2$ MHz per vacuum tube. Importantly, the detection system must have a suitable timing precision (least count) that is smaller by a few orders of magnitude than the expected peak signal strength due to GWs, in order to detect the whole waveform. The latest optical clocks offer a timing precision of $\sim 10^{-19}$ s [171].

We observe that in this detection technique, certain noise sources such as gravity gradient noise and seismic noise always act as “drag" i.e. which tend to continually build up a time delay in the proton bunch time tagging while causing no significant timing jitter. This is in contrast to laser interferometry, where these same noise sources tend instead to mimic a stochastic GW background. Meanwhile, the other noise sources in this detection technique cause only a timing jitter.

In the LHC, the RF system is present only at certain points of the circular accelerator ring. The ideal RF system causes no acceleration to be experienced by those particles which travel through it with the correct speed and timing (synchronous particles), while all other particles in the proton bunch perform longitudinal oscillations about the synchronous particle while traveling (synchrotron oscillations), because the RF system causes all non-synchronous particles to experience a suitable accelera-

tion that tends to restore the synchronous parameters. Since an LHC proton bunch consists of $\sim 10^{11}$ particles, let us assume a continuous velocity distribution of the particles having a tiny spread around the mean (which is the synchronous velocity), and also a continuous position distribution with a spread equal to the bunch length. Considering this picture, we see that in spite of the presence of an RF system, the effect of GWs (which would equally affect all particles in the proton bunch) would be to cause continuous, small and slow (relative to the synchrotron oscillations) periodic shifts of the particle velocities and positions, as given by Eq. (6.9) and Eq. (6.13) respectively. Hence, we can expect the GW signal to be present in the travel time information of the proton bunches in a circular particle accelerator.

Note that the above paragraph was found to be incorrect, and primitive models by D'Agnolo et al. (see Sec 2.6 of [172]) showed that we can expect the RF system to act as a damping mechanism to the expected GW signal, reducing its sensitivity, but not cancelling the GW signal entirely.

For determining the location of an astrophysical GW source, triangulation via the time delay between three or more GW observatories at different locations detecting the same event is needed, as done by the extended LIGO/VIRGO collaboration [173]. The space-based LISA detectors are expected to have a sky-localization of 1-100 $\deg^2$, which can improve in a network with other space-based detectors [174]. The LISA orbit would lag the Earth orbit by ≈ 20 degrees, implying an optimistic improvement by roughly 1.5 orders of magnitude of the angular resolution, for massive binary GW events detected by both LISA and LHC. Thus, the network of LISA with the potential LHC-GW observatory can achieve a significantly higher precision of localizing the GW source in the sky.

While probing mHz GWs with any Earth-based detector, the orientation of the GW with respect to the detector would vary significantly (by more than 10 degrees) over the detection period due to the Earth's rotation, and therefore, this must be taken into account in the models (see Appendix 6.10). This may change the response of the detector if the GW orientation becomes aligned differently with the antenna pattern, shown in Fig. 6.2.

6.8 Conclusion

We conclude that a high-frequency, low timing jitter and high-precision proton bunch time-tagging detector could turn a circular particle accelerator facility into a GW observatory sensitive to mHz GWs.

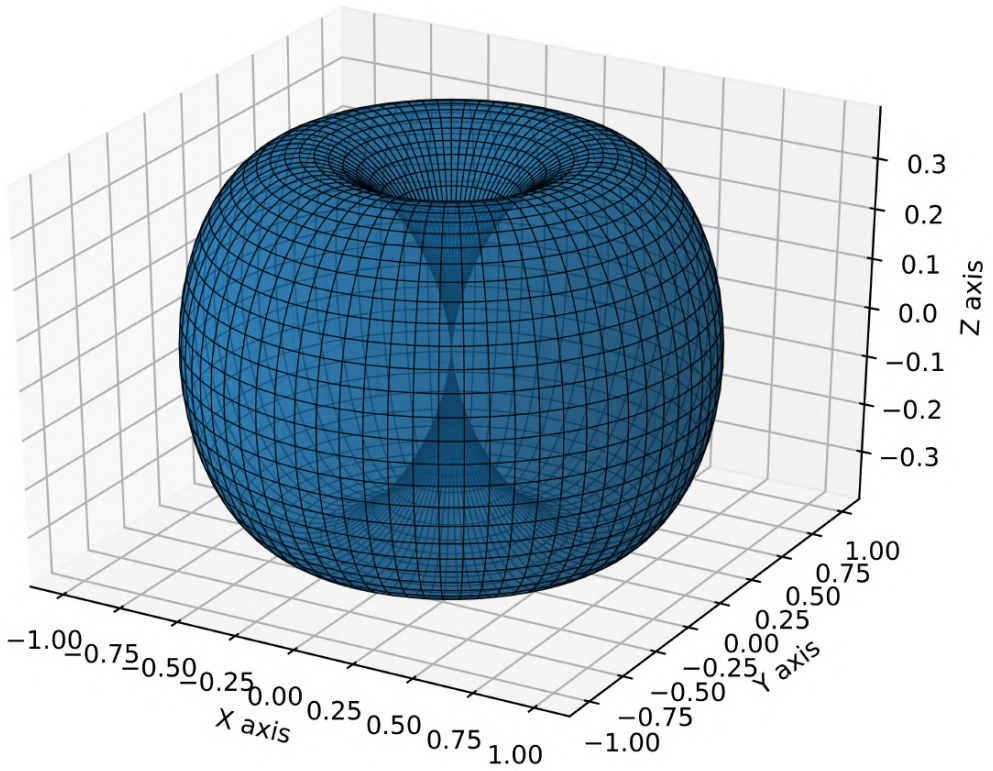

Figure 6.2: The LHC-GW antenna pattern. Shown here is the approximate 'pointing' of a circular particle accelerator GW observatory, rms-averaged over all possible GW polarization angles (see Appendix 6.9). The origin lies at the center of the circular accelerator with the z-axis being perpendicular to its plane.

6.9 Sinusoidal GW ansatz, time-difference magnitude and antenna pattern

In Eq. (6.4), we ignore the cross polarization term (effectively assuming a linearly polarized GW), and use a sinusoidal ansatz of the time-varying GW strain,

$$h_+(t) = h_0 \sin(2\pi f_{GW} t). \tag{6.32}$$

We substitute Eq. (6.4) in the general expression for the travel time change,

$$\Delta T_{\rm GW} = \left(1 - \frac{v_0^2}{2c^2}\right) \int_{t_0}^{t_0+T} \left(h_{\theta\phi\psi}(t, \alpha(t)) - h_{\theta\phi\psi}(t_0, \alpha_0)\right) dt. \tag{6.33}$$

In the nominal case, the travel-time of particles with constant circular velocity v_0, making n (not necessarily whole) turns in a circular accelerator of radius R is $T = \frac{2\pi n R}{v_0}$. The observing run begins at time t_0, from an angular coordinate, α_0, of the

detector's location. We may arbitrarily set $\alpha_0 = 0$, since the relative orientation of the GW can be compensated in the choice of the azimuth, ϕ. This fixes the x-axis to pass through the detector location. And, we take $\alpha(t) = \frac{v_0}{R}(t - t_0)$, since all terms of order $\mathcal{O}(h^2)$ and higher can be neglected. Therefore, we have,

$$\begin{aligned}\Delta T_{GW} = \quad & h_0\Big(1 - \frac{v_0^2}{2c^2}\Big) \\ & \Bigg(f_s^+ \int_{t_0}^{t_0+T} \sin\left(2\pi f_{GW} t\right) \sin^2\Big(\frac{v_0}{R}(t - t_0)\Big) dt \\ & + f_c^+ \int_{t_0}^{t_0+T} \sin\left(2\pi f_{GW} t\right) \cos^2\Big(\frac{v_0}{R}(t - t_0)\Big) dt \\ & + f_{sc}^+ \int_{t_0}^{t_0+T} \sin\left(2\pi f_{GW} t\right) \sin\Big(2\frac{v_0}{R}(t - t_0)\Big) dt \\ & - f_c^+ T \sin\left(2\pi f_{GW} t_0\right) \Bigg).\end{aligned} \tag{6.34}$$

Solving the time integral, and using $T = \frac{2\pi n R}{v_0}$, we get,

$$\begin{aligned}\Delta T_{GW} = \quad & h_0\Big(1 - \frac{v_0^2}{2c^2}\Big) \times \\ & \Bigg(\frac{(f_s^+ + f_c^+)}{2\pi f_{GW}} \sin\left(\pi f_{GW} T + 2\pi f_{GW} t_0\right) \times \\ & \sin\left(\pi f_{GW} T\right) - f_c^+ T \sin\left(2\pi f_{GW} t_0\right) \\ & + \frac{(f_s^+ - f_c^+)}{4\pi} . \frac{T}{f_{GW} T + 2n} \sin\left(\pi f_{GW} T + 2\pi n\right) \times \\ & \sin\left(\pi f_{GW} T + 2\pi n + 2\pi f_{GW} t_0\right) \\ & + \frac{(f_s^+ - f_c^+)}{4\pi} . \frac{T}{f_{GW} T - 2n} \sin\left(\pi f_{GW} T - 2\pi n\right) \times \\ & \sin\left(\pi f_{GW} T - 2\pi n + 2\pi f_{GW} t_0\right) \\ & + \frac{f_{sc}^+}{4\pi} . \frac{T}{f_{GW} T - 2n} \cos\left(\pi f_{GW} T - 2\pi n\right) \times \\ & \sin\left(\pi f_{GW} T - 2\pi n + 2\pi f_{GW} t_0\right) \\ & - \frac{f_{sc}^+}{4\pi} . \frac{T}{f_{GW} T + 2n} \cos\left(\pi f_{GW} T + 2\pi n\right) \times \\ & \sin\left(\pi f_{GW} T + 2\pi n + 2\pi f_{GW} t_0\right) \Bigg).\end{aligned} \tag{6.35}$$

If v_0 is large, close to light-speed (as is usually achieved in particle accelerators such as the LHC at CERN), implying that n is also large, then the last four terms in the above result vanish, and the coefficient outside becomes $1/2$, leaving us with the

result,

$$\Delta T_{GW} = \frac{1}{2}\frac{h_0}{f_{GW}}\left(\frac{(f_s^+ + f_c^+)}{2\pi}.\sin(\pi f_{GW}T + 2\pi f_{GW}t_0) \times \sin(\pi f_{GW}T) - f_c^+.f_{GW}T.\sin(2\pi f_{GW}t_0)\right). \tag{6.36}$$

The phase term, $2\pi f_{GW}t_0$, signifies the effect on the travel time change, of the initial phase of the periodic GW signal at the beginning of the observing run, t_0, and here, $t_0 = 0$ corresponds to phase 0. Since it is highly likely that there are no GWs at the beginning of an observing run, the condition $t_0 = 0$ applies, giving the final result,

$$\Delta T_{GW} = -\frac{1}{4\pi}\frac{h_0}{f_{GW}}.F_+.\sin^2(\pi f_{GW}T), \tag{6.37}$$

$$F_+ = \sin^2\theta\cos 2\psi. \tag{6.38}$$

Taking an rms-average over angular parameters (θ, ψ) of Eq. (6.37), we find the order of magnitude of travel time change due to GWs, of test mass particles in a circular accelerator, over the GW period $1/f_{GW}$, to be,

$$\Delta T_{GW} \sim \frac{\sqrt{3}}{16\pi}\frac{h_0}{f_{GW}}. \tag{6.39}$$

The antenna-pattern of this GW detector, rms-averaged over all GW polarization angles, is given by

$$\overline{F_+} = \left(\frac{1}{2\pi}\int_0^{2\pi}\sin^4\theta\cos^2 2\psi.d\psi\right)^{1/2} \sim \sin^2\theta. \tag{6.40}$$

6.10 Effect of Earth's rotation

The change in travel time given by Eq. (6.33) must be recalculated by considering the time-varying GW orientation due to Earth's rotation, $\theta(t), \phi(t), \psi(t)$, the terms corresponding to which would now be inside the time integral, which must be evaluated numerically.

The following relation establishes the connection between the time-varying GW orientation $\theta(t), \phi(t), \psi(t)$, as measured from a moving coordinate system on Earth with its origin at the center of the circular accelerator, (x, y, z), and the equatorial

celestial coordinate system, in which the orientation of the GW is fixed:-

$$\begin{pmatrix} \cos\psi & -\sin\psi & 0 \\ \sin\psi & \cos\psi & 0 \\ 0 & 0 & 1 \end{pmatrix} \begin{pmatrix} \cos\theta & 0 & \sin\theta \\ 0 & 1 & 0 \\ -\sin\theta & 0 & \cos\theta \end{pmatrix} \begin{pmatrix} \cos\phi & -\sin\phi & 0 \\ \sin\phi & \cos\phi & 0 \\ 0 & 0 & 1 \end{pmatrix} = \begin{pmatrix} \cos\psi_{eq} & -\sin\psi_{eq} & 0 \\ \sin\psi_{eq} & \cos\psi_{eq} & 0 \\ 0 & 0 & 1 \end{pmatrix} \begin{pmatrix} \cos\left(\frac{\pi}{2}-\delta_{GW}\right) & 0 & \sin\left(\frac{\pi}{2}-\delta_{GW}\right) \\ 0 & 1 & 0 \\ -\sin\left(\frac{\pi}{2}-\delta_{GW}\right) & 0 & \cos\left(\frac{\pi}{2}-\delta_{GW}\right) \end{pmatrix} \begin{pmatrix} \cos\omega_e\big(\alpha_{GW}-l_0-(t-t_0)\big) & -\sin\omega_e\big(\alpha_{GW}-l_0-(t-t_0)\big) & 0 \\ \sin\omega_e\big(\alpha_{GW}-l_0-(t-t_0)\big) & \cos\omega_e\big(\alpha_{GW}-l_0-(t-t_0)\big) & 0 \\ 0 & 0 & 1 \end{pmatrix} \begin{pmatrix} \cos\left(\frac{\pi}{2}-\theta_{lat}\right) & 0 & -\sin\left(\frac{\pi}{2}-\theta_{lat}\right) \\ 0 & 1 & 0 \\ \sin\left(\frac{\pi}{2}-\theta_{lat}\right) & 0 & \cos\left(\frac{\pi}{2}-\theta_{lat}\right) \end{pmatrix} \begin{pmatrix} \cos\psi_0 & -\sin\psi_0 & 0 \\ \sin\psi_0 & \cos\psi_0 & 0 \\ 0 & 0 & 1 \end{pmatrix}. \quad (6.41)$$

ω_e is the angular speed of Earth's rotation. α_{GW}, δ_{GW} are the RA and DEC of the GW propagation direction. ψ_{eq} is the polarization of the GW in the equatorial celestial coordinates. ψ_0 is the angle between the line joining the center of the circular accelerator to the timing detector and the longitude passing through the center of the circular accelerator. l_0 and θ_{lat} are respectively, the local sidereal time at the beginning of the observing run and latitude of the center of the circular accelerator.

Chapter 7

Detection of Gravitational Waves in Circular Particle Accelerators II. Response Analysis and Parameter Estimation Using Synthetic Data

7.1 Preface

This chapter is largely the verbatim presentation of the original research paper of the author of this dissertation and collaborators (with the same name as the chapter title) [175], submitted to Physical Review D for peer review and publication, that has been edited to fit into the structure of this dissertation. This is the sequel to [145], the paper on which the previous chapter is based. Relative to the previous chapter, this chapter shows further progress of the understanding of this novel experiment concept that was made in the previous years.

7.2 Abstract

We simulate the response of a Storage Ring Gravitational-Wave Observatory (SRGO) to astrophysical millihertz (mHz) gravitational waves (GWs), numerically obtaining its sensitivity curve and optimal choices for some controllable experiment parameters. We also generate synthetic noisy GW data and use Markov Chain Monte Carlo (MCMC) methods to perform parameter estimation of the source properties and their degeneracies. We show that a single SRGO could potentially localize the GW source in the sky using Earth's rotation. We also study the source sky localization area, mass and distance estimation errors as functions of noise, data sampling rate, and observing time. Finally, we discuss, along with its implications, the capacity of an SRGO to detect and constrain the parameters of millihertz GW events.

7.3 Introduction

Theoretical studies of gravitational waves (GWs) interacting with storage rings (circular particle accelerators where beams of charged particles circulate without collisions for long periods of time), intending to explore the possibility of using storage rings as GW detectors, have been conducted independently by several authors over the past decades [176, 177, 178, 179, 180].

However, these studies only considered the scenario of GWs propagating perpendicularly to the plane of the storage ring (i.e., a “face-on" orientation). This particular orientation maximizes the GW-induced oscillations of the charged test mass particles circulating in the ring (which we will refer to as “ions" henceforth) along the ring’s radial direction. Thus, one can hope to exploit resonances with the beam’s betatron oscillations and detect the presence of GWs using beam position monitors. However, as storage ring betatron frequencies generally fall in a range where no significant astrophysical GW sources exist, and since these radial oscillations are expected to be extremely small, this idea did not seem very promising.

In our previous paper [145], henceforth referred to as paper I, we instead discussed the possibility of detecting GWs by monitoring the circulation time of the ions instead of their orbit shape. We expect the circulation time of the ions to be affected by a passing GW not just because of the above-mentioned orbit shape distortion but also because of a GW-induced change in the velocity of the ions. While the former effect is, in general, proportional to h^2 (where h is the dimensionless GW strain, see Appendix 7.10), the key insight from paper I was that the latter is, in general, proportional to h. It is only in the special case of a face-on orientation of the storage ring, where a GW can only cause a beam shape distortion, that the latter effect vanishes, leaving only the former, much smaller effect. Since previous studies had only considered this special case, it was prematurely concluded that a detection of GWs by monitoring the circulation time of the ions was unfeasible. The realisation from paper I that the effect of the GW-induced change in the velocity of the ions on their circulation time is in general proportional to h clearly changes this assessment.

Moreover, in paper I we also showed that the circulation time deviation induced by a GW has a periodicity equal to that of the GW, suggesting that it builds up over time during the first half of a GW period and then wanes during its second half. In addition, the peak value of the signal is proportional to the GW period, making a storage ring GW detector more sensitive to lower frequency GWs. Importantly, we showed in paper I that, due to an overlap of several conditions, a Storage Ring Gravitational Wave Observatory (SRGO) would be most sensitive to the yet undetected millihertz (mHz) GWs from astrophysical sources that are also targeted by future space-based GW detectors such as the Laser Interferometer Space Antenna (LISA) [28, 58].

The quantity measured by an SRGO would be analogous to the “timing residuals" measured by pulsar timing arrays (PTAs), which are the GW-induced arrival-time

deviations of radio pulses produced by millisecond pulsars from their expected, highly regular arrival times in the absence of GWs and noise sources [181]. Moreover, using ions as moving test masses in an SRGO to detect GWs is similar to the idea of GW detection by atom interferometry, where ballistic atoms are used as test masses [182, 122, 123, 124, 125].

Recently, D'Agnolo et al. independently derived the expected GW-induced circulation time deviation of ions in an SRGO which is in agreement with our results from paper I, under the condition that no radio frequency (RF) system is present in the storage ring (see Sec 2.6 of [172]). Therefore, the general relativistic calculations for an SRGO using two different approaches (metric formalism in our paper I, and Riemann tensor formalism by D'Agnolo et al.), give, effectively, the same result.

In paper I, we considered the Large Hadron Collider (LHC) at CERN as an existing facility that could potentially be turned into an SRGO. However, the LHC is not the ideal facility to realize the SRGO detector because the presence of an RF system in the storage ring would dampen the GW signal that we hope to detect [172]. Instead, rings capable of storing coasting (i.e., without interference by an RF system) "crystalline ion beams" [183, 184, 185] or rings that could potentially store a single circulating ion [186] may be better laboratories for detecting GWs. Moreover, there are better options for the ion time-tagging detector technology than that proposed in paper I, such as "beam arrival time monitors" [187], which are electro-optic charge centroid monitors providing femtosecond timing precision. Also, improving the vacuum quality inside storage rings would enable sustaining stable, coasting ion beams or single ions for longer periods, allowing for longer SRGO observation runs.

In this paper we continue our investigation from paper I, improving on some previous results, and exploring new areas with an updated theoretical formalism and numerical simulations. The rest of this paper is organized as follows: in Sec. 7.4, we provide an updated theoretical framework for an SRGO. In Sec. 7.5, we provide the mathematical models and numerical procedures used in this investigation. Sec. 7.6.1 presents the SRGO response function and its variation with various parameters. In Sec. 7.7, we study the estimation of GW source parameters with an SRGO using artificial noisy data. Finally, In Sec. 7.8, we discuss various aspects of our study, and we summarize our main results in Sec. 7.9.

7.4 Review and revision of SRGO basics

Using the metric formalism of general relativity, in paper I, we derived the circulation time deviation of test masses in a storage ring due to GWs relative to the circulation time in the absence of any GWs. Here, we revise some of these results and display them in a more concise form. We recall from Eq. (10) of paper I that the circulation time deviation (relative to the case of no GWs) is given by the expression

$$\Delta T_{\rm GW}(T) = \left(1 - \frac{v_0^2}{2c^2}\right) \int_{t_0}^{t_0+T} \left(h_{\theta\phi\psi}(t, \alpha(t)) - h_{\theta\phi\psi}(t_0, \alpha_0)\right) dt, \tag{7.1}$$

where v_0 is the constant speed of the ions in the absence of any GWs, c is the speed of light, t_0 is the time of the start of the monitoring campaign, and T is the duration of the monitoring campaign. $h_{\theta\phi\psi}$ is a function of the GW strain amplitudes, $h_{+,\times}(t)$, the orientation of the GW with respect to the ring, parameterized by the three angles $\theta(t), \phi(t)$, and $\psi(t)$, which vary with time due to the Earth's rotation, and the angular trajectory of the ions in the ring, $\alpha(t)$.

We recall from paper I that ϕ, θ and ψ are the Euler angles which transform the observer's coordinate system with the z-axis coinciding with the storage ring axis and the x-axis pointing towards the timing detector to a coordinate system with the new z-axis coinciding with the GW propagation direction, and the xy axes being aligned with the GW polarization axes. Specifically, ϕ, θ and ψ are the rotations around the z, y' and z'' axes, respectively. The origin of both coordinate systems is at the center of the storage ring and both coordinate systems are right-handed.

As it is not possible to know a priori whether GWs are present at any given time, v_0 in Eq. (7.1) cannot be measured in practice. We therefore reformulate Eq. (7.1) in terms of $v(t_0) = v_i$, the instantaneous initial speed of the ions, which *can* be measured. Note that v_i denotes the *instantaneous* speed of the ions, as opposed to the speed averaged over one or more revolutions. We start from Eq. (6) of paper I, and keeping the term $v(t_0)$ as it is, we follow through with the remaining derivation as done in paper I, to get a reformulated expression for the circulation time deviation:

$$\Delta T_{\mathrm{GW}}(T) = \int_{t_0}^{t_0+T} \left[\left(1 - \frac{v_i^2}{2c^2}\right) h_{\theta\phi\psi}(t, \alpha(t)) - \frac{1}{2}\left(1 - \frac{v_i^2}{c^2}\right) h_{\theta\phi\psi}(t_0, \alpha_0) \right] dt. \quad (7.2)$$

Thus, $\Delta T_{\mathrm{GW}}(T)$ is now the timing deviation relative to the expected ion arrival times calculated using v_i instead of v_0.

The first term in Eq. (7.2) is an oscillatory function containing three different frequencies, viz. the GW frequency, Earth's rotational frequency and the revolution frequency of the storage ring ions. The latter frequency is always much greater than the former two in the case of mHz GWs. This allows us to analytically integrate out the rapidly oscillating terms corresponding to the ion revolution frequency. From paper I, we recall

$$\begin{aligned} h_{\theta\phi\psi}(t, \alpha) = h_+(t)\left(f_s^+ \sin^2\alpha + f_c^+ \cos^2\alpha + f_{sc}^+ \sin 2\alpha\right) + \\ h_\times(t)\left(f_s^\times \sin^2\alpha + f_c^\times \cos^2\alpha + f_{sc}^\times \sin 2\alpha\right), \end{aligned} \quad (7.3)$$

where $h_+(t)$ and $h_\times(t)$ are the plus and cross polarization GW strain components, $\alpha(t) = \alpha_0 + \frac{v_0}{R}(t - t_0)$, and R is the radius of the storage ring. The terms $\sin^2\alpha$, $\cos^2\alpha$ and $\sin 2\alpha$ integrate out to yield the constant factors $\frac{1}{2}$, $\frac{1}{2}$ and 0 respectively. The 'f'-terms inside the parentheses are functions of cosines and sines of the angles θ, ϕ, ψ (see paper I, Sec. 2).

We now make the assumption that v_i is large enough such that the second term in Eq. (7.2), which is linear in T, is negligible compared to the amplitude of the

oscillation of the first term, even for integration times of $T \approx$ a few days. Although the best ion energy for a successful GW detection is still under discussion, the above is a reasonable assumption since relativistic ions may indeed be advantageous (Schmirander et al., in preparation).

Therefore, in the end, we obtain the reformulation,

$$\Delta T_{\mathrm{GW}}(T) = -\frac{1}{2}\Big(1 - \frac{v_i^2}{2c^2}\Big) \int_{t_0}^{t_0+T} \big(F_+ h_+ + F_\times h_\times\big) dt, \tag{7.4}$$

where F_+ and $F_\times$ are the plus and cross polarization antenna pattern functions of an SRGO, with $F_+ = \sin^2\theta \cos 2\psi$ and $F_\times = \sin^2\theta \sin 2\psi$.

Note that in our derivation of $\Delta T_{\mathrm{GW}}(T)$, we only considered terms that are linear in h (see paper I, Sec. 2) since all contributions by higher order terms are usually negligible. However, in the specific case of a face-on orientation of the storage ring relative to the GW source (i.e., $\theta = 0$), we see that $\Delta T_{\mathrm{GW}}(T) = 0$. In this specific case, the signal is therefore dominated by higher order h-terms, as discussed above. We will nevertheless continue to disregard these terms even in the face-on case as these much smaller higher order terms could never be detected by an SRGO that is just sensitive enough to detect the first order h term in other orientations.

Note that the integrand in Eq. (7.4) now has the same form as the GW response of the Laser Interferometer Gravitational-wave Observatory (LIGO) [18], but the response signal in our case is a time-integral of this integrand. Also, while the antenna pattern functions of SRGO are very different compared to those of LIGO, interestingly, they happen to be exactly the same as those of a bar detector [188, 189, 105, 190] the longitudinal axis of which is aligned with the axis of the storage ring (see Sec. 4.2.1 of [146]). Further, the SRGO antenna pattern shown in Fig. 2 of paper I (averaged over all polarization angles), which was derived after making several approximations, happens to be exactly valid even for the general case derived here.

For GWs in the mHz regime, the effect of Earth's rotation must be taken into account, as it causes the angles ϕ, θ and ψ to be periodic functions of time with a period equal to a sidereal Earth day:

$$\begin{pmatrix}\cos\psi & -\sin\psi & 0\\ \sin\psi & \cos\psi & 0\\ 0 & 0 & 1\end{pmatrix}\cdot\begin{pmatrix}\cos\theta & 0 & \sin\theta\\ 0 & 1 & 0\\ -\sin\theta & 0 & \cos\theta\end{pmatrix}\cdot\begin{pmatrix}\cos\phi & -\sin\phi & 0\\ \sin\phi & \cos\phi & 0\\ 0 & 0 & 1\end{pmatrix}=$$
$$\begin{pmatrix}\cos\psi_{eq} & -\sin\psi_{eq} & 0\\ \sin\psi_{eq} & \cos\psi_{eq} & 0\\ 0 & 0 & 1\end{pmatrix}\cdot\begin{pmatrix}-\sin\delta_{\rm src} & 0 & \cos\delta_{\rm src}\\ 0 & 1 & 0\\ -\cos\delta_{\rm src} & 0 & -\sin\delta_{\rm src}\end{pmatrix}$$
$$\cdot\begin{pmatrix}-\cos\omega_e\big(\alpha_{\rm src}-l_0-(t-t_0)\big) & \sin\omega_e\big(\alpha_{\rm src}-l_0-(t-t_0)\big) & 0\\ -\sin\omega_e\big(\alpha_{\rm src}-l_0-(t-t_0)\big) & -\cos\omega_e\big(\alpha_{\rm src}-l_0-(t-t_0)\big) & 0\\ 0 & 0 & 1\end{pmatrix}$$
$$\cdot\begin{pmatrix}\sin\theta_{\rm SRGO} & 0 & -\cos\theta_{\rm SRGO}\\ 0 & 1 & 0\\ \cos\theta_{\rm SRGO} & 0 & \sin\theta_{\rm SRGO}\end{pmatrix}\begin{pmatrix}\cos\phi_0 & -\sin\phi_0 & 0\\ \sin\phi_0 & \cos\phi_0 & 0\\ 0 & 0 & 1\end{pmatrix}. \quad (7.5)$$

ω_e is the angular speed of Earth's rotation. $\alpha_{\rm src}$ and $\delta_{\rm src}$ are the right ascension (in units of time) and declination of the GW source. ϕ_0 is the angle between the line joining the center of the storage ring to the timing detector, and the meridian passing through the center of the storage ring, measured using the right-hand curl rule starting from the detector position. l_0 and $\theta_{\rm SRGO}$ are, respectively, the local sidereal time at the start of the observations, t_0, and the latitude of the center of the storage ring.

Note that, without loss of generality, if we assume that the timing detector lies due North, then the SRGO coordinate system can be regarded similar to the horizon celestial coordinate system, with the difference being that $\phi = 360° - \text{azimuth}$ and $\theta = 90° + \text{altitude}$. This is firstly due to the fact that the handedness of the horizon system is opposite to the right handed convention used in our work. Secondly, the coordinates in the horizon system are used to point towards the source, whereas in our case, we wish to point away from the source, along the GW propagation direction.

Furthermore, the polarization angle in a coordinate system is defined as the angle between a reference line made by projecting the z-axis onto the GW wavefront plane, and a chosen GW polarization axis, following a right-handed rotation convention. In the equatorial celestial coordinate system, the z-axis points towards the north celestial pole. In the SRGO coordinate system, the z-axis points perpendicular to the plane of the storage ring. Therefore, ψ and $\psi_{\rm eq}$ may be the same in cases where SRGO is located at one of Earth's poles.

7.5 Models and numerical procedures

We obtain all the numerical results in this work from a computer code written in Python and freely available online on GitHub [191]. Below, we detail the mathematical models and numerical procedures programmed into the code to obtain our

results:

7.5.1 GW source model

We consider the simplest realistic models for mHz GWs from astrophysical sources viz. the dominant harmonic of GWs from the quasi-circular inspiral phase of non-spinning compact object binaries [192], accounting for the redshift correction to the GW frequency and chirp mass.

The inspiral phase of a non-spinning binary system can be modeled using post-Newtonian analysis [45], which provides relatively simple analytical expressions for the time-varying GW strain amplitudes corresponding to the plus and cross polarizations. The simplest of these corresponds to the quadrupole formula:

$$h_+ = \frac{4}{d_L}\left(\frac{G\mathcal{M}}{c^2}\right)^{\frac{5}{3}}\left(\frac{\pi f}{c}\right)^{\frac{2}{3}}\frac{1+\cos^2(i)}{2}\cos(2\pi f t+\delta_0), \tag{7.6}$$

$$h_\times = \frac{4}{d_L}\left(\frac{G\mathcal{M}}{c^2}\right)^{\frac{5}{3}}\left(\frac{\pi f}{c}\right)^{\frac{2}{3}}\cos(i)\sin(2\pi f t+\delta_0). \tag{7.7}$$

If m_1 and m_2 are the masses of the objects in the binary, then $\mathcal{M} = \frac{(1+z)(m_1m_2)^{\frac{3}{5}}}{(m_1+m_2)^{\frac{1}{5}}}$ is the redshift-corrected chirp mass. d_L is the luminosity distance of the GW source and z is its redshift. i is the inclination angle between the observer's line of sight to the GW source and the angular momentum vector of the GW source. δ_0 is the initial phase of the GW at the start of the observing time, t_0. The redshift-corrected, time-varying GW frequency is $f = (1+z)^{-1}\left(f_0^{-\frac{8}{3}} - \frac{8}{3}k(t-t_0)\right)^{-\frac{3}{8}} = (1+z)^{-1}\sqrt{G(m_1+m_2)}/\pi r^{\frac{3}{2}}$, where r is the separation between the objects in the binary; f_0 is the GW frequency at $t = t_0$, corresponding to an initial separation of $r = r_0$; and $k = \frac{96}{5}\pi^{\frac{8}{3}}\left(G\mathcal{M}/c^3\right)^{\frac{5}{3}}$. G and c are respectively, the gravitational constant and the speed of light. For a higher computational speed, we use an approximate analytical relation between d_L and z for ΛCDM cosmology, from [193].

We use an approximation of the innermost stable circular orbit, $r_{isco} = \frac{6G\max(m_1,m_2)}{c^2}$, to mark the end of the inspiral phase. Upon reaching this point, or at the end of our chosen observation time (whichever comes earlier), our computations are halted.

7.5.2 Storage ring model

We consider a hypothetical circular storage ring having a 100 m circumference and containing a single, rigid, ultrarelativistic particle (not necessarily ionic or subatomic) that is coasting stably at close to the speed of light (making the prefactor in Eq. (7.4) equal to $-1/4$), with no RF system and a single timing detector present within the

ring. The timing detector is placed to the south of the storage ring's center, such that it lies on the longitude that passes through the center of the storage ring i.e. $\phi_0 = 0$.

We assume that this high-tech storage ring has a sufficiently high vacuum to allow the particle to circulate for the entire duration of the observation run without loss due to collisions with air molecules. We also assume that the particle has a charge-to-mass ratio which minimises the noise due to synchrotron radiation, such that it can circulate stably during the observation run without the RF system. We cannot comment at this time, whether an existing storage ring could be turned into such a system, or whether this could be realised in the future, but we remain hopeful that it can.

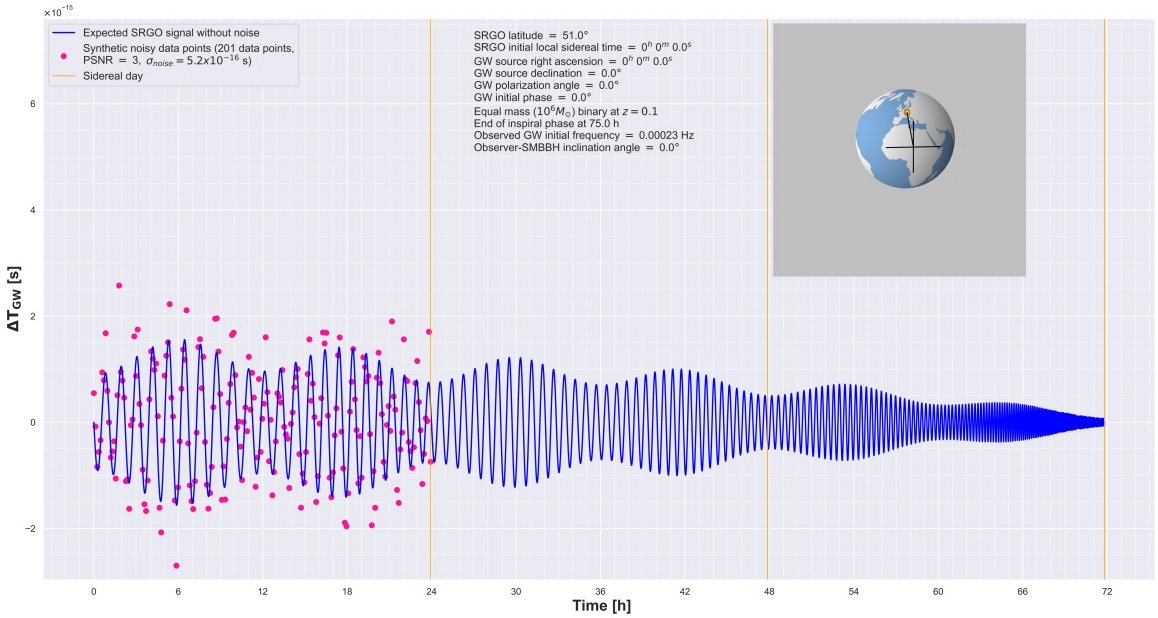

Figure 7.1: The blue curve is the expected response of an SRGO to mHz GWs, for the given parameters. The pink dots are a demonstration of discrete, noisy data points, created by adding artificial Gaussian noise to the SRGO response signal. The orange ring is the initial SRGO position, while the black lines show the GW propagation direction and plus polarization axes.

As per the Nyquist-Shannon sampling theorem, the minimum sampling (data measurement) rate must be greater than twice the highest expected GW frequency, while the maximum possible sampling rate would correspond to the timing detector making one detection per revolution of the ion bunch, i.e. every time it arrives at the detector. Given the parameter choices made earlier, our SRGO would have a maximum sampling rate of $f_{\text{sample}} = 2.998$ MHz. While in reality, one would prefer having a sampling rate as close to the maximum possible rate as allowed by instrument limitations, but in our simulations, we choose significantly lower values of the sampling rate for the sake of computational speed. This also provides upper limits on the constraints that can be derived from parameter estimation. However, each data point at a given noise level may always be considered equivalent to a binning of several close-by data points at a higher noise level. In our code, we choose the total number of data points to be powers of two, as this allows for faster computation of

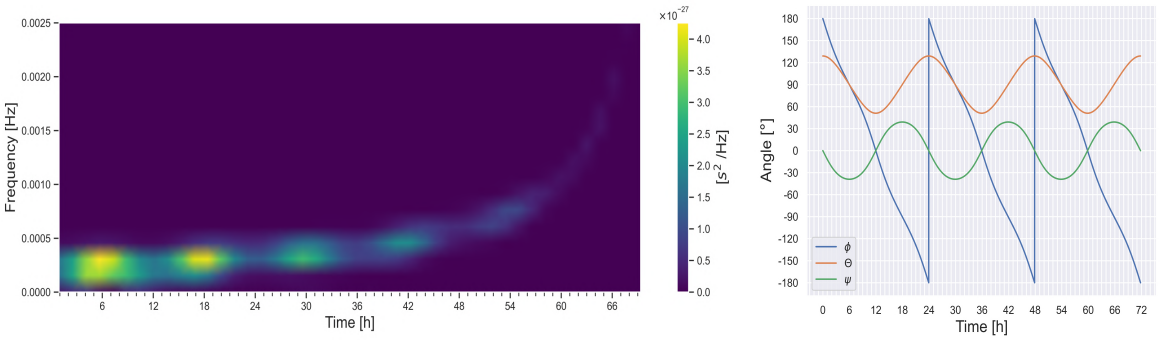

Figure 7.2: The left panel shows the spectrogram of the SRGO response, which is the time-evolution (along the horizontal axis) of the power spectral density of the signal (along the vertical axis) computed over a sliding time window. The right panel shows the time evolution of the Euler angles, ϕ, θ, ψ. Both panels correspond to the SRGO response signal shown in Fig. 7.1, without any noise.

the Fast Fourier Transform (FFT) done during the MCMC GW parameter estimation.

We assume that deterministic (including systematic) sources of noise, such as gravity gradient noise, seismic activity, etc. are either technologically eliminated or accounted for by subtracting them from the data, and only stochastic (random) noise sources remain in the experiment as the residual noise. The net residual noise is assumed to be Gaussian (an assumption also made by LIGO [194]), with a standard deviation, $\sigma_{\rm noise}$, between 10 to 0.01 times the peak GW signal. We consider this range of PSNR (peak signal-to-noise ratio) as values beyond this range may give trivial results, particularly for parameter estimation. A better noise model for the current study cannot be assumed until detailed studies of noise sources have been done (Schmirander et al., in preparation).

7.5.3 Numerical solution for finding $\phi(t), \theta(t), \psi(t)$

Upon analytically multiplying all the matrices on the left hand side of Eq. (7.5), and naming the net matrix product on the right hand side as R, we arrive at the following relations by comparing the matrix elements on both sides:

$$\begin{aligned} \phi(t) &= \arctan\left(\frac{R_{21}}{-R_{20}}\right), \\ \theta(t) &= \arccos\left(R_{22}\right), \\ \psi(t) &= \arctan\left(\frac{R_{12}}{-R_{02}}\right). \end{aligned} \tag{7.8}$$

Note that in the above relations, numerically, we must use the appropriate functions to obtain the angles in their correct quadrants. The right panel of Fig. 7.2 shows the time evolution of the angles for the case corresponding to Fig. 7.1.

7.5.4 Numerical integration procedure

We use Boole's rule quadrature [195] over a timestep to compute its contribution to the integral of Eq. (7.4). Starting from the initial value of the integral (equal to zero), the contribution of each timestep is added to the integral, and its cumulative value is saved after each timestep. We perform this procedure till the halting condition (mentioned in Sec. 7.5.1) is reached. Thus, we numerically obtain the SRGO response signal as a time series.

7.5.5 Markov Chain Monte Carlo (MCMC) fitting procedure

MCMC is a Bayesian inference tool for numerically obtaining the joint posterior probability distribution of unknown model parameters by directly drawing samples from the posterior. MCMC works by following an algorithm to find and explore around the regions in parameter space that correspond to the maximum likelihood of the parameters being a fit for the given data, given model and a prior probability distribution of the unknown fitting parameters [196, 197, 198].

MCMC methods are preferred over the conventional matched filtering algorithm [146] for thorough and efficient GW parameter estimation, because the typical GW models contain around 15 to 17 fitting parameters, and making a grid in parameter space of such a high dimensionality would require an impossibly long computation time. In our study, we do GW parameter estimation using MCMC methods, keeping all possible unknown parameters as the fitting parameters. These are nine in number, namely, the GW source masses m_1, m_2 ; the initial separation between the masses, r_0 ; the GW source inclination angle, i ; the GW source redshift, z ; the initial phase of the GW, δ_0 ; the right ascension, α_{src} and declination, δ_{src} of the GW source ; and the polarization angle, ψ_{eq} of the GW in the reference frame of equatorial celestial coordinates.

In our code, we first create synthetic noisy data points by adding Gaussian noise to the SRGO response computed for user-provided parameters. The noisy data is then transformed to Fourier space via a Fast Fourier Transform (FFT) and passed to the likelihood function.

We use flat priors for the unknown fitting parameters and a two-dimensional Gaussian noise "Whittle" likelihood function, as also done by LIGO for GW parameter estimation [194]. The priors corresponding to angular parameters are bounded between $-180°$ and $180°$, whereas priors corresponding to non-angular parameters are bounded between zero and double of their true parameter values for computational efficiency.

We employ the Differential Evolution Markov Chain (DE-MC) algorithm [199] for the MCMC chains, and run per data set, 1000 parallel chains which draw 1250 samples each. Since we are purely interested in parameter estimation, and not in showing the convergence of chains to the region of maximum likelihood, we do not

discard 25% of the initial traces as the “burn-in" phase. Instead, we allow the chains to start from the true parameter values and then explore around. For each case (i.e. a set of user-provided parameters), 10 data sets are produced by regenerating the noisy data points, and after the MCMC procedure, we discard those results where the true parameter values do not lie within the $3-$sigma (99.7%) highest posterior density (HPD) region. The multiple joint posteriors per case give us the statistical variation of the joint posterior for each case. This is used to produce error bars on the sizes of the joint posteriors plotted as a function of different controllable experiment parameters, discussed in Sec. 7.7. In all cases, MCMC is carried out in our code using the PyMC3 Python module [200].

7.6 Results: SRGO response analysis

7.6.1 Response signal analysis

In Fig. 7.1, we show a demonstration of the response of an SRGO to mHz GWs from an SMBBH (supermassive binary black hole) inspiral, for an arbitrarily chosen configuration of parameters. In general, we notice that when the GW period is smaller than Earth's rotation period, then the response signal has an envelope which periodically repeats every sidereal day due to the effect of Earth's rotation. Within the envelope, the signal has a frequency equal to the GW frequency, which increases with time due to the inspiral of the binary. Correlated to this is also the observation that the amplitude of the signal diminishes with passing time and increasing GW frequency. The behaviour of the peak signal amplitude as a function of the GW frequency, f, and total observation time, T_{obs} is discussed in depth in the following paragraphs, supplemented by Fig. 7.3. Therefore, unlike LIGO, the chirping of the GW strain amplitude does not reflect in SRGO's response spectrogram (Fig. 7.2 left panel), whose amplitude actually diminishes with time, as the SMBBH inspirals and the GW frequency increases. The right panel of Fig. 7.2 shows the evolution of the Euler angles which point along the GW propagation direction in the SRGO reference frame. These angles determine the track made by the GW source on the SRGO antenna pattern due to Earth's rotation. Due to the convention used in our theoretical framework, these angles point opposite to the GW source. The expected orders of magnitude of the SRGO response signal amplitude (due to astrophysical sources) are discussed in Sec. 7.6.3. The variation of the response signal with some important parameters (which give useful insights) are shown in the following figures.

In Fig. 7.3, we notice first that, in the regime where $f\,T_{\rm obs} \gg 1$, the PSNR decreases with increasing GW frequency. Thus, the right side tails in the plots agree with our analytical results from paper I. At very low GW frequencies, where $f\,T_{\rm obs} \ll 1$, the timing deviation buildup is slow, and the GW strain amplitude is also quite small. Therefore, the plots have tails on the left side as well. Finally, in the regime where $f\,T_{\rm obs} \sim 1$, the PSNR decreases with decreasing observation time. This is because, when the observation time is large and also close to the GW period, a large timing

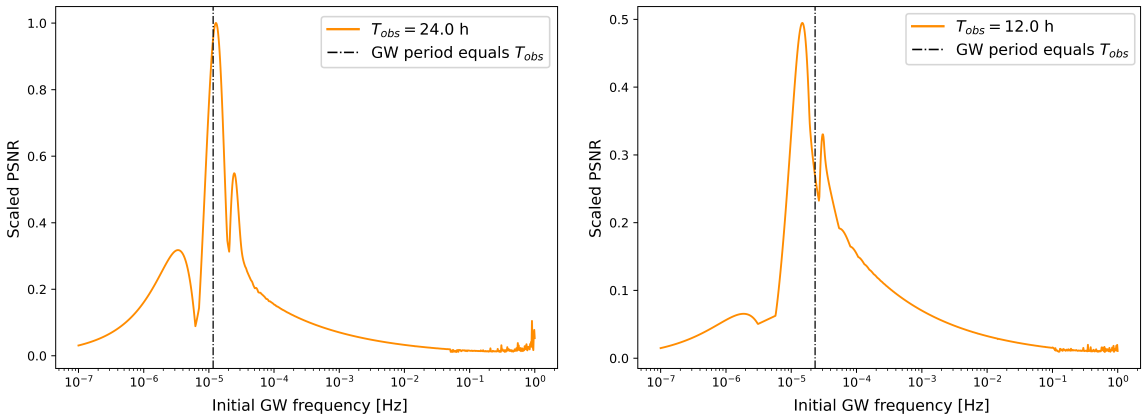

(a) $T_{\text{obs}} = 24$ hrs

(b) $T_{\text{obs}} = 12$ hrs

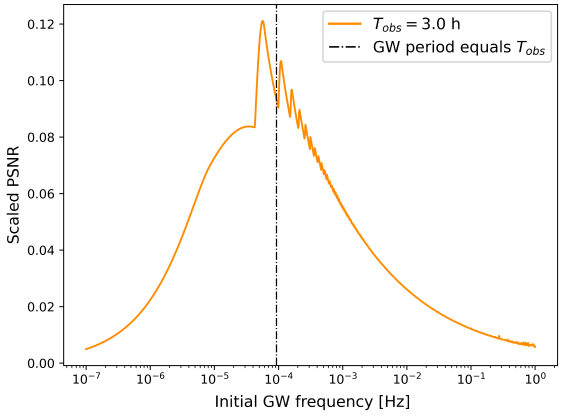

(c) $T_{\text{obs}} = 3$ hrs

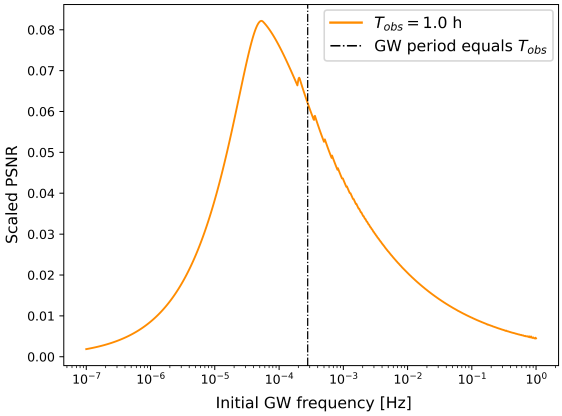

(d) $T_{\text{obs}} = 1$ hour

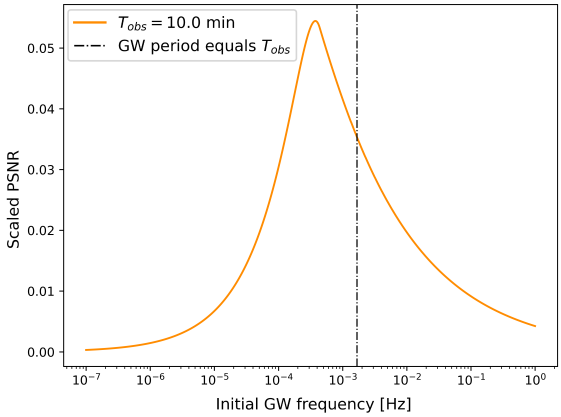

(e) $T_{\text{obs}} = 10$ mins

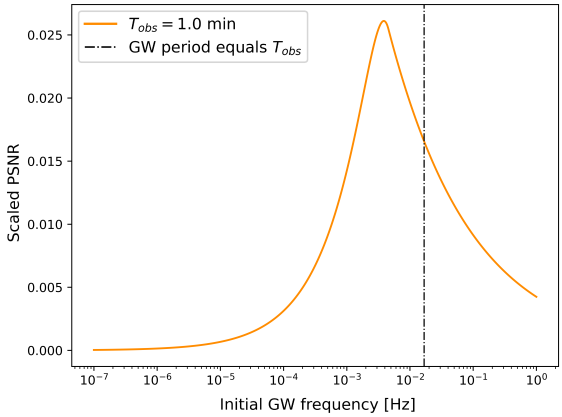

(f) $T_{\text{obs}} = 1$ min

Figure 7.3: Scaled values of the peak signal-to-noise ratio as a function of the initial GW frequency (which is set by the initial separation of the binary), for different values of the observation time, T_{obs}. All other parameters are equal to those shown in Fig. 7.1, except the black hole masses, which have been chosen to be 3 $M_\odot$ each, so that even for the highest initial GW frequency, the inspiral phase does not end before the total observation time. Note that, due to the scaling, the shape of the plots are independent of the binary mass. The scaling is done such that the largest peak among all plots has a value of unity.

deviation can be accumulated by the circulating ions, as opposed to cases with smaller observation times.

We can understand this behaviour better by conducting a mathematical analysis of Eq. 7.4. For better clarity, let us temporarily ignore the contribution due to the envelope, contained in the antenna pattern terms F_+ and $F_\times$ (which corresponds to the situation in plot 7.3f, since the observation time is much smaller than the Earth's rotation period). The response signal is basically a time integral of a periodic function that is the GW strain, and the numerical value of this integral is maximised when integrating over some fraction of the GW period (depending on the initial phase) i.e. in the regime $f\,T_{\rm obs} \sim 1$. In this regime, if the GW period (or equivalently, the total observation time), is reduced, and even if the amplitude of the GW strain were to increase, the total area under the strain curve would actually decrease. The same reason also explains why, in the regime $f\,T_{\rm obs} \gg 1$, the peak signal decreases with increasing GW frequency. Note that in this regime, the peak signal amplitude would occur somewhere within the first GW period, ignoring the effect of the envelope.

The dynamically changing peaks and valleys in the series of plots can be somewhat elucidated: they are the result of the interplay between the GW period, initial GW phase, the orientation of SRGO relative to the GW source, Earth's rotation period and the observation period. The orientation of SRGO relative to the GW source and Earth's rotation period together determine the envelope seen in the response signal of Fig. 7.1. During the observation time, large peaks in these plots occur when peaks in the GW strain waveform align with the envelope peaks, and valleys occur when the GW strain peaks align with the envelope valleys (or vice versa, whichever produces a greater response signal). For a given observation time, as the initial GW frequency is increased, a number of successive GW strain peaks and valleys occur during the observation period, which may or may not align with the envelope peaks and valleys. An aligned GW strain peak (resulting in a local maxima in the plot curves), upon increasing the initial GW frequency, will become misaligned, resulting in a drop in the curve until the next peak starts becoming aligned, causing then a rise in the curve. This succeeding local maxima may be higher or lower than its predecessor, depending on the location of the global maxima, which occurs when the initial GW period is close to the observation time. This explains the spiky sections of the plot curves, prominently seen in Fig. 7.3c, but also present in the other plots.

In Figs. 7.3a, 7.3b and 7.3c, the noisy regions in the right side tails of the plots have purely numerical origins, being caused by the abrupt halting of the code one timestep after the inspiral phase has been crossed. Therefore, they exist only at the ends of the right side tails (corresponding to high initial GW frequencies, meaning that the binary compact objects begin close to the end of their inspiral phases). As the observation time is reduced, the end of the inspiral phase would be reached within the observation time at higher initial frequencies. Therefore, the noisy regions shift towards higher frequencies and eventually disappear in Figs. 7.3d, 7.3e and 7.3f.

In Fig. 7.4, we plot the PSNR as a function of the source position in the sky, scaled such that the arbitrary case corresponding to Fig. 7.1 has a PSNR of unity. While

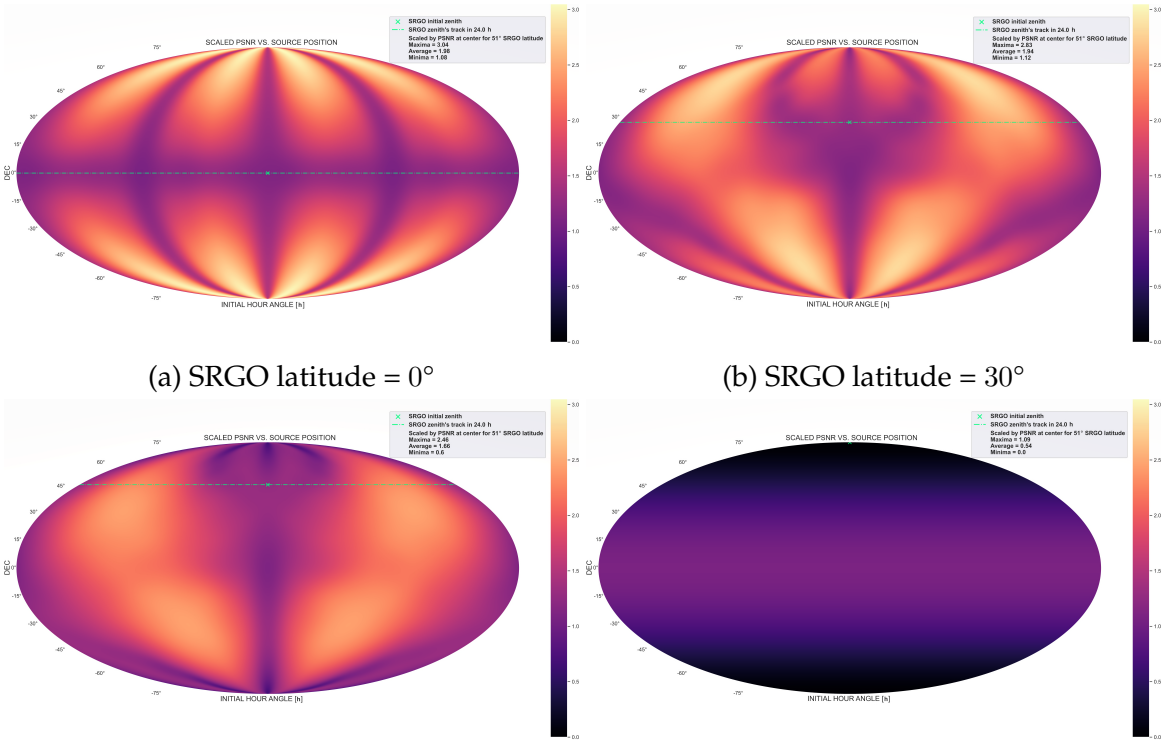

(a) SRGO latitude = 0°

(b) SRGO latitude = 30°

(c) SRGO latitude = 51°

(d) SRGO latitude = 90°

Figure 7.4: Scaled values of the peak signal-to-noise ratio as a function of the GW source's initial position in the sky relative to SRGO. All other parameters are equal to those shown in Fig. 7.1, except the initial separation between the masses which is 1 AU (corresponding to an initial GW period of 3.1 h), and the observation time which is 1 day. The top-left, top-right, bottom-left and bottom-right figures respectively correspond to an SRGO latitude of 0°, 30°, 51° and 90°. The scaling is done relative to the case corresponding to the center of the bottom-left plot.

changing the source position, all other parameters remain the same as those in Fig. 7.1, but the initial SMBBH separation is 1 AU (corresponding to an initial GW period of 3.1 h), and signal is computed over an observation time of 1 day. We repeat this for different latitudes of the SRGO location on Earth.

We observe that the complex patterns in the plots are a modified projection of the SRGO antenna pattern on the sky, as expected from Eq. 7.4. Other parameters being fixed, for a given SRGO latitude and source declination, the horizontal variation is determined by the initial hour angle, the GW frequency, initial GW phase, GW polarization angle and Earth's rotation frequency. Maxima in the horizontal variation occur during the observation time when peaks in the GW strain waveform occur exactly at a time when there are peaks in the response signal envelope. Minima occur when the GW strain peaks align with the envelope valleys (or vice versa, whichever produces a greater response signal). We note that the pattern depends on the initial hour angle i.e. the right ascension of the GW source relative to the initial SRGO local sidereal time (and not on their absolute values). However, the same is not true between the SRGO latitude and source declination. That symmetry is broken by the Earth's spin axis, and therefore, the SRGO latitude variation produces different patterns in the plots. The bottom-right plot corresponds to SRGO being placed at the pole. For this case, if the GW source is also at one of the poles, then the orientation always remains face-on, and no response signal is produced. For all other cases, a non-zero response signal is produced over 24 hours, due to a changing orientation of the GW source relative to the ring.

Further, we observe that the plots show antipodal symmetry, since placing the ring and/or the GW source at antipodal positions, and/or having the ions circulating in the opposite direction, would all produce the same SRGO response. The plots also appear to have a left-right symmetry, because two GW sources at the same declination, initially located on either side of the ring and having the same hour angle magnitude, would produce the same value of the initial SRGO response. The response signals over a 24 h period would, however, not be exactly the same, breaking the symmetry. Although both sources would trace the same path across the antenna pattern, the phase difference between the GW and the path across the antenna pattern would be different, so that the peak signal would be attained at different times and at slightly different values. In addition, the symmetry is further broken by the time evolution of the GW frequency due to the inspiral, which in turn changes the amplitude of the response signal, as discussed above. This effect is particularly relevant when the rate of change of the GW frequency is large, which is not the case in the example shown in Fig. 7.4. Finally, there is also a latitudinal symmetry, as having SRGO located at equal and opposite latitudes would simply flip the plots about the horizontal axis.

The SRGO latitude variation indicates that placing the ring near the equatorial latitudes on Earth would be more advantageous than placing the ring near the polar latitudes, offering an increase of the maximum PSNR by around 3 times, of the average PSNR by around 4 times, and of the minimum PSNR by a factor of unity from zero, between the polar and equatorial SRGO latitudes.

7.6.2 SRGO sensitivity curve

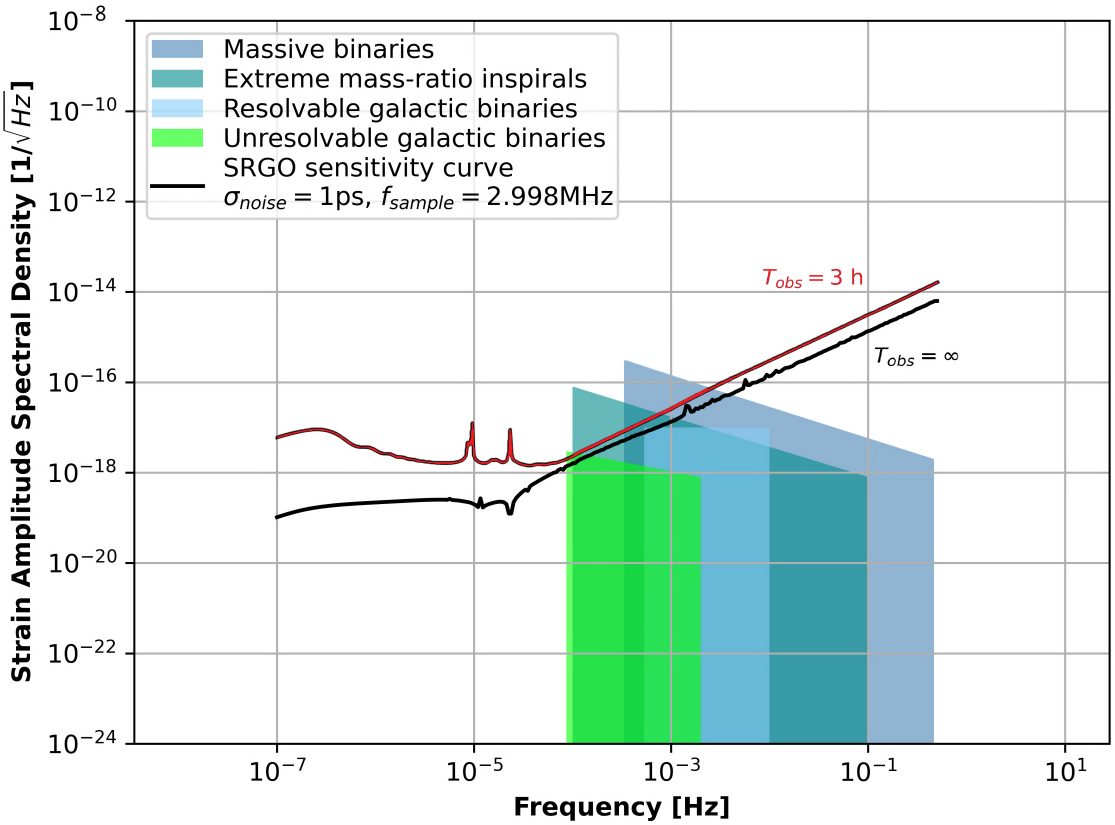

Figure 7.5: The numerically computed sensitivity curve of an SRGO for the given parameter values, and averaged over all other parameter values. The red curve corresponds to a finite observation time of 3 h, while the black curve is the standard amplitude spectral density corresponding to an infinite observation time.

The sensitivity curve of a GW detector may be defined as the curve in the plane of the strain amplitude spectral density versus frequency, where the signal-to-noise ratio is unity.

Conventionally, a GW sensitivity curve plot contains two elements: First, colored regions are shown corresponding to various astrophysical GW sources. These regions are computed solely from GW strain models of the sources, and their extent is determined by astronomical constraints applied to the model parameters. Second, a curve is overplotted over these regions, which is constructed by modeling the experimentally measured detector noise data as a strain, using the response model of the GW detector. Since this plot is in the frequency space, which is integrated over all time, the ratio of a point in the colored region to a point on the curve, at a given frequency, directly gives the integrated signal-to-noise ratio at that frequency. This allows us to directly read off the signal-to-noise ratio by eye from such a plot. However, for computing the sensitivity curve, an averaging over the antenna pattern of the GW detector is involved. For LIGO and other high frequency GW detectors, the averaging of the antenna pattern is time-independent and trivial, because the antenna

pattern is practically stationary over the duration of the GW. For millihertz GWs, which is our region of interest for an SRGO, the antenna pattern is not stationary due to Earth's rotation, making such an averaging time-dependent and difficult.

Therefore, in our study, we plot the sensitivity curve in a different way. The colored regions in our plot are the same as in every conventional GW sensitivity plot, and taken from [99]. But the curve itself is not made by modeling the experimentally measured (or artificially generated) noise data as a strain. Instead, we compute the source GW strain that would be required to make a detection using SRGO, for chosen values of controllable experiment parameters such as the stochastic noise level, data sampling rate and total observation time. Hence, our sensitivity plot compares the expected GW strain (the colored regions) to the GW strain required to make a detection (the curve itself), as a function of GW frequency. Note that here too, the integrated signal-to-noise ratio can be read by eye from the plot, based on the definition of the sensitivity curve mentioned earlier.

In this study, we use our code to numerically compute the SRGO sensitivity curve. We start by equating the root mean square value of the response signal (taken over the total observation period) to the effective noise,

$$[\Delta T_{\mathrm{GW}}]_{\mathrm{rms}} = \frac{\sigma_{\mathrm{noise}}}{\sqrt{f_{\mathrm{sample}} T_{\mathrm{obs}}}}, \tag{7.9}$$

where T_{obs} is the total observation time and $f_{\mathrm{sample}} = \frac{n_p v_0}{2\pi R}$ is the data sampling rate, with n_p being the number of circulating test masses that are timed, which may be individual ions or bunches of ions. σ_{noise} can be the standard deviation of any stochastic noise, even the net stochastic noise in the system. In our study, we assume that the residual noise in the system is Gaussian, as mentioned in Sec. 7.5.2. Note that, although the condition Eq. (7.9) appears unconventional, but upon transposing $\sqrt{f_{\mathrm{sample}} T_{\mathrm{obs}}}$ over to the left, it is clear that this is a valid way of imposing the fundamental criterion for GW signal detectability, where some measure of the **integrated** signal, such as the root mean square of the signal multiplied by the square root of the observation time, should be equal to a measure of the noise level, such as σ_{noise}.

We then expand the left hand side using Eq. (7.4), substituting h_+ and $h_\times$ from Eq. (7.6) and Eq. (7.7), respectively. Then we set $k = 0$ in the GW frequency evolution to get continuous GWs (i.e. GWs with a constant frequency). Finally, we club together all the common time-independent terms within the integral, and call this quantity h_0. Hence, we have defined,

$$h_0 = \frac{4}{d_L} \left(\frac{G\mathcal{M}}{c^2} \right)^{\frac{5}{3}} \left(\frac{\pi f}{c} \right)^{\frac{2}{3}}. \tag{7.10}$$

Rearranging Eq. (7.9), we thus obtain,

$$h_0 = \frac{4\sigma_{\text{noise}}}{\sqrt{f_{\text{sample}} T_{\text{obs}}}}. \left[\int_{t_0}^{t_0+T} \left(F_+. \frac{1+\cos^2(i)}{2} \cos(2\pi f t + \delta_0) + F_\times . \cos(i) \sin(2\pi f t + \delta_0)\right) dt\right]_{\text{rms}}^{-1}. \quad (7.11)$$

Hence, the quantity h_0 must satisfy the condition Eq. (7.11) on the sensitivity curve. Now, we calculate and express the GW strain amplitude spectral density (ASD) in terms of h_0. It is defined as,

$$ASD = \lim_{T_{\text{obs}} \to \infty} \frac{|\tilde{h}(f)|}{\sqrt{T_{\text{obs}}}}, \quad (7.12)$$

where the Fourier Transform of the GW strain, $\tilde{h}(f)$, can be calculated in terms of h_0 over the finite duration T_{obs}, by first rewriting Eq. (7.6) as,

$$h_+(t) = h_0 \frac{1+\cos^2(i)}{2} \cos(2\pi f t + \delta_0). \quad (7.13)$$

Upon performing the calculations, we find,

$$ASD = \lim_{T_{\text{obs}} \to \infty} \frac{h_0}{2} \frac{1+\cos^2(i)}{2} \sqrt{T_{\text{obs}}} \sqrt{1 + \text{sinc}^2(2\pi f T_{\text{obs}}) + 2\,\text{sinc}(2\pi f T_{\text{obs}}). \cos(2\delta_0)}. \quad (7.14)$$

Finally, we substitute h_0 from Eq. (7.11) and then apply the limit in Eq. (7.14) to get,

$$ASD_\infty = \frac{2\sigma_{\text{noise}}}{\sqrt{f_{\text{sample}}}} \frac{1+\cos^2(i)}{2} \left[\int_{t_0}^{t_0+T} \left(F_+. \frac{1+\cos^2(i)}{2} \cos(2\pi f t + \delta_0) + F_\times . \cos(i) \sin(2\pi f t + \delta_0)\right) dt\right]_{\text{rms}}^{-1}. \quad (7.15)$$

Note that the root mean square in Eq. (7.15) is over an infinite duration. But due to the periodicity of the GW signal, we can compute the root mean square over the lowest common multiple of the GW period and Earth's rotation period. For a finite observation time, we can skip the limit in Eq. (7.14) to get,

$$ASD_{<\infty} = \frac{2\sigma_{\text{noise}}}{\sqrt{f_{\text{sample}}}} \frac{1+\cos^2(i)}{2} \left[\int_{t_0}^{t_0+T} \left(F_+ . \frac{1+\cos^2(i)}{2} \cos(2\pi f t + \delta_0) + F_\times . \cos(i) \sin(2\pi f t + \delta_0)\right) dt\right]^{-1}_{\text{rms}} \sqrt{1+\text{sinc}^2(2\pi f T_{\text{obs}}) + 2\,\text{sinc}(2\pi f T_{\text{obs}}).\cos(2\delta_0)}. \quad (7.16)$$

The GW strain amplitude spectral density is plotted as a function of the GW frequency, f, and it is numerically averaged over all the GW source parameters present in Eq. (7.16). Note that, we would have obtained similar analytical results had we used $h_\times$ instead of h_+ in the above derivation, which would have lead to the same numerical result after averaging over the GW source parameters. The result shown in Fig. 7.5 numerically confirms that an SRGO would be sensitive to mHz GWs by design. In the log scale, the SRGO sensitivity curve has a linear behaviour in the mHz frequency regime, as analytically predicted in paper I [1]. The sensitivity deteriorates at higher frequencies. This is because, as the GW period becomes smaller, the SRGO response amplitude also decreases, since the ions spend lesser time accumulating a timing deviation during every half-cycle of the GW. This aspect is discussed in the previous section and shown in Fig. 7.3. Therefore, a larger strain amplitude would be required to detect high frequency GWs. This would greatly exceed the predicted strain amplitudes from astrophysical sources in the decihertz or kilohertz ranges (i.e. for "LIGO-like" sources).

At very low frequencies, for a finite observation time (red curve in Fig. 7.5), the sensitivity curve rises. We may perform a thought experiment to analyse this situation: a zero frequency GW would be equivalent to an anisotropic spacetime having a constant distortion, and not necessarily a flat spacetime. In such a spacetime, if the instantaneous initial speed of the circulating test mass is measured and used to predict the expected future arrival times of the test mass at the timing detector, then in general the observed arrival times would deviate from the prediction, as the test mass traverses an anisotropic spacetime. This is why, if we input $f = 0$ in Eq. (7.4), we still get a finite value of the response signal. Therefore, unlike laser

[1]The 'LHC-GW' sensitivity curve shown in Fig. 1 of paper I was not a conventional one, since it was not normalized for a fixed observation time. It could not be directly compared with the sensitivity curves of other GW detectors, and was therefore shown in a separate plot. In this study, since we plot the strain amplitude spectral density, this issue is resolved.

interferometers and atom interferometers (which use test masses that can only move linearly) which require both the temporal and spatial components of GW spacetime in order to probe it, an SRGO (which utilizes circulating test masses) would, in principle, be able to probe purely the spatial anisotropy of GW spacetime even at very low GW frequencies and finite observation times. However, for low frequency GWs, as the GW period far exceeds the total observation time, $T_{\rm obs}$, the peak response signal value would be comparatively small, as discussed in the previous section and shown in Fig. 7.3. That is why the SRGO sensitivity curve rises again at low frequencies. Also, for most resolvable astrophysical GW sources, the strain amplitude at near-zero frequencies would be near-zero. Further, we notice oscillations in the red curve at low frequencies. These correspond to the term containing sinc functions in Eq. 7.16 which appears as a result of Fourier transforming the GW strain over a finite observation time.

However, for an infinite observation time (black curve in Fig. 7.5), in principle, no matter how small the GW frequency, one can observe several GW wavelengths. Since this regime corresponds to $f\,T_{obs} \gg 1$ as shown in Fig. 7.3, the signal would increase with decreasing frequency. This causes the black curve in Fig. 7.5 to continue to decline at low frequencies, unlike the red curve.

In both curves of Fig. 7.5, we notice two significant spikes at GW frequencies corresponding roughly to a period of a full day and a half day. This suggests that when the GW period is equal to a full or half of Earth's rotation period, for certain parameter configurations, the signal amplitude is greatly boosted or reduced relative to the average. Therefore, while averaging over parameters to compute the sensitivity curve, such special configurations act as outliers and produce a spike in the average curve at certain frequencies. Moreover, in the black curve, which corresponds to an infinite observation time, we note that the curve changes its slope at around the region where the GW period equals half a day and one day, although the curve still continues to fall gradually with decreasing frequency. This is because, at this point, unlike before, the GW frequency determines the signal envelope instead of Earth's rotation frequency, thus changing the properties of the signal.

The red sensitivity curve of Fig. 7.5 should corroborate with the curve in Fig. 7.3c, as both are computed for an observation time of 3 hours and we expect them to be inversely related. Although the general shape of the two curves agree with each other, their details are different, since the sensitivity curve has been computed by averaging over several parameters, whereas Fig. 7.3c corresponds to a fixed set of parameters. The GW frequency of the sensitivity curve minima matches the GW frequency of the maxima in Fig. 7.3c. In general, combining the insights from Figs. 7.3 and 7.5, we deduce that the minima of the sensitivity curve would occur at a GW frequency close to the inverse of the observation time, and that this minimum would be smaller for longer observation times. Based on the predicted astrophysical mHz GW sources, we can conclude that the minimum observation time for an SRGO experiment to be maximally sensitive to the entire mHz GW regime, would be of a few hours. This can be seen in Fig. 7.5, where the minima of the sensitivity curve lies close to the low-frequency edge of the predicted mHz GW regime.

Finally, we note from Eq. 7.15 and Eq. 7.16 that the absolute scale of sensitivity curves in Fig. 7.5 of course scales with $\sigma_{\rm noise}/\sqrt{f_{\rm sample}}$. This holds because we consider only stochastic noise to be present in the system, and any stochastic noise can be cut down by collecting more data points, due to the fundamental theorem in statistics that the variance of the mean goes as the inverse of the number of data points.

7.6.3 SRGO observational range

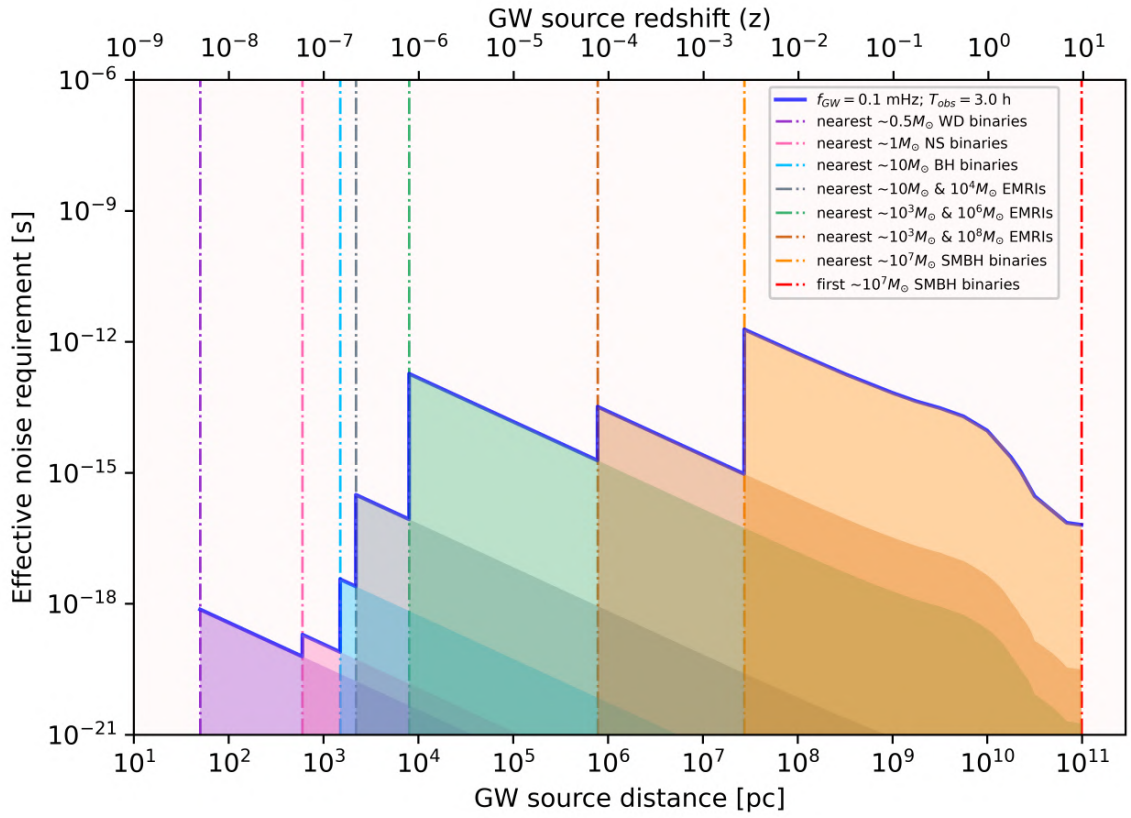

Figure 7.6: The maximum effective noise allowed in an SRGO to make a detection, or equivalently, the largest SRGO response amplitude expected in the best-case (optimum parameter choice) scenarios which maximise the signal, due to GW sources at various distances. The colored dash-dotted lines indicate the nearest location of a particular type of source i.e. these GW sources are absent to the left of the colored line corresponding to them. All computations are done for a fixed observation time of 3 hours, and an initial GW frequency which is at the expected lower limit of the mHz regime, as this would maximise the SRGO response amplitude.

In the previous sections, having simulated the response signal of an SRGO to astrophysical GWs and having computed the sensitivity curve, here we predict using our models, the required effective residual noise in the system to make a detection of various different types of GW sources. By 'effective', we mean the residual stochastic noise divided by the square root of the number of data points taken over the observation period. We do this by computing the root mean square

value of the strongest signal expected in an SRGO, using the principle of Eq. (7.9), discussed in the previous subsection. We use a realistic distribution of GW source types in the universe, combined with choosing a set of parameters for a given source that maximises the SRGO response.

From the ninth catalogue of spectroscopic binary orbits (SB9) [201], cross-referenced with the Gaia Data Release 3 [202, 203, 204], we find that the nearest spectroscopic binaries within our galaxy, including white dwarf (WD) binaries with masses $\sim 0.5 M_\odot$ and periods of a few days, are located at distances of a few tens of pc. Whereas, the nearest spectroscopic binaries with periods of a few hours are located at distances of several tens of pc. Hence, we choose a distance of 50 pc to mark the nearest WD binaries that would emit mHz GWs.

The nearest neutron star (NS) binaries [205, 206, 207, 208, 209] with masses $\sim 1 M_\odot$ and periods of a few days, are located at distances of a few hundreds of pc [210]. Whereas, the nearest known double neutron star system with a period of a few hours is located at around 600 pc [211, 212]. Hence, we choose this distance to mark the nearest NS binaries that would emit mHz GWs.

It is estimated that our Milky Way galaxy contains millions of stellar mass black holes [213]. From binary black hole population simulations for Milky Way-like galaxies [214], it is estimated that binary black holes may be present as close as 1 kpc from Earth, although most of them would be present 8 kpc away, near the galactic center. This also happens to agree with the recent unambiguous detection via astrometric microlensing, of an isolated stellar mass black hole [215], located at 1.58 kpc from Earth. Hence, we choose this distance as an estimate of the nearest stellar mass binary black holes with masses $\sim 10 M_\odot$.

Intermediate mass black holes (IMBHs) of 10^2 – $10^5 M_\odot$ are expected to be found in globular clusters and massive star clusters, but would be more numerous within galactic bulges of large galaxies and within dwarf galaxies [62, 63]. In Milky Way-like galaxies, globular clusters containing IMBHs of 10^3 – $10^4 M_\odot$ are expected to be numerous at distances of 10 kpc from the galactic center, and these IMBHs can emit mHz GWs by merging with stellar mass black holes [64, 65]. Hence, we use the distance to the nearest known globular cluster “M4", of 2.2 kpc, to estimate the whereabouts of the nearest $\sim 10 M_\odot$ & $10^4 M_\odot$ extreme mass ratio inspirals (EMRIs).

A typical large galaxy can contain several “wandering" SMBHs of $\sim 10^6 M_\odot$, spread out across the galactic halo, from near the galactic center to within the dwarf satellite galaxies and anywhere in between [216]. The Milky Way’s central supermassive black hole (SMBH), Sgr A*, also happens to be of mass $\sim 10^6\ M_\odot$ [217]. According to [218], the most promising mHz GW scenario in the IMBH – light SMBH mass range, is of $\sim 10^3\ M_\odot$ IMBHs merging with $\sim 10^6\ M_\odot$ SMBHs. Lastly, the nearest large galaxy to us, M31 (Andromeda), contains a $\sim 10^8\ M_\odot$ central SMBH [219]. For all these reasons, we choose a distance of 8 kpc (distance from Earth to Milky Way’s center, as well as to the closest dwarf galaxy, Canis Major) to represent the location of the nearest $\sim 10^3\ M_\odot$ & $\sim 10^6\ M_\odot$ EMRIs. We choose 0.778 Mpc (distance to M31) to represent the location of the nearest $\sim 10^3\ M_\odot$ & $\sim 10^8\ M_\odot$ EMRIs.

The redshift evolution of the SMBH mass function [220, 221, 222] tells us that, on average, $10^7\ M_\odot$ SMBH mergers may be the most frequent. The nearest known inspiralling SMBHs due to a galaxy merger, are located at a distance of $27.4\,$Mpc [223]. Finally, according to [66], the first SMBH mergers happened at around $z = 10$, when the first galaxies began to merge in the early universe.

We use all this information to generate Fig. 7.6, which shows the maximum response signal, or equivalently, the upper limit on the effective residual noise allowed in an SRGO to detect a GW source at a given distance. From Fig. 7.6, we see that the largest SRGO response signals would correspond to mHz GWs from SMBH binaries in galaxy mergers. EMRIs involving a SMBH, typically the central SMBH of galaxies, or even wandering SMBHs interacting with smaller black holes, would also be significant sources. WD binaries, NS binaries and stellar mass BH binaries within our galaxy would not produce great responses, even if they were individually resolvable sources and located as close to Earth as possible. IMBH EMRIs within globular clusters in our galaxy may also produce reasonably large response amplitudes.

The linear behaviour of each section of the curve in Fig. 7.6, having a negative slope, comes from the inverse relation between the GW source luminosity distance and the GW strain (hence, also the response signal). To generate Fig. 7.6, we assume an observed initial GW frequency of $0.1\,$mHz (the expected lower limit of the mHz regime, which maximises the response signal). Since the GW is cosmologically redshifted over large distances, the emitted GW frequency (or equivalently, the orbital frequency of the binary) is an order of magnitude larger at high redshifts, between z=1 to z=10. Importantly, this causes the chirp rate of the frequency to also be significantly higher. Therefore, the signal amplitude reduces rapidly as the GW frequency increases (as discussed in Sec. 7.6.1), which explains the non-linear behaviour of the curve at high redshifts.

Fig. 7.6 also tells us that an SRGO should aim for an effective residual stochastic noise of $\sim$1 ps or better. Since the effective noise depends not only on the noise of an individual timing measurement, but also on the data sampling rate and observing time, the true residual stochastic noise may be greater than $\sim$1 ps, and can effectively be reduced by collecting data at a higher sampling frequency during the observing run (see Sec. 7.6.2). At this level of noise (or better), an SRGO could potentially detect mHz GW events involving SMBHs starting from within our galaxy, up to galaxy merger events at high redshifts.

Note that, while the sensitivity curve Fig. 7.5 is a curve of unity SNR for the average signal as a function of GW frequency, Fig. 7.6 is a curve of unity SNR for the maximum signal as a function of GW source distance, which also depends on the GW source type.

7.7 Results: GW parameter estimation

We have established a mathematical model to describe a basic SRGO, using which we have analysed its repsonse to GWs, obtained its sensitivity curve, and computed upper limits on the residual noise required to detect astrophysical mHz GW sources. In this section, we obtain first estimations on the capacity of an SRGO to constrain the physical parameters of a GW source. We do this by performing MCMC model fitting on synthetic noisy data generated with our model.

The antenna pattern of a LIGO detector is largely omnidirectional (see Fig. 2 of [224]) and the same is true for an SRGO (see Fig. 2 of paper I). Therefore, even with a high signal-to-noise ratio, a single stationary LIGO or SRGO, in principle, cannot pinpoint the position of the GW source in the sky. However, an Earth-based detector is not stationary, and continuously changes its orientation relative to an incoming GW, due to Earth's rotation. In principle, this should cause the GW source to sweep across the detector's antenna pattern and produce a corresponding characteristic envelope in its response, breaking the degeneracies of omnidirectionality and thus allowing the GW source to be pinpointed. But since LIGO is sensitive to GWs in the kHz frequency range that have short durations, it is unable to fully exploit the effect of Earth's rotation. Hence, three or more LIGO detectors working together are required to triangulate the GW source position via the relative time-delays between their detections from the same source.

On the other hand, since an ideal SRGO would be sensitive to GWs in the mHz frequency range (where the GW signal may last for hours, days, or much longer), it should be able to utilize Earth's rotation to pinpoint the GW source position. The GW source sky localization area, however, would obviously depend on the signal-to-noise ratio. We demonstrate this with an example from our simulation results, where MCMC methods have been used to do GW parameter estimation on noisy data points that were created by adding Gaussian noise to the SRGO response signal.

Fig. 7.7 is an example of the MCMC chain traces, and the diagonal elements of the 9×9 joint posterior corner-plot (shown in Appendix 7.11, Fig. 7.10). We see that in general, at sufficient PSNR values, starting from the correct parameter values, the MCMC chains explore around this location in the 9-dimensional parameter space.

Fig. 7.8 corresponds to the same case as Fig. 7.7, and it shows the sky localization (i.e. the joint posterior of the right ascension and declination of the GW source) for a case corresponding to 32 effective data points taken over 12 hours at a PSNR of 100. The sky localization area is calculated by computing the area on the sky (in deg^2) of the posterior region. The formula we used to obtain calculate the sky localization area from the joint posterior results such as Fig. 7.8, is given by

$$A_{sky}\ \left(\mathrm{deg}^2\right) = \frac{\text{colored pixels}}{\text{total pixels}} \frac{180}{\pi} \Delta\alpha_{\mathrm{src}}\ \Delta \sin\delta_{\mathrm{src}}, \tag{7.17}$$

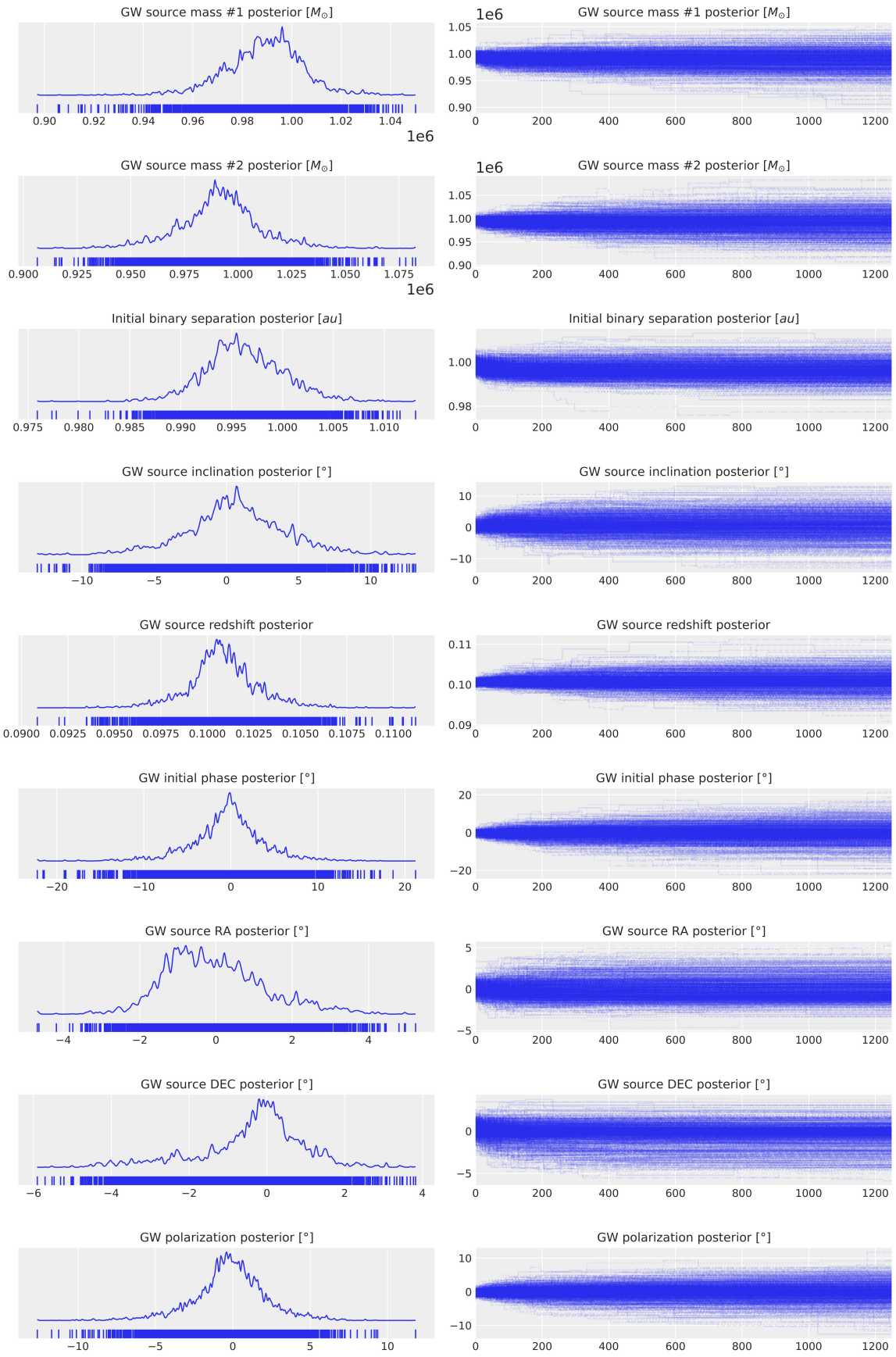

Figure 7.7: On the left are the marginalized posteriors of the fitting parameters and on the right are the corresponding MCMC traces, consisting of 1000 parallel chains with 1250 samples each. The true parameter values for this case are the ones in Fig. 7.1, except the initial separation between the masses which is 1 AU (corresponding to an initial GW period of 3.1 h). 32 data points with artificial noise added (PSNR = 100) are taken over an observing time of 12 hours.

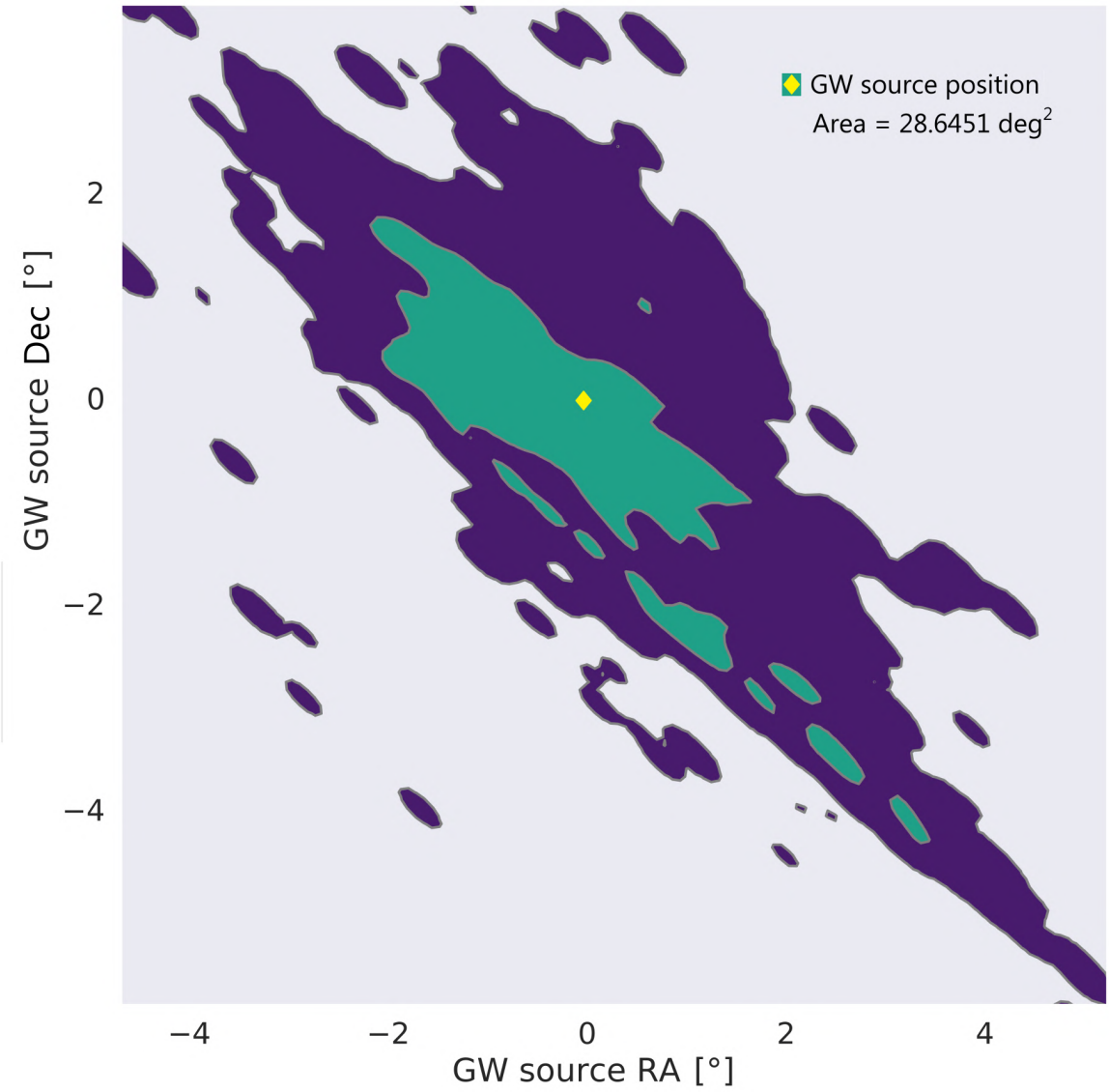

Figure 7.8: The GW source sky localization, i.e. the 3-sigma (99.7%, purple) and 1-sigma (68%, green) HPD region on the joint posterior of the GW source's right ascension and declination. This figure corresponds to the case shown in Fig. 7.7. This shows that a single SRGO can potentially use Earth's rotation to localize the GW source in the sky. The other joint posteriors corresponding to this case may be found in Appendix 7.11.

where we first calculate the area of the sky delimited by the boundary of the figure, and then find the fraction of that area covered by the joint posterior. We do this by multiplying the total area with the ratio of the pixels in the posterior region to the total pixels in the image. For the total area, the width of the figure gives us the range of right ascension, $\Delta\alpha_{\rm src}$, and the height of the figure gives us the range of the declination, $\Delta\delta_{\rm src}$. The $\Delta \sin\delta_{\rm src}$ comes because of calculating the area on the spherical surface of the sky. The $\delta_{\rm src}$ values should be inserted in radians inside the sine, while the $\alpha_{\rm src}$ may remain in degrees, to obtain the final result in deg^2.

Due to the specifics of the MCMC setup, described in Sec. 7.5.5, we miss the antipodal sky localization region, which should exist because placing the ring and/or the GW source at antipodal positions, and/or having the ions circulating in the opposite direction, would all produce the same SRGO response. Although we provide flat priors and allow the MCMC chains to explore over the full range of the angular parameters, the chains seem to explore only around the true parameter values. This is of course due to the nature of the DE-MC algorithm used, which is known for converging quickly to a solution in the parameter space and staying around it. An antipodal region would double the sky localization area, hence, we manually do so for all measurements of sky localization area.

We observe that the joint posteriors we obtain are in many cases not smooth (see Sec. 7.11 for the entire set of joint posteriors corresponding to Fig. 7.8). However, a non-smooth posterior can still be statistically well-behaved and provide meaningful information about the parameters of interest. The smoothness or lack thereof in a posterior distribution does not necessarily indicate the quality or reliability of the results. If the model is highly non-linear or complex, it might naturally lead to non-smooth posteriors. The choice of MCMC sampling algorithm can also play a role. Different algorithms have different exploration and convergence properties, which can affect the smoothness of the obtained posteriors. The 'blobbiness' observed in our posteriors comes from a combination of the complex model and the DE-MC algorithm. We chose the DE-MC because not only did it offer faster computation times, but it also gave more reliable results compared to other algorithms.

Following this brief overview, in the next sub-sections, we shall explore the SRGO parameter estimation results in greater depth.

7.7.1 Variation of parameter estimation errors

We explore the constraints derived from parameter estimation, by computing the variation of the posteriors as functions of some controllable experiment parameters (such as the observation time, data sampling rate and PSNR), for 5 out of the 9 fitting parameters in our model. These are: the GW source component masses, m_1 and m_2 ; the GW source redshift, z ; and the GW source sky position, $\alpha_{\rm src}$ and $\delta_{\rm src}$. The results for $\alpha_{\rm src}$ and $\delta_{\rm src}$ jointly correspond to the sky localization area, shown in Figs. 7.9a and 7.9b. By symmetry, the results for m_1 and m_2 are the same, and correspond to Figs. 7.9c and 7.9d. The results for z have been translated into the GW

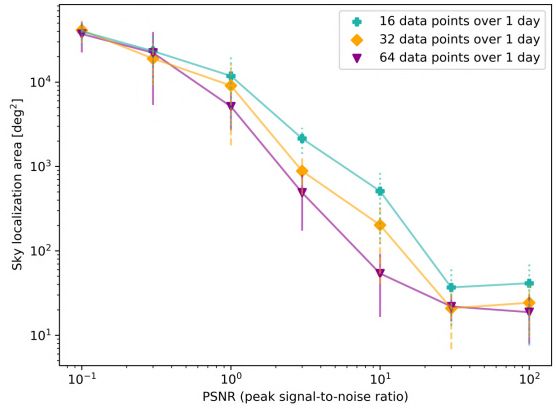

(a) Sky localization area vs. PSNR

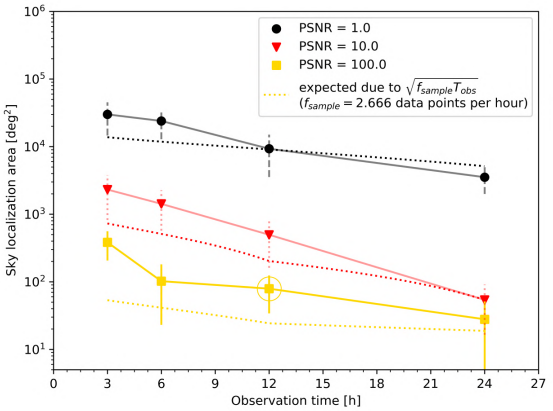

(b) Sky localization area vs. T_{obs}

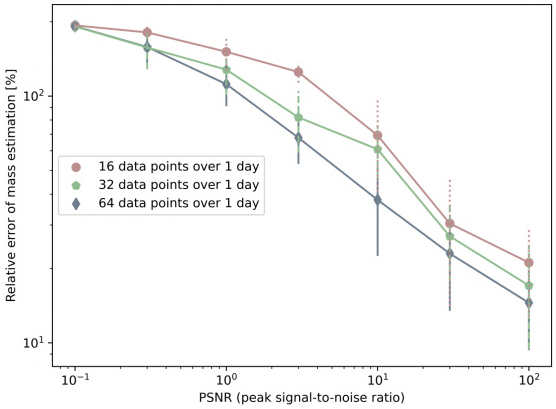

(c) Mass estimation error vs. PSNR

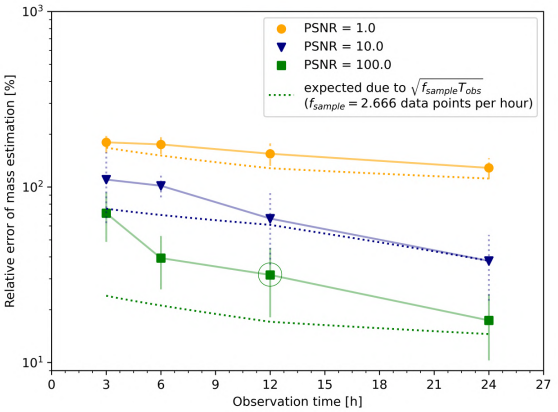

(d) Mass estimation error vs. T_{obs}

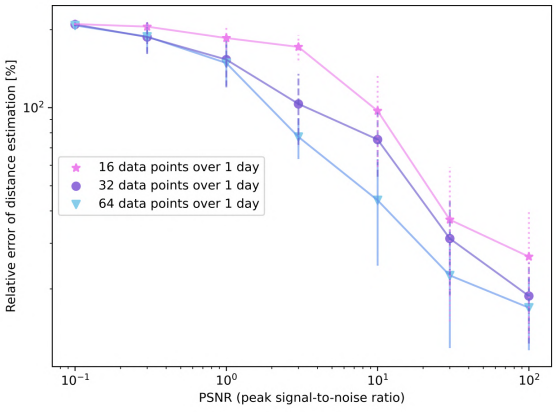

(e) Distance estimation error vs. PSNR

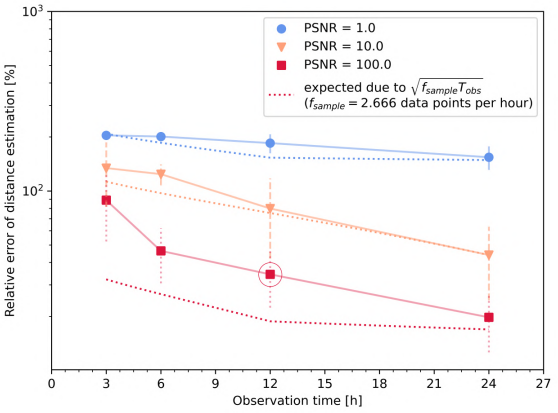

(f) Distance estimation error vs. T_{obs}

Figure 7.9: The parameter estimations of three parameters are shown: GW source sky localization area, relative errors of distance and mass estimation. The left column shows their variation with PSNR for different data sampling rates. The right column shows their variation with observation time at a fixed data sampling rate, for different values of PSNR. The circled scatter points on the right panels correspond to the case shown in Fig. 7.7, Fig. 7.8 and App. 7.11.

source luminosity distance, and correspond to Figs. 7.9e and 7.9f. We choose these 5 parameters as they are astrophysically the most relevant ones.

We generate 16, 32 and 64 data points in this study for a multitude of reasons: first, as explained in Sec. 7.5.5, we use powers of two as this allows for faster computation of the Fast Fourier Transform (FFT). Furthermore, in our computations, 16 data points taken over one day (or 2.666 data points per hour) happens to be the lower limit for the Shannon-Nyquist condition to hold for the case corresponding to Fig. 7.1, which is used to generate results in this section. Hence, this would give us an upper limit on the constraints that can be derived from parameter estimation for a given PSNR and observation time. Also, although in reality it would be possible for a timing detector to make several million measurements within an observation time of hours to days, we use only a small number of data points for computational efficiency. This is justified because a smaller number of data points at a given PSNR may be interpreted as binning a large number of data points that correspond to a lower true PSNR, thus giving the same effective PSNR.

Note that, for results pertaining to parameter estimation, we chose to work with the PSNR (peak signal-to-noise ratio) rather than an integrated SNR, such as that used for the sensitivity curve in Sec. 7.6.2. Integrated SNR is a useful measure for probing the limits of detectability, but large values can be obtained for a given signal and noise level, simply by taking measurements over longer observation times. The PSNR, on the other hand, is independent of the observation time. For a given noise level, the PSNR necessarily reflects whether the signal is strong or weak overall, unlike the integrated SNR. However, if the observation time is fixed, then both kinds of SNR effectively convey the same information.

In Fig. 7.9a, we see that, for a given data sampling rate and observation time, the sky localization area decreases with decreasing noise, and saturates at around a few tens of deg^2 for high PSNR. This is due to parameter degeneracies that cannot be broken further, unless multiple SRGOs are utilized or better models are utilized that, for instance, account for higher-order harmonic modes of GWs [225]. The error bars show the statistical variation of the parameter estimation ("error on the error"), and they increase with increasing noise. This is likely due to the DE-MC algorithm: at low PSNR, it would generally cause the chains to spread over a wide range on the parameter space, but they would sometimes tend to converge to some spurious value on the parameter space, thus increasing the standard deviation of the parameter estimation values obtained from multiple data sets generated for the same case.

Furthermore, at a given PSNR, the sky localization improves upon increasing the data sampling rate. This is because the effective noise is inversely proportional to the square root of the total number of data points, or in other words, the square root of the data sampling rate times the observing time. The parameter estimation becomes unreliable at high levels of noise, with the sky localization area covering almost the entire sky for PSNR values lower than ~ 0.1. An effective PSNR of ~ 80 seems to be the threshold for a single SRGO to achieve its best possible sky localization. As stated in the previous sections, 'effective' implies dividing the noise (or multiplying

the PSNR) by $\sqrt{f_{\rm sample} T_{\rm obs}}$, i.e. the square-root of the number of data points.

For a given PSNR in Fig. 7.9a, upon interpolating over the three data points corresponding to different number of samples, and then extrapolating this, we plot model curves (dotted lines) for different PSNR values in Fig. 7.9b, which show the expected variation of the sky localization due to a change in the total number of samples taken over different observation times, at a fixed sampling rate. This would correspond to a realistic scenario, where the sampling rate of the SRGO would be fixed, and changing the total observation time would change the number of data samples measured. However, when we overplot values (scatter points) obtained by doing an MCMC fit to simulated noisy data, we observe a deviation from the extrapolated model curves. This deviation is greater for higher PSNR values and for smaller observation times. In fact, this deviation shows that changing the observing time does not just have the effect of changing the number of data samples, but further, the effect of Earth's rotation can be exploited to a greater extent to better break some parameter degeneracies. At small observation times, this effect is inefficient, and hence the scatter points perform worse than the model fit. Note that the model fit agrees with the scatter point at an observation time of 24 hours, since that was the fixed observation time in Fig. 7.9a which was used to create the model curves.

An exception to this trend may occur when the Shannon-Nyquist condition is violated, i.e. for a fixed number of data points, a smaller observation time may result in better parameter estimation if increasing the observation time (reducing the data sampling rate) results in aliasing. This scenario would typically not be relevant for a realistic SRGO experiment, where the data sampling rate would be orders of magnitude higher than the GW frequency. Finally, beyond 24 hours observing time, the Earth's rotation cannot break any more parameter degeneracies in principle, and therefore even at high effective PSNR values in Figs. 7.9a and 7.9b, the sky localization tends to saturate at around 20 deg^2.

In Figs. 7.9c, 7.9d, 7.9e and 7.9f, we observe similar trends for the GW source mass and distance estimation as observed for the sky localization. The relative errors of mass and distance estimation saturate at 200% for low PSNR values only because of the bounded flat priors that we use in the MCMC algorithm, mentioned in Sec. 7.5.5. Even at the highest PSNR value, the errors on the mass and distance estimation remain finite, at $\sim$20%. For the same reasons mentioned previously, comparing values from a given curve in Fig. 7.9d (7.9f) with the corresponding values at the same PSNR in Fig. 7.9c (7.9e), we notice the trend that for the same effective PSNR, increasing the observation time improves parameter estimation. However, unlike the sky localization, the errors on the mass and distance estimations do not yet saturate at the highest PSNR values probed, but are expected to eventually saturate at even higher PSNR values.

7.7.2 Parameter degeneracies

In Appendix 7.11, we show an example of the 36 joint posterior pair-plots for our 9 model parameters. These correspond to a case where 32 noisy data points were taken over 12 hours, at a PSNR of 100. The true parameter values for this case are the same as in Fig. 7.1, except that the initial binary separation is 1 AU (corresponding to an initial GW period of 3.1 h). At such a high PSNR, the joint posterior correlations show the degeneracies between the parameters. Here, we try to explain the observed correlations based on the model details described in Sec. 7.5.1:

The joint posterior of the two binary masses (Fig. 7.10a) shows an anti-correlation, because upon increasing one of the masses, the other must be decreased to have the same chirp mass. The two binary masses are also positively correlated with the initial binary separation (Figs. 7.10b and 7.10i), since increasing the mass increases the GW strain amplitude and also affects the frequency evolution, which can be countered by increasing the initial binary separation. The positive correlation between the masses and the GW source redshift (Figs. 7.10h and 7.10k) has already been explored in detail in Sec. 7.6.3. It exists because increasing the redshift decreases the response signal, which can be countered by increasing the mass of the binary. Instead of increasing the binary mass, we can also counter this by increasing the initial binary separation, which reduces the GW frequency, thus increasing the response signal, as discussed in the beginning of Sec. 7.6.1. That is why the joint posterior between the source redshift and the initial binary separation also shows a positive correlation (Fig. 7.10q).

An interesting joint posterior to analyze is the source redshift, z vs. the source inclination angle, i (Fig. 7.10v). The degeneracy between the source distance, d_L, and inclination angle is well known in GW astronomy. Therefore, we expect them to be anti-correlated, since increasing the source distance decreases the GW strain amplitude, but decreasing the inclination angle can counter this. However, in Fig. 7.10v we consider the correlation of i with z, rather than with the luminosity distance, and z also affects the chirp mass and GW frequency. Therefore, in our results, the $z - i$ joint posterior shows no correlation, since these two parameters control very different aspects of the response signal. Further, a small change in z corresponds to a large change in d_L. If a posterior of d_L and i were computed, for an approximately constant z, then the expected degeneracy may be easily seen.

Another noteworthy joint posterior is that of the GW polarization angle vs. the GW initial phase (Fig. 7.10ag), which shows a strong linear correlation. This can be derived analytically for our special case of $i = 0$. For this case, the response signal Eq. (7.4) can be re-written as follows, after substituting all the terms and collecting the common terms into a factor h_0,

$$\Delta T_{\mathrm{GW}} = \int_{t_0}^{t_0+T} h_0 \sin^2\theta \Big(\cos(2\psi)\cos(2\pi f t + \delta_0) + \sin(2\psi)\sin(2\pi f t + \delta_0) \Big) dt = \int_{t_0}^{t_0+T} h_0 \sin^2\theta \cos(2\pi f t + \delta_0 - 2\psi) dt. \quad (7.18)$$

The above equation shows that, $i = 0$ corresponds to circularly polarized GWs observed with an SRGO, which may be interpreted as GWs with a constant phase, δ_0, whose polarization axes are rotating in a circle with an 'effective' GW polarization angle, $\psi_{\mathrm{eff}} = \psi - \pi f t$. Other parameters being fixed, if we Taylor-expand ψ as a function of ψ_{eq} around its true value, then for small deviations of ψ_{eq} from its true value, ψ will be linear in ψ_{eq}. Hence, the above equation explains why the joint posterior of ψ_{eq} and δ_0 shows a linear correlation. Note that all values within the parentheses of the above equation are in radians, while the values shown in Fig. 7.10ag are in degrees, but these values are consistent with the Taylor series assumption that deviations of ψ_{eq} from its true value, in radians, is small.

Thus, for circularly polarized GWs, changing the initial phase of the GW can produce the same signal as changing the GW polarization angle. If the Earth were stationary, this would be the same as beginning the observation run at a different time.

7.8 Discussion

Why do we choose ultrarelativistic test mass particles?

It is currently unclear, but using ultrarelativistic ions might be beneficial (Schmirander et al., in preparation). This is because a single ion with sufficiently high energy would, in principle, by its sheer momentum, appreciably attenuate the effect of many stochastic and deterministic noise sources that would directly perturb the ion (some of which were explored in paper I). This would also allow a coasting ion to deflect or deviate less from its ideal orbit, and last longer in a non-ideal vacuum, thus potentially allowing for longer SRGO observation runs.

What are the limitations and caveats of this study?

One of the primary limitations of this study is the simplistic static Gaussian noise model for the residual system noise, based on the assumption that our hypothetical storage ring facility is capable of attenuating most of the (yet un-studied) noise sources, similar to LIGO. We cannot yet model noise sources in detail, especially their frequency and time dependence, until a thorough study is conducted (Schmirander et al., in preparation).

Next, our GW waveform models do not account for the spins of the compact objects in the binary, the eccentricity of their orbit, and other parameters corresponding to realistic binary systems. While our model contains 9 unknown fitting parameters, realistic GW models contain around 15 to 17. However, as a first step towards establishing a novel experiment concept, for the sake of consistency and ease of analysis, it is better to use a realistic toy model for making order-of-magnitude estimations, rather than to use complex and detailed models from the very beginning, which can make analysis quite difficult in a topic that has not been explored to such an extent prior to this study. Although our GW source and ring models are simple, they are realistic enough to provide correct orders of magnitude of the estimates. Perhaps, incorporating detailed GW waveforms and storage ring models is the next logical step in this series of works.

We also do not model the merger and ringdown phases, and cover only the inspiral phase of the binaries. However, because the response signal tends to decrease with increasing GW frequency (Fig. 7.3), the merger and ringdown phases would likely not produce an SRGO response signal as large as the one during the inspiral phase.

Furthermore, our GW source models, which are derived from post-Newtonain (PN) analysis, cannot accurately model EMRIs (extreme and intermediate mass ratio inspirals). In Sec. 7.6.3, Fig. 7.6, some GW sources that are actually EMRIs, have been estimated with our post-Newtonian GW waveform model, which is not optimal. But since we are interested in order-of-magnitude estimates and since we do not expect the difference between our model and an EMRI GW waveform to be orders-of-magnitude greater, we regard this as a justifiable simplification. This is supported by [226], where it can be seen that the simple PN waveform models are accurate enough to model EMRIs for small observation times of a few hours or days, as considered in our study.

Many of our results have been generated by averaging over as many parameters as possible, so that the conclusions interpreted from them may remain accurate and general. However, some of our conclusions are extrapolated based on results for a specific and arbitrary combination of parameters, corresponding to Fig. 7.1 (with some variations which are described in the sections pertaining to each result). This was done for cases where averaging over parameters was very difficult or computationally expensive. These include results in Sects. 7.6.1 and 7.7. However, we do not expect the parameter-averaged results to be different in order-of-magnitude for these cases, and hence expect them to be sufficient for first estimates and general conclusions. For instance, the results in Sec. 7.6.1, which are based on scaled values of the PSNR, are intrinsically independent of some parameters, such as the GW source mass and distance. Moreover, we can make estimates of how some of the results would change for a different set of parameters. For example, the results of Sec. 7.7, for a different set of true parameters, can be estimated by combining the results of Sects. 7.6.1 and 7.7.1, which should at least be correct in order of magnitude.

Lastly, we have not yet accounted in the SRGO response formulation, the effect of

the GW on the storage ring magnetic field, which may possibly boost the response signal. This would be included in future works (Schmirander et al, in preparation).

How to measure the instantaneous initial ion speed, v_i?

Two timing detectors placed close by would detect a passing ion with a delay. Dividing the known distance covered by the ion with this timing delay would give us v_i. This measurement could be made more accurate by repeating this procedure over the first several revolutions and then taking an average value. However, performing this procedure with a single timing detector (i.e. dividing the orbit circumference by the time interval between two successive detections of the same ion by a single detector) would be less accurate, because although the time-varying quantities would change negligibly during a single ion revolution, but the ion would still be affected by the anisotropy of the spacetime. Hence, compared to the former procedure, this way would give us a slightly worse substitute for the quantity that we wish to measure.

How to measure $\Delta T_{\rm GW}$?

Using v_i and the circumference of the ion orbit, we can predict the expected arrival times of the ion to the timing detector. These must then be subtracted from the actual ion arrival times that are measured by the timing detector. The result will constitute the discrete noisy data points $\Delta T_{\rm GW}$, which when plotted against the expected arrival times, will look like Fig. 7.1. This is why the second term within the integral of Eq. (7.4) differs from that of Eq. (6.13), when we measure $v_i = v_0 \left(1 + \frac{h_{\theta\phi\psi}(0)}{2}\right)$ instead of v_0. Since the speed is used to predict the times when the ion would arrive at the detector, a different speed would change the predicted ion arrival times, and thus, also the signal (which is the observed arrival time minus the predicted arrival time of the ion).

Do GWs affect the atomic clock of the timing detector?

Since the storage ring ion clock and the atomic/optical clock of the timing detector would be located next to each other, they would both be affected in the same way due to the temporal component of the GW metric (or any other spacetime metric). Therefore, in principle, the temporal component of the spacetime metric cannot be measured by a comparison between the ion clock and atomic clock geodesics (the working principle of SRGO). However, since the location of the atomic clock would be stationary in the reference frame, while the ion would revolve in an anisotropic GW spacetime, the spatial components of the GW metric would affect the storage ring ion clock differently as compared to the atomic/optical clock. This difference would result in the response signal that can, in principle, be measured by an SRGO. This is the reason why, as explained in Sec. 7.6.3, laser and atom interferometer GW detectors cannot probe the anisotropy of a static distorted spacetime (such as very low frequency GW spacetimes over short observation times), even in principle. Whereas, this would possible in principle with an SRGO, even in the absence of Earth's rotation. However, practically, this might never be tested because of the stochastic gravitational wave background (SGWB), which exists due to an overlap of a large number of unresolved and incoherent astrophysical GW sources at low

frequencies [84, 85, 86].

Why did we choose MCMC methods over Fisher Information for parameter estimation?

The Fisher Information Matrix (FIM) can be described as the inverse of the covariance matrix of some distribution. It may also be interpreted as the curvature of the log-likelihood graph. The FIM can be calculated analytically, requiring only the model that generates the response signal. This makes the FIM a fast and simple method of obtaining the precision of the parameter estimation pipeline without actually having to make a measurement of artificial noisy data. However, the FIM does have limitations: It assumes a model with linearly correlated parameters, a detector with Gaussian noise, and a high SNR. It has been shown that for a non-spinning binary GW source model with 9 unknown parameters such as ours, at total binary mass higher than $10.0M_{\odot}$, the standard deviation predicted by the FIM does not agree with the standard deviation of a fully calculated posterior by MCMC methods [227].

Further, an MCMC fit gives us the added advantage of studying correlations between parameters, and getting a qualitative impression of how well-behaved a fit is.

What are the implications for conducting an SRGO experiment at the FCC (Future Circular Collider)?

FCC [228] is a proposed circular particle accelerator which will be able to accelerate ultrarelativistic ions at even higher energies than the LHC. This could increase the natural attenuation of any stochastic noise sources directly acting on the ions, due to the ions having a higher relativistic mass or momentum. However, the proposed 100 km circumference of the FCC would have implications for noise levels from sources such as seismic noise, gravity gradient noise and others, which unlike the expected SRGO response signal, would likely be sensitive to the ring size. Currently, it is unclear whether a larger or smaller ring size would be more suitable for an SRGO experiment. It is hoped that, upon detailed computational modeling of the noise sources, an optimal configuration within the parameter space can be found, which reveals the optimal ring size (Schmirander et al., in preparation).

However, another pertinent point regarding the FCC in the context of this study is that, innovation in particle accelerator technology through big projects such as the FCC would indeed help the future realisation of an ideal SRGO facility. As we recall from Sec. 7.5.2, the ideal SRGO assumed in this study currently seems to be beyond the frontier of modern technology, and work on the FCC may help push that frontier in ways that serendipitously unlock solutions for realising an SRGO.

What are the potential implications for multi-messenger astronomy?

The yet undetected mHz GW events are also predicted to be associated with the emission of electromagnetic radiation and neutrinos [58, 229, 230, 231]. For transient astrophysical events that correspond to high frequency GWs such as those detected by LIGO, the usual case for multi-messenger observations is of the event

first being detected by the omnidirectional GW detectors, which then perform fast parameter estimations and send out real-time alerts to other observatories, providing the estimated GW source component types, masses, spins and importantly, the sky localization region. An effort is then made to quickly and simultaneously observe the GW event via the other messenger signals, using the alert information. However, for mHz GW events, fast alert response would be of lesser concern, because most of these events would be long-lasting. Therefore, improving parameter estimation, especially the sky localization, would be most important for multi-messenger studies of mHz GW events. Other than improving detector sensitivities, this is best achieved by collaboration between multiple mHz GW detectors. It is estimated that a proposed mHz GW detector such as LISA, by itself, would not be good enough to pinpoint the host galaxies of mHz GW sources [174, 229]. On this front, it is clear that the successful realization of an SRGO would greatly complement other mHz GW detectors such as LISA, and improve the GW alerts for multi-messenger observations.

Assuming that a mHz GW event is detected simultaneously by LISA and SRGO, and further assuming that the realized SRGO has effectively the same capabilities as the hypothetical system considered in Sec. 7.5.2 of this study, then we can make a rough estimation of the improvement in the GW source sky localization due to a combination of SRGO and LISA. The LISA sky localization for massive black holes is estimated to be $1 - 100\,\mathrm{deg}^2$, and LISA would be lagging the Earth orbit by $20°$ [28]. In the optimistic case, assuming that a single SRGO on Earth manages to localize the same GW event between $4 - 40\,\mathrm{deg}^2$ as obtained in Sec. 7.7.1, then by combining this data via simple 3D geometry, we can roughly estimate that the improved sky localization may be as good as sub–deg^2, and as bad as a few tens of deg^2. Overall, this would be a very good improvement, and it could be made even better by having multiple SRGOs at different locations on Earth.

7.9 Summary and Conclusion

In Sec. 7.3, we discuss previous studies on storage rings as GW detectors, highlighting what they missed, and explaining the novelty of our idea. We provide comparisons and analogies between an SRGO and other known GW detection techniques. We also discuss references that support our findings and throw light on potential ways for realizing an SRGO. In Sec. 7.4, we provide a review of the theory behind an SRGO, and revise important formulae to display them in a better format. Sec. 7.5 describes the mathematical models and numerical procedures of our simulation code.

In Sec. 7.6.1, we study the variation of the response signal with the experiment parameters, obtaining useful physical insights about how an SRGO works. Our results suggest that the response signal would be maximised by placing an SRGO at equatorial latitudes on Earth and by having long observation times. In Sec. 7.6.2, we numerically obtain the SRGO sensitivity curve, which shows that an SRGO would be sensitive to the mHz GW regime provided that a minimum observation time (run time of the storage ring) of at least a few hours can be achieved in an SRGO

experiment. In Sec. 7.6.3, we find that a typical SRGO would require an effective residual noise lower than $\sim$ 1ps to detect astrophysical mHz GW sources. At this level of noise, an SRGO could potentially detect mHz GW events involving supermassive black holes starting from within our galaxy, up to galaxy merger events at high redshifts.

The results of Sec. 7.7 prove that even a single SRGO can, in principle, perform accurate GW parameter estimation, being able to provide a closed region on a sky map for the GW source localization, which would improve with increasing PSNR. In Sec. 7.7.1, we find that an effective PSNR (i.e. true PSNR times the square root of the total number of data points) of at least ~ 80 would be required to constrain parameters effectively with a single SRGO, which may be achieved by a combination of noise reduction and increasing the data measurement rate. At this effective PSNR or higher, a single SRGO would be capable of constraining the GW source parameters (such as the sky localization area, relative distance and mass estimations, etc.) to within a few tens of percent of their true values. In Sec. 7.7.2, we obtain more physical insights by studying the parameter degeneracies of an SRGO experiment.

Finally, in Sec. 7.8, we discuss the limitations of this study; justify some approaches we have taken in this study; answer fundamental questions about the working principle of an SRGO; and discuss future implications of realizing an SRGO.

In conclusion, SRGO seems promising as a near-future Earth-based GW detector sensitive to the yet undetected mHz GWs. It could complement space-based detectors such as LISA, or even make detections prior to the launch of LISA, assuming that rapid technological development during this decade allows a functional SRGO to be built. The main effort required in this direction would be detailed studies, techniques and technologies to handle noise sources; finding the optimum operation mode of a storage ring for an SRGO experiment; techniques and technologies for the timing data readout. Further studies of single ion storage rings and improvement in vacuum technology would also help.

7.10 Contribution to $\Delta T_{\rm GW}$ from beam orbit shape distortions

Consider a circular ion beam of radius R, which gets distorted into, say, an ellipse with axes $R \pm \Delta R$, where $\frac{\Delta R}{R} = h$ represents the GW strain amplitude, which is much smaller than unity.

The perimeter of a near-circular ellipse is approximated to an excellent accuracy by Ramanujan's formula [232],

$$C_{\rm ellipse} = \pi(a+b)\left(1 + \frac{3\lambda^2}{10 + \sqrt{4 - 3\lambda^2}}\right). \tag{7.19}$$

Here, $a = R + \Delta R$, $b = R - \Delta R$, $\lambda = \frac{(a-b)}{(a+b)} = h$. The error in Ramanujan's approximation is $\mathcal{O}(h^{10})$. Over many revolutions, the ion circulation time deviation will be proportional to a time integral over the difference between the perimeters of the distorted and ideal orbit shapes,

$$\Delta T_{\text{orbit}} \propto \int_{t_0}^{t_0+T} (C_{\text{ellipse}} - 2\pi R)\, dt \propto h^2. \tag{7.20}$$

This result is, in general, also true for more complex beam orbit shape distortions caused by other sources (such as seismic activity), as long as the corresponding quantity equivalent to h is small.

7.11 Corner plot shown as individual joint posterior plots

Due to space constraints, we show in Fig. 7.10, the 36 individual joint posterior pair-plots corresponding to the non-diagonal elements of the 9×9 corner plot. The diagonal elements of the corner plot have been shown in Fig. 7.7. In each pair-plot, we show the 1-sigma (68%, green) and 3-sigma (99.7%, purple) highest posterior density (HPD) regions. The results of Fig. 7.10 are discussed in Sec. 7.7.2.

The true parameter values for this case correspond to those in Fig. 7.1, except the initial binary separation which is 1 AU (corresponding to an initial GW period of 3.1 h). 32 data points have been taken over an observing time of 12 hours at a PSNR of 100. The following table provides the true parameter values corresponding to each posterior shown in Fig. 7.10:

True Parameter Values		
Name	Symbol	Value
GW source mass 1	m_1	$1.00 \times 10^6 M_\odot$
GW source mass 2	m_2	$1.00 \times 10^6 M_\odot$
Initial binary separation	r_0	1.00 au
GW source inclination	i	0.00°
GW source redshift	z	0.10
GW initial phase	δ_0	0.00°
GW source right ascension	α_{src}	0.00°
GW source declination	δ_{src}	0.00°
GW source polarization	ψ_{eq}	0.00°

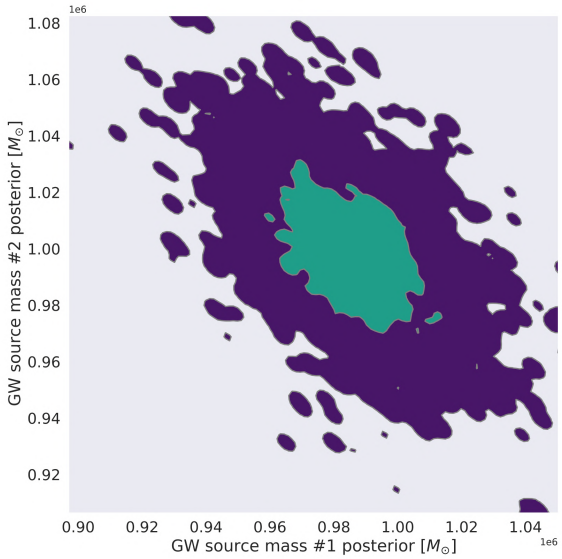

(a) m_1 and m_2

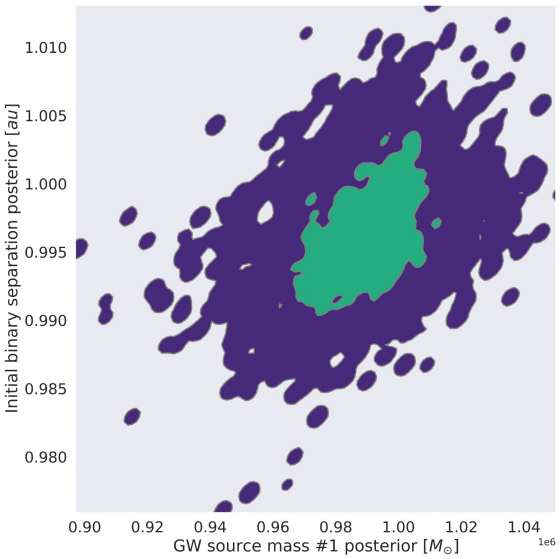

(b) m_1 and r_0

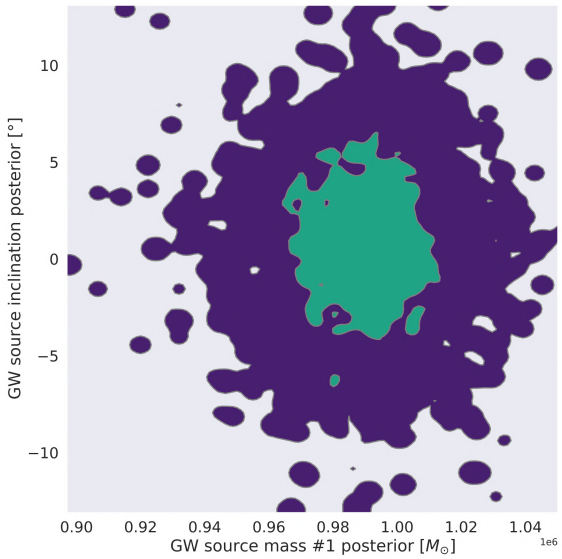

(c) m_1 and i

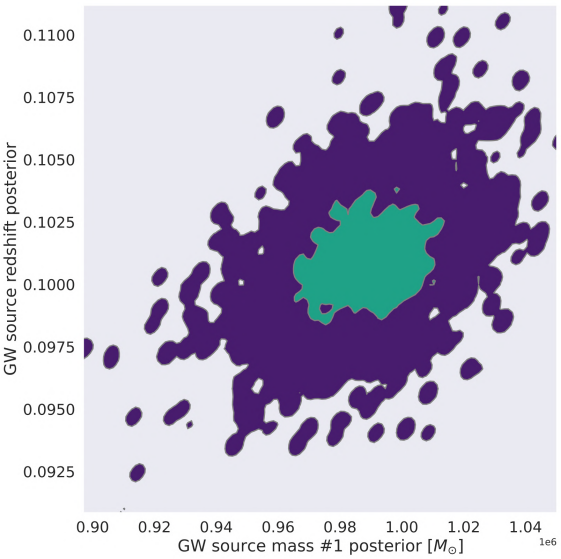

(d) m_1 and z

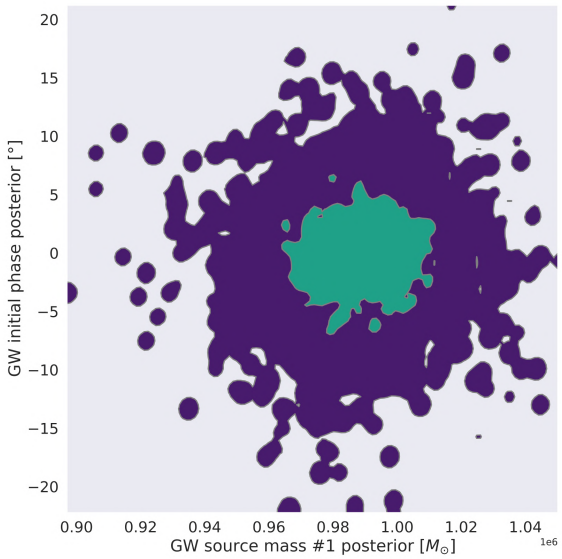

(e) m_1 and δ_0

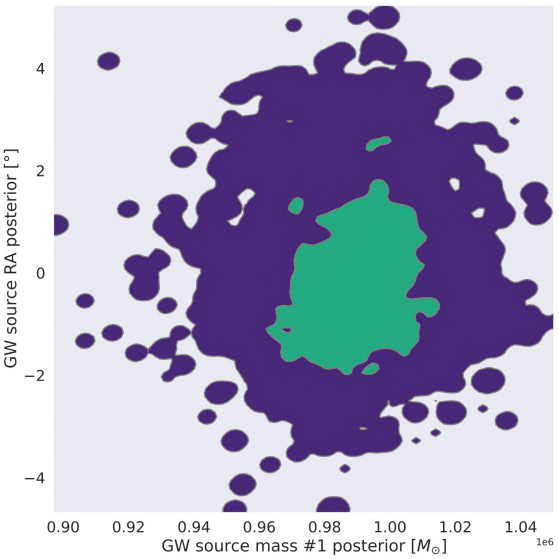

(f) m_1 and α_{src}

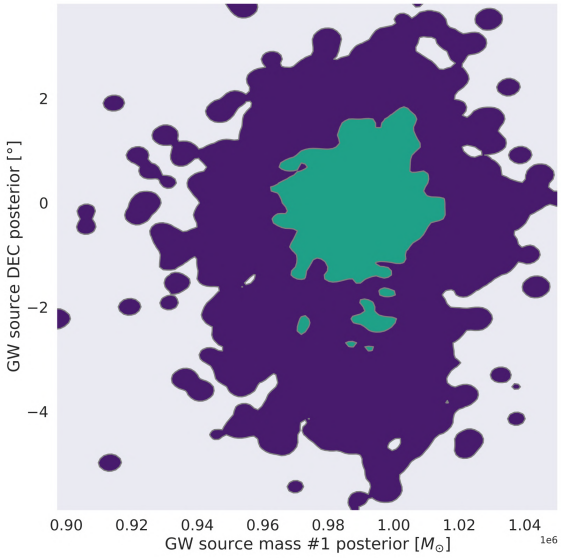

(g) m_1 and δ_{src}

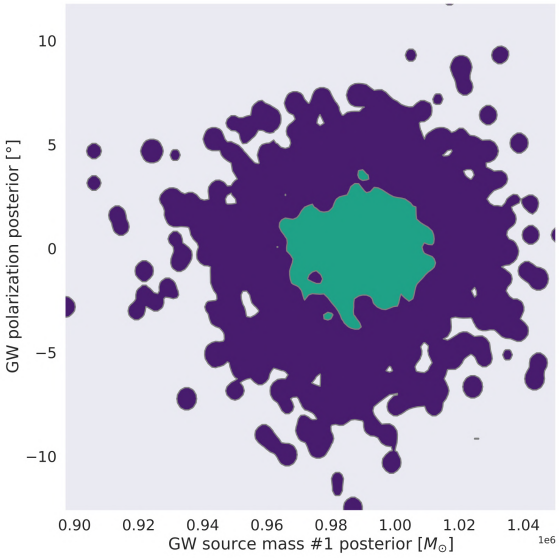

(h) m_1 and ψ_{eq}

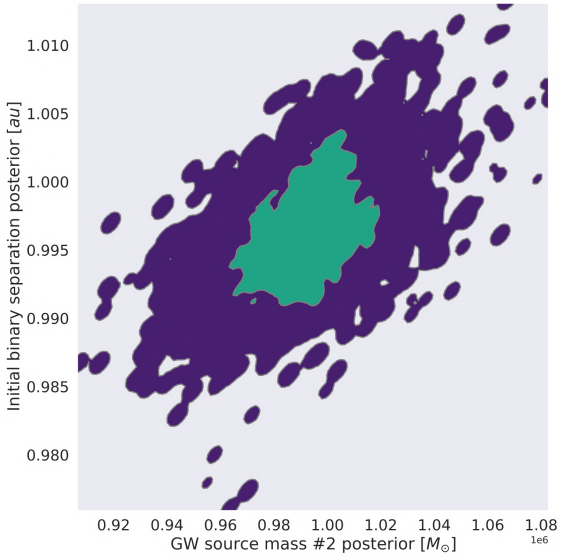

(i) m_2 and r_0

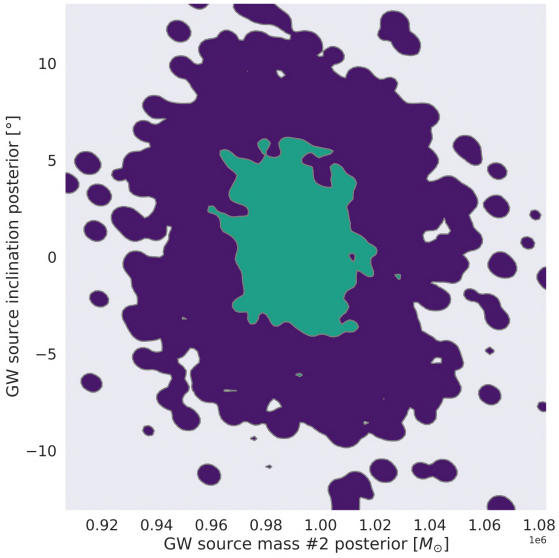

(j) m_2 and i

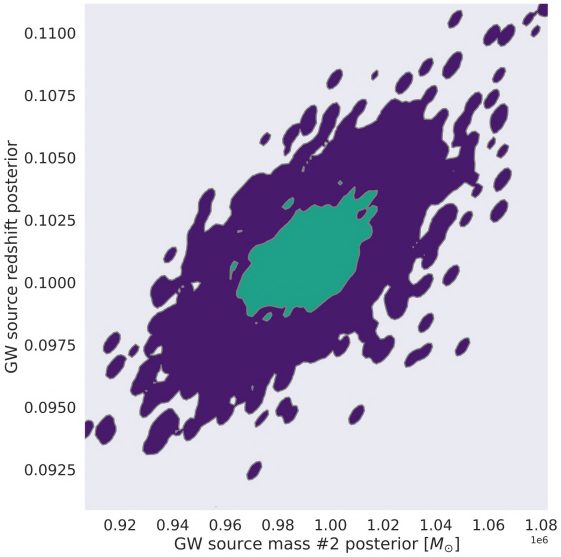

(k) m_2 and z

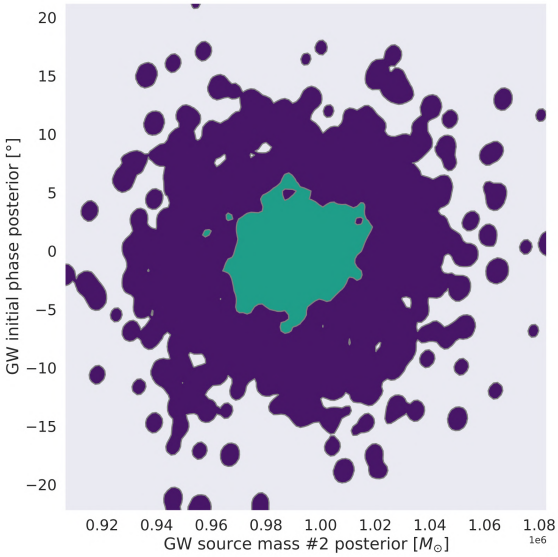

(l) m_2 and δ_0

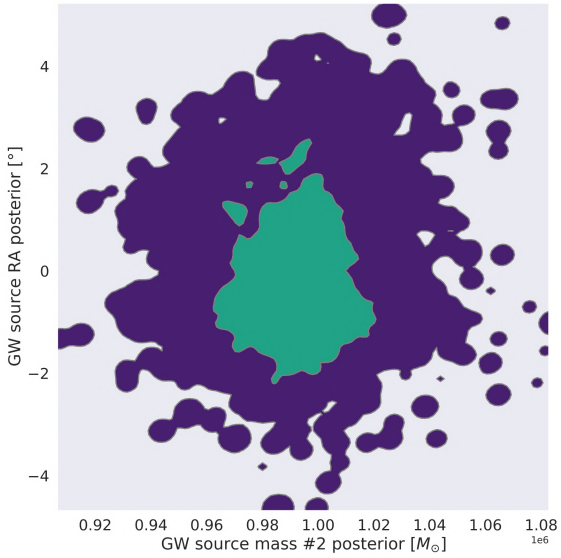

(m) m_2 and α_{src}

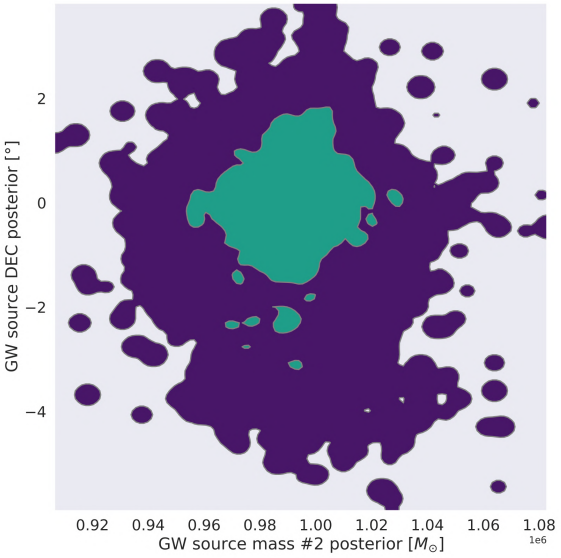

(n) m_2 and δ_{src}

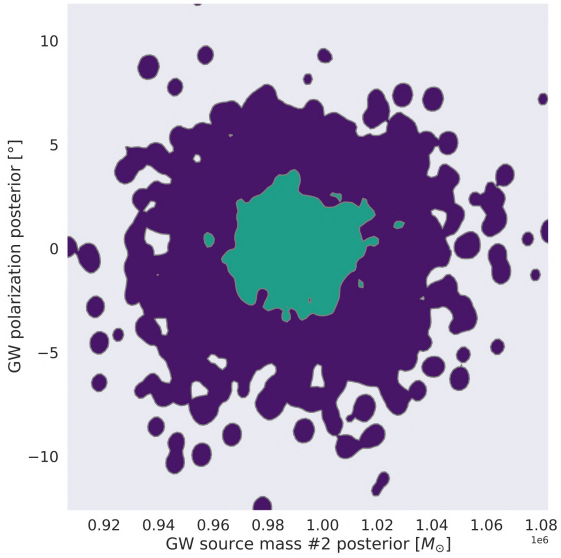

(o) m_2 and ψ_{eq}

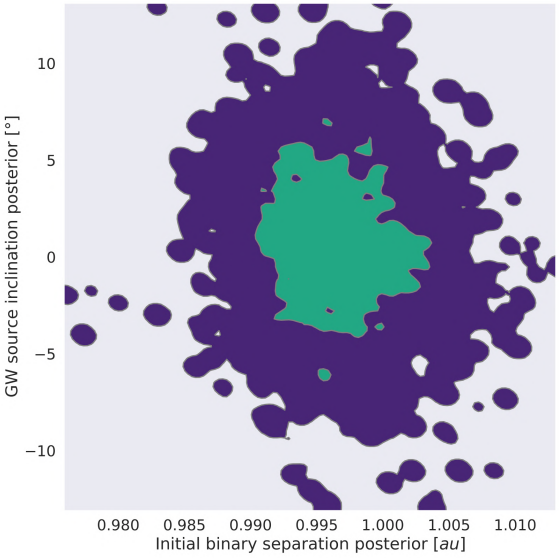

(p) r_0 and i

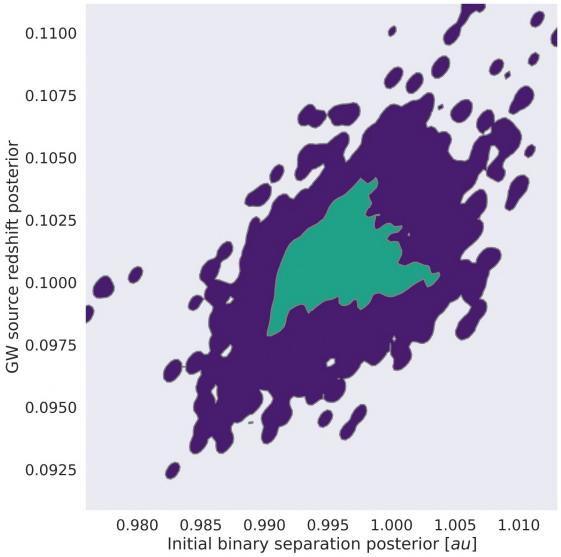

(q) r_0 and z

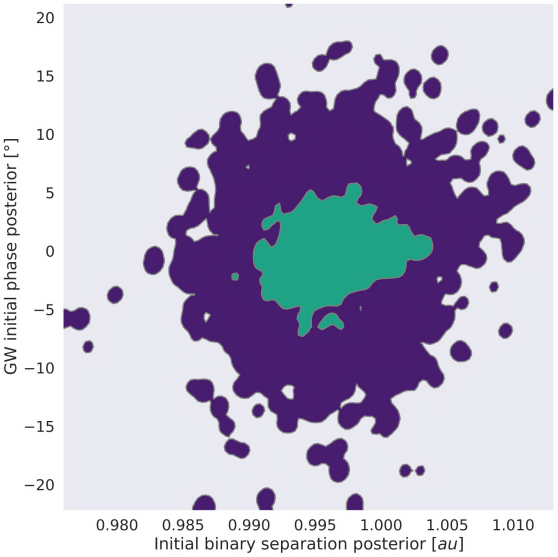

(r) r_0 and δ_0

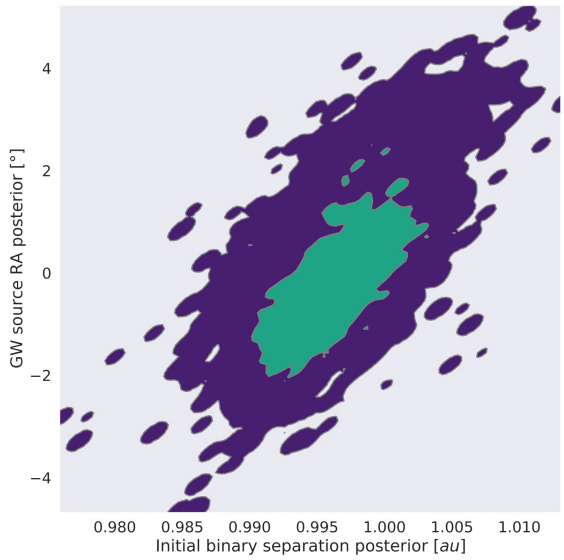

(s) r_0 and α_{src}

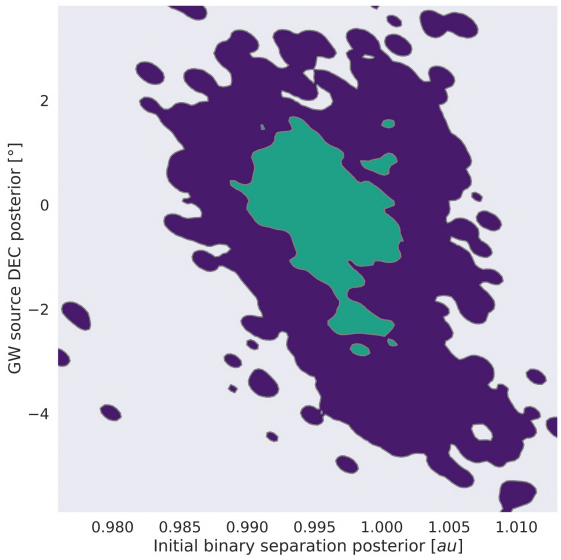

(t) r_0 and δ_{src}

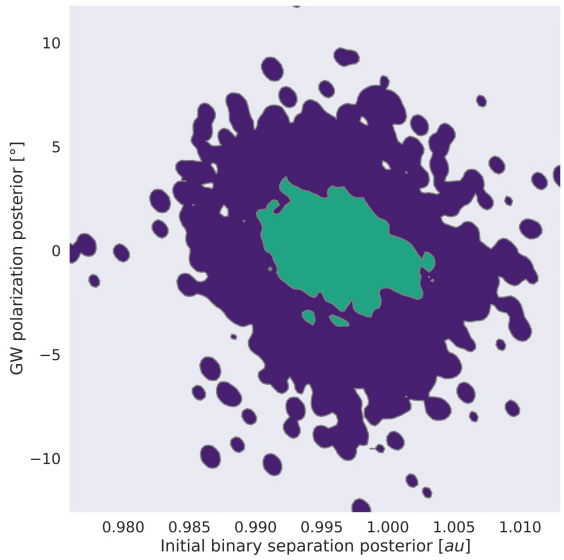

(u) r_0 and ψ_{eq}

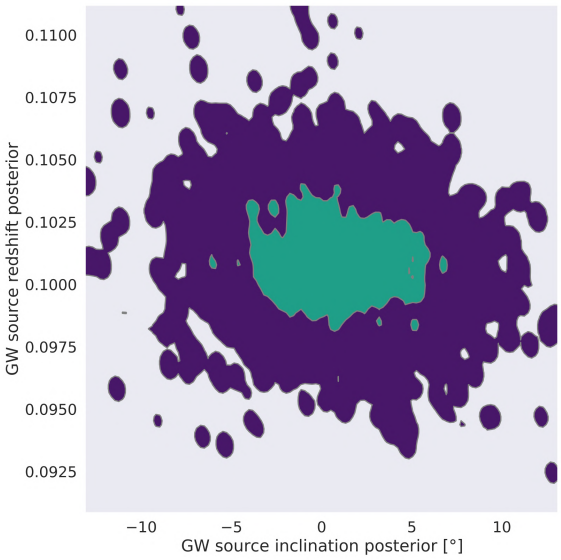

(v) i and z

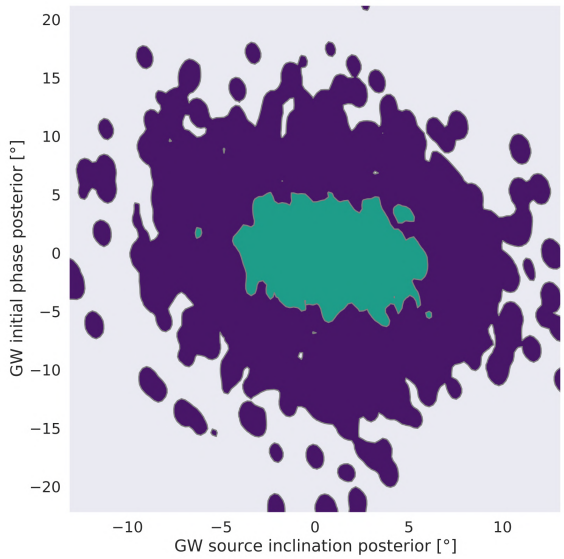

(w) i and δ_0

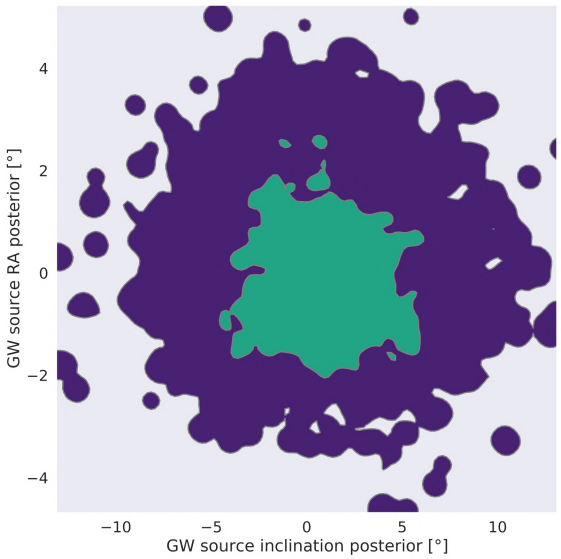

(x) i and α_{src}

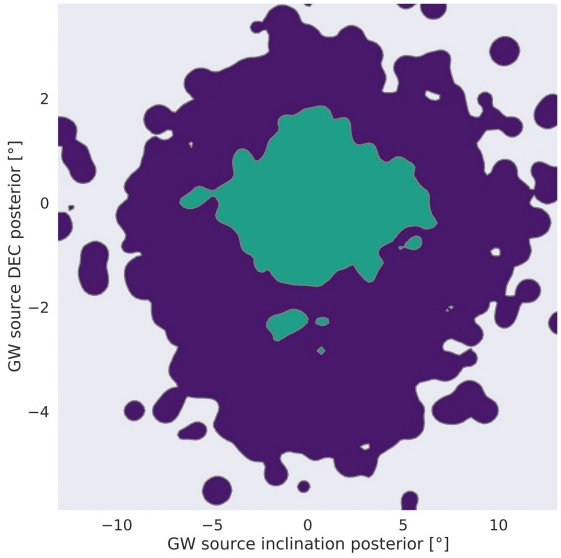

(y) i and δ_{src}

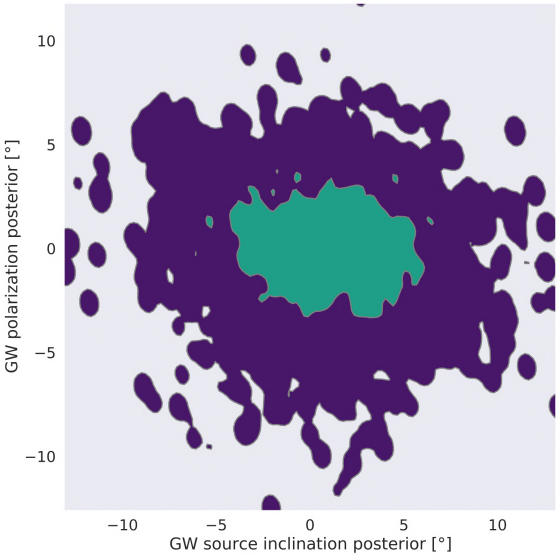

(z) i and ψ_{eq}

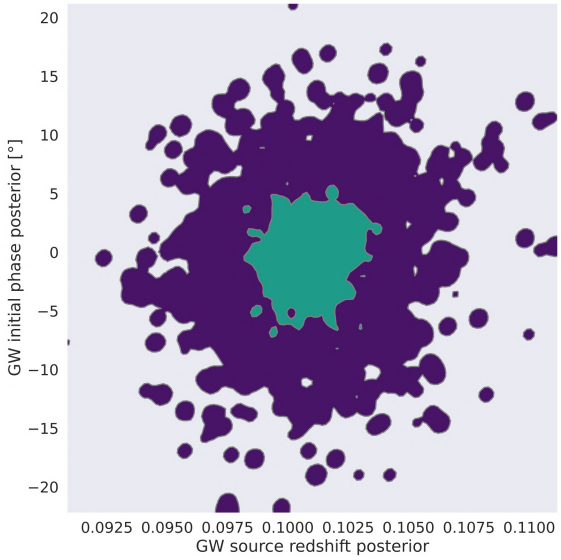

(aa) z and δ_0

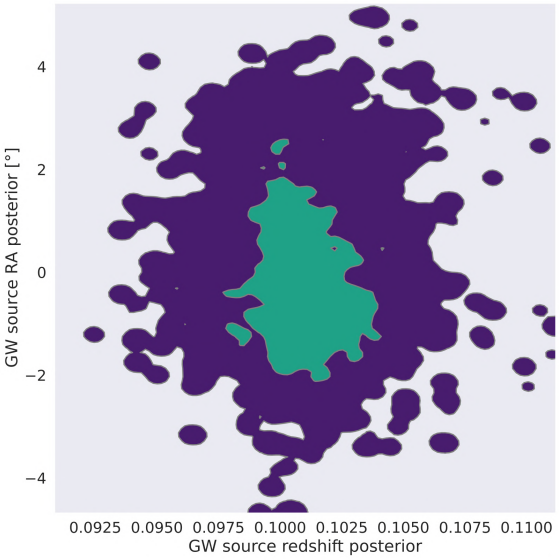

(ab) z and α_{src}

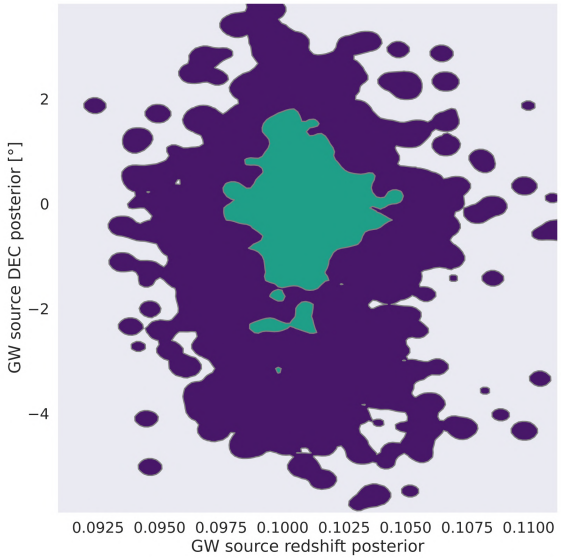

(ac) z and δ_{src}

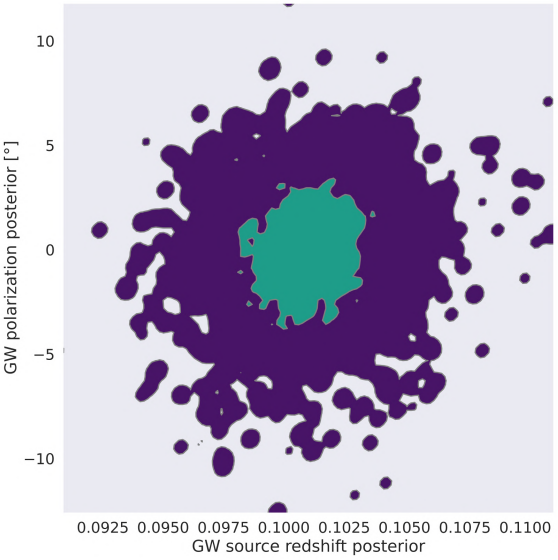

(ad) z and ψ_{eq}

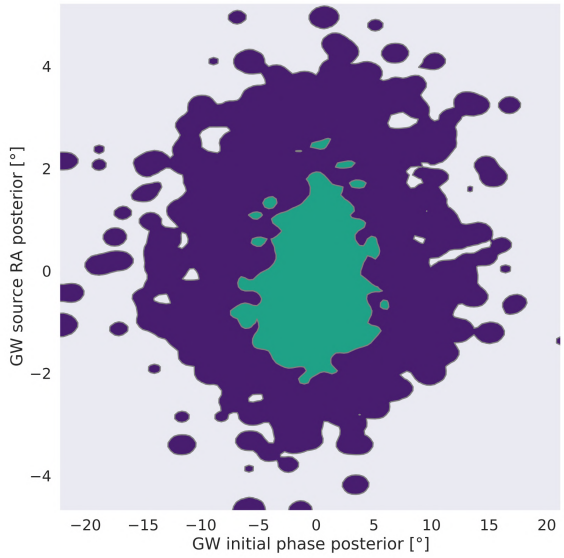

(ae) δ_0 and α_{src}

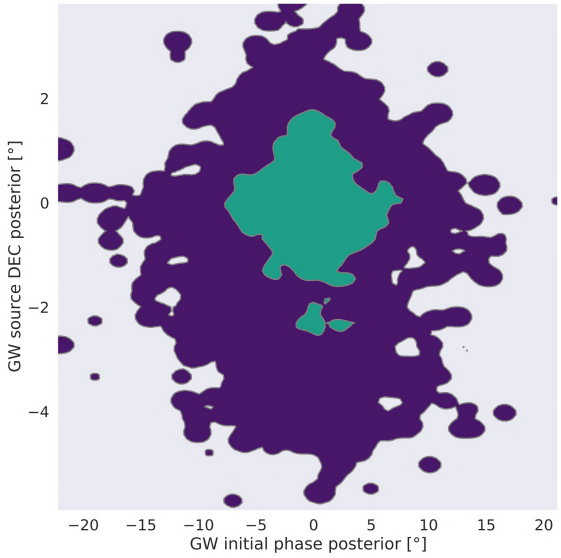

(af) δ_0 and δ_{src}

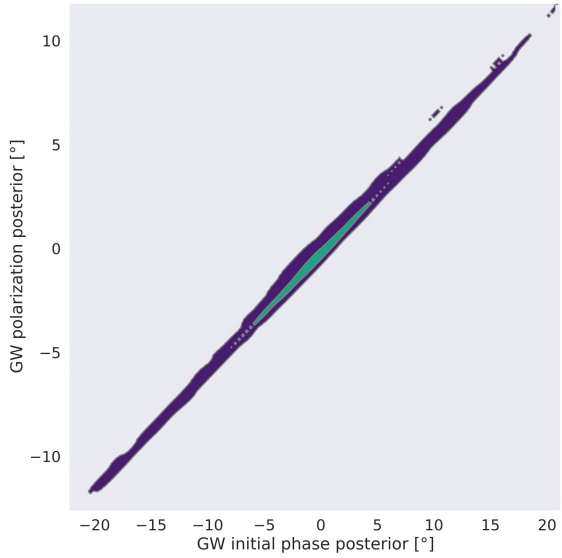

(ag) δ_0 and ψ_{eq}

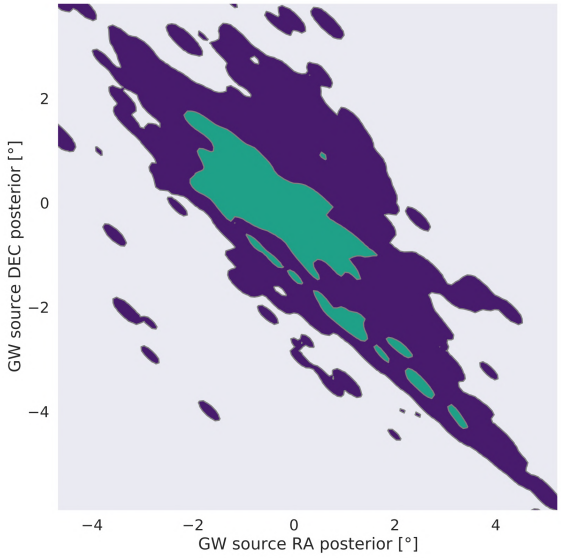

(ah) α_{src} and δ_{src}

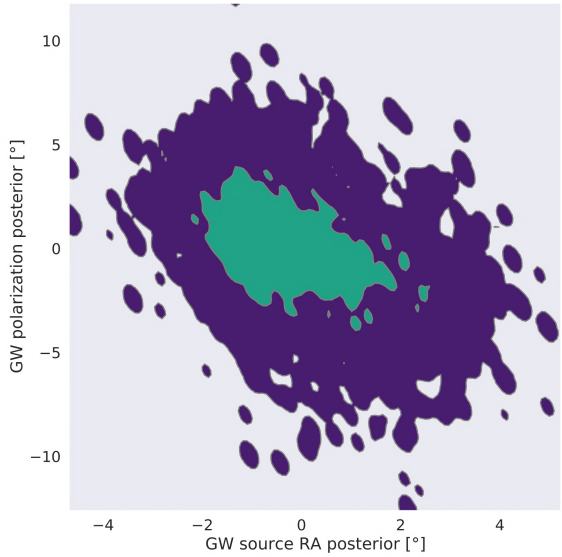

(ai) α_{src} and ψ_{eq}

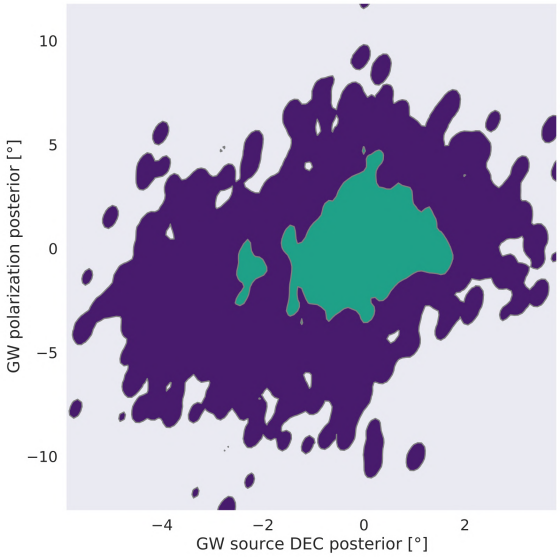

(aj) δ_{src} and ψ_{eq}

Figure 7.10: Individually shown joint posteriors of the 9×9 corner plot obtained after MCMC parameter estimation, for true parameter values described in Appendix 7.11.

Chapter 8

Overview of Unstudied Noise Sources

8.1 Introduction

In Sec. 6.6, some basic models and order-of-magnitude estimates of the major noise sources in an SRGO experiment were discussed, which were made based on the limits of current technology, the available studies of LHC, and the scope of this work.

Obviously, more accurate models of noise sources would be needed for advancing towards a realistic SRGO, for which purpose, detailed mathematical modeling, numerical simulations and experimental studies would be required. An embarkation of this long journey has already begun (Schmirander et al., in preparation).

In this section, we would like to conceptually discuss additional noise sources to those discussed in Sec. 6.6, covering a more extensive range of the total noise. We focus on noise sources which, (a) would continue to persist despite assuming ideal conditions and futuristic technology, (b) might have a significant contribution as noise on the expected signal, and (c) cannot be readily modeled, or have not been previously studied in the literature in the context of this work.

For this chapter, as done in Chap. 7, Sec. 7.5.2, let us consider a single, rigid test mass particle, such as an ion, orbiting stably in a futuristic storage ring.

8.2 Interactions with Residual Gas

Due to current limits of technology, there are limits to the maximum vacuum that can be obtained within the tubes of the storage ring where the ion orbits (see Sec. 5.1.1). Even for a futuristic ring, there may be theoretical upper limits on the level of vacuum attainable. Therefore, some residual air molecules would survive and interact with the circulating ions.

Such interactions may cause the ion to deviate from its ideal path, causing orbit distortions, which, as discussed in Sec. 7.10, would contribute negligibly as a noise on the timing measurement, as long as the amplitude of the distortion is small.

These interactions may also cause a perturbation in the tangential velocity of the ion, which would be a more significant contribution as a noise on the timing

measurement.

Although, it is obvious that the cross-section of such interactions would reduce not only for higher purity of vacuum, but also for a higher speed of the circulating ions, therefore indicating an advantage to using ultra-relativistic ions for an SRGO experiment.

8.3 Seismic Gravity Gradient Noise

In Chap. 6, Sec. 6.6, we discussed seismic noise and gravity gradient noise as two distinct and independent sources of noise. However, there is also a possiblity of a combined effect of the two.

Consider a scenario where a seismic wave impacts the geological region of an SRGO facility. The ion already experiences the effect of the vibrating magnets of the ring, and the effect of the local gravity gradient across the ring. However, some types of seismic waves, especially whose oscillations are perpendicular to the surface of the storage ring base, would effectively cause a bulge of Earth mass to oscillate across the mean location. This oscillating mass would, in turn, affect the local gravity gradient across the ring, introducing a 'seismic gravity gradient noise' on the timing measurement.

This noise would not be easy to estimate, and would require high fidelity numerical simulations, especially to obtain its frequency dependence.

However, as explored in Chap. 6, Sec. 6.6, unlike for an interferometric GW detector, the effect of any gravity gradient noise on a circulating test mass as within an SRGO, would act like 'a wind' on ΔT, that tends to cause a change which increases with time. Since gravity gradients are conservative, any change to the speed of the particle traveling across the gravity gradient in a circular path would be reverted to its original value after each revolution. However, the effect on the timing measurement, ΔT, would be affected permanently, causing a systematic noise.

For passive gravity gradients across the ring due to stationary objects such as the surrounding landscape, or even entirely predictable ones such as due to the Sun and the Moon, these may be easily modeled and subtracted from the measured data to eliminate their effect.

However, unpredictable gravity gradients, such as those due to seismic activity, would be harder to eliminate, and may require active sensors to monitor and accurately model the noise in real time, and then subtract it from the data.

Since gravity gradient noise cannot be screened, unlike pure seismic noise, the 'seismic gravity gradient noise' would not be attenuated even by installing vibration attenuating technology on the entire facility.

Chapter 9

Alternate Experimental Setups

As we have discussed in the previous chapters, the main application of the GW detection principle explored in this doctoral dissertation involves using storage rings, because it is already a well-known, pre-existing technology where charged particles act as test masses that can indeed perform uniform circular motion stably for long periods, and that are free along the circular tangential direction. These charged particle test masses can be controlled and monitored precisely, since storage rings are highly precise and sensitive setups. Further, the typically high rate of revolution acts favorably, not only to probe GWs over a wider frequency range, but to also reduce the impact of certain noise sources, and to cut down stochastic noise statistically by obtaining more data points over a given time period.

In this section, as the dissertation title suggests, we explore additional scenarios where we might find controllable test masses performing uniform circular motion that could be precisely monitored, and where the sources of noise would be minimal.

9.1 Artificial Satellites

At first glance, an artificial satellite orbiting in uniform circular motion around the Earth seems like an ideal experiment setup, since the satellite can easily be timed as it transmits signals back to Earth. Furthermore, since it is space-based, the sources of noise would be minimal. Collisions with debris and cosmic ray impacts, etc. could be negated by suspending a free test mass within an artificial vacuum created inside the satellite that has an outer shielding and thrusters for position correction.

However, upon further consideration, the real problem becomes apparent. The orbital frequency for a satellite would be comparable to the frequency of millihertz GWs. In case of storage rings, when the ion revolution frequency was much higher than the GW frequency, the ion could continuously 'accumulate' a timing deviation so long as the GW strain amplitude was monotonously increasing or decreasing, leading to a peak value that could be measured. In this case, the GW strain amplitude could change signs more than once during a single revolution of the satellite, which would greatly attenuate its ability to 'accumulate' a time difference. Hence, the pure signal would be weaker for such a setup due to a significantly lower orbital frequency compared to an SRGO.

One clear advantage that this setup has over storage rings, is that a satellite can orbit for much longer periods compared to ions in a storage ring. This suggests that such a setup would actually be better for probing GWs of frequencies lower than millihertz GWs. At such frequencies, the problem discussed in the previous paragraph is also resolved.

Qualitatively, we conclude that, compared to an SRGO, the noise levels in such a setup would be lower, but so would be the signal. Hence, an overall improvement to the SNR is not readily seen. Thus, this setup may not be as sensitive to millihertz GWs as an SRGO, although it may be more sensitive than an SRGO at lower frequencies.

Note that, for this experiment, the orientation of the satellite orbit relative to the GW source would be fixed, and the rotation of Earth would play no role in improving parameter estimation as it did for SRGO (discussed in Sec. 7.7). Using multiple satellites in differently oriented orbits would be required for improving the accuracy of parameter estimation.

Also note that a satellite is technically not confined along the radial direction, and small changes to its velocity may distort the orbit shape from the ideal circular orbit into an elliptical orbit, as is commonly known in astrodynamics. However, since the amplitude of these orbit distortions would be small, their effect on the timing deviation would be negligible, as mathematically proven in Sec. 7.10.

9.2 Levitating Superconductors

Consider a 'table-top' sized box, whose temperature is maintained to near absolute zero with high precision. The walls of the box are made of composite materials that are efficient at screening against external electromagnetic radiation, stray fields and stray particles. This box has a uniform and perfectly circular magnetic strip placed within. A small, solid test mass made of a uniform, superconducting material, in thermal equilibrium with the box, levitates atop the magnetic strip due to the Meissner effect [233]. An ultra-high vacuum is created inside the box. Upon giving the test mass a suitable impulse, it would perform uniform circular motion without any drag.

Assume also that this box is placed deep underground to reduce gravity gradient noise and other stray fields or particles. Assume further that the box is placed in an active vibration attenuator which reduces mechanical vibrations from seismic noise, etc. A thermal photon detector attached to an atomic/optical clock monitors the test mass without interfering with its motion.

Since the box is 'table-top' sized, thus the orbit radius is small, and the orbital frequency should be sufficiently large compared to the millihertz GW frequencies. The test mass could orbit stably for long periods, perhaps for weeks or even months.

This setup seems quite close to the ideal version envisioned for the GW detection

principle. However, such a setup is not as popular as a storage ring, and the sources of noise and other potential problems would have to be studied experimentally to make further comments. Some potential sources of noise are briefly explored below.

9.2.1 Stochastic Noise

Stochastic noise refers to random and unpredictable factors that induce jitters in the motion of the test mass.

- **Residual Gas Molecules:** Rare collisions with residual gas molecules in an ultra-high vacuum would impart unpredictable tiny forces, causing stochastic jitters.
- **Blackbody Radiation Interactions:** Comprising radiation pressure fluctuations and minor temperature changes post-photon absorption, this factor would induce random jitters in the ball's position.
- **Cosmic Rays and High-Energy Particles:** Random interactions with cosmic rays and similar particles would cause sporadic disturbances.
- **Detector Noise:** The stochastic effect of photon shot noise on the measurement and any other internal detector timing jitter.

9.2.2 Non-Stochastic Noise

Non-stochastic noise encompasses predictable, time-evolving, or transient influences on the motion of the test mass.

- **Mechanical Imperfections and Magnetic Field Fluctuations:** Imperfections in the magnetic strip and test mass, causing magnetic field fluctuations, would introduce forces that may evolve or have periodic effects.
- **External Vibrations:** Residual seismic vibrations or molecular vibrations within materials would contribute to time-evolving or transient forces.
- **Tidal Forces:** Predictable and periodic, tidal forces due to the Sun and the Moon would exert a calculable influence.

Chapter 10

Conclusion

From this doctoral dissertation, we conclude the following:

- In principle, a system consisting of test masses performing uniform circular motion which can be timed, is a novel detector of gravitational waves, as gravitational waves would cause a time-varying deviation of the measured test mass circulation times from those expected under no external disturbances.
- Such a detector, by its intrinsic detection principle and realistic limitations, would have maximum sensitivity to gravitational waves in the millihertz frequency range or lower, which are undetected at the time of writing this dissertation.
- Assuming a steady improvement in sensitivity leading to the first detections being made with a hypothetical future realisation of such a detector, the first sources to be detected would be supermassive binary black holes associated with the nearest galaxy mergers. These would be followed by the nearest mergers of supermassive black holes with intermediate mass black holes, likely at the centers of our galaxy and the nearest galaxies.
- A single such detector, taking advantage of Earth's rotation, and an assumed attenuation of noise sources, could perform accurate parameter estimation of the GW source, which is significant for follow-up studies in multi-messenger astronomy.
- Multiple such detectors at different locations on Earth, and in combination with space-based millihertz GW detectors, could achieve excellent parameter estimation capabilities.
- A circular particle accelerator, particularly, a storage ring, is one of the only pre-existing Earth-based technologies that comes closest to the ideal detector envisioned in principle. Other potential setups may offer even better sensitivities and parameter estimation capabilities, but have to be explored in-depth from scratch.
- A storage ring has various noise sources which would hide the GW signal that we wish to detect, and these noise sources must be studied in detail beyond the scope of this work, to be eliminated to the greatest possible extent.

- As long as there are no conclusive proofs that a futuristic facility as envisioned in this work, which we call SRGO, can never be achieved due to theoretical upper limits in technology or similar conclusive remarks, or as long as alternative systems to achieve the principle of the detector envisioned in this work cannot be conceived and tested, it is advisable to continue research in this novel direction.

Appendix A

Additional SRGO Response Plots

In this section, we show some more results like Fig. 7.1, without any noise, for some interesting configurations of the model parameters.

Fig. (A.1a), and Fig. (A.1b) show the SRGO response signal for an inspiraling supermassive binary black hole (SMBBH) with a GW frequency close to Earth's rotation frequency, at different initial GW phases. The order of magnitude of the signal, about $10^{-13}s$, is consistent with a $10^7 M_\odot$ equal mass SMBBH at $z = 0.1$, from Fig. (7.6).

Notably, the GW source has a declination of $90°$, thus the GW source is aligned with the Earth's axis, which means that the antenna pattern functions, F_+ and $F_\times$, are not time-evolving anymore due to Earth's rotation. Therefore, the SRGO response is, effectively, just a time-integral over the GW strain, making the response frequency equal to the GW frequency without any 'envelope', unlike other cases.

Interestingly, we see that for some initial GW phases, such as in Fig. (A.1a), once the signal begins from a value of zero (which is always true), after every GW period, the response never manages to return back to zero, since the GW frequency increases due to the inspiral of the binary and the amplitude of the response decreases. This means, eventually, the signal would die out at some finite, non-zero value, implying that after passing completely, the GW would leave a permanent deviation in the measured circulation times compared to the expected circulation times in the absence of GWs. This could be attributed as a homologue to the standard 'memory effect' of GWs [234] on a ring of test masses, with the difference being that the ring of test masses is circulating in our case.

Also, comparing Fig. (A.1a), and Fig. (A.1b), we notice that depending on the initial phase of the GW, the signal can obtain with time, both positive values and negative values. This implies that the test masses have the possibility to arrive both earlier or later than expected at the detector, depending on the scenario.

In Fig. (A.2a) and Fig. (A.2b), the GW source declination is equal to the latitude of the SRGO, allowing once per day, the GW to have a 'face-on' orientation to the plane of the storage ring, making the response null at those times. These times correspond to the flat regions observed in the responses. Further, since the GW frequency and Earth's rotation frequency are close, there is no clear 'outer envelope' and 'inner signal' that can be distinguished, unlike in Fig. (7.1), where there was a significant

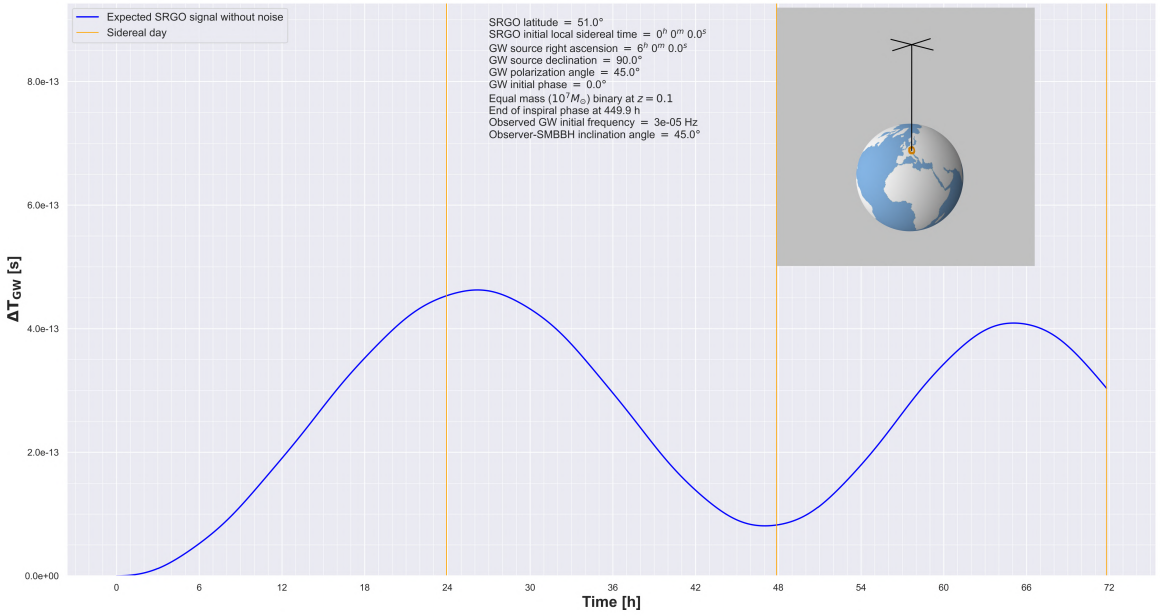

(a) Dec $= 90°$, $\delta = 0°$

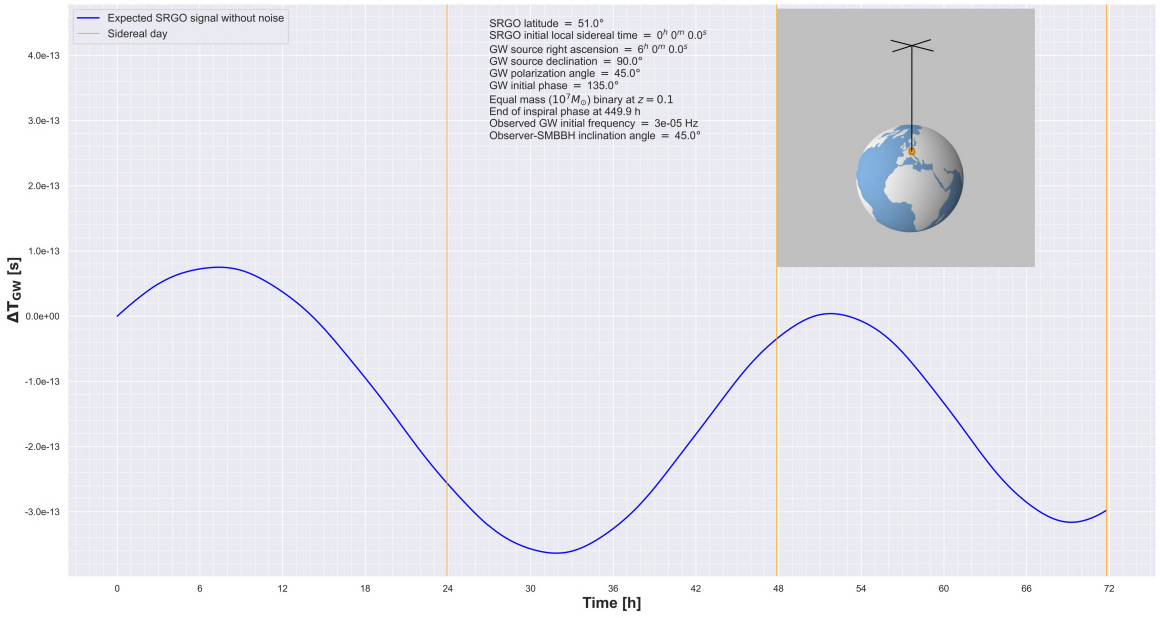

(b) Dec $= 90°$, $\delta = 135°$

Figure A.1: The SRGO response signals (without noise) corresponding to the parameters mentioned within the figures, with the difference between the left and right panels being that the initial phase of the GW is changing. Notably, both panels correspond to a GW source declination of $90°$, which is aligned with the Earth's axis.

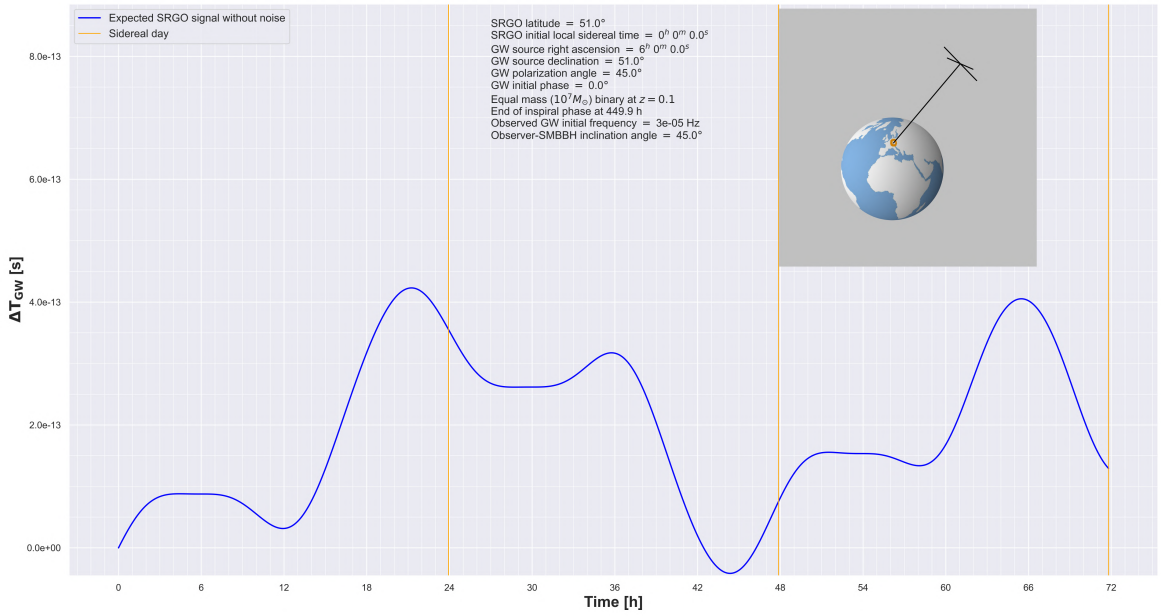

(a) Dec $= 51°$, $\delta = 0°$

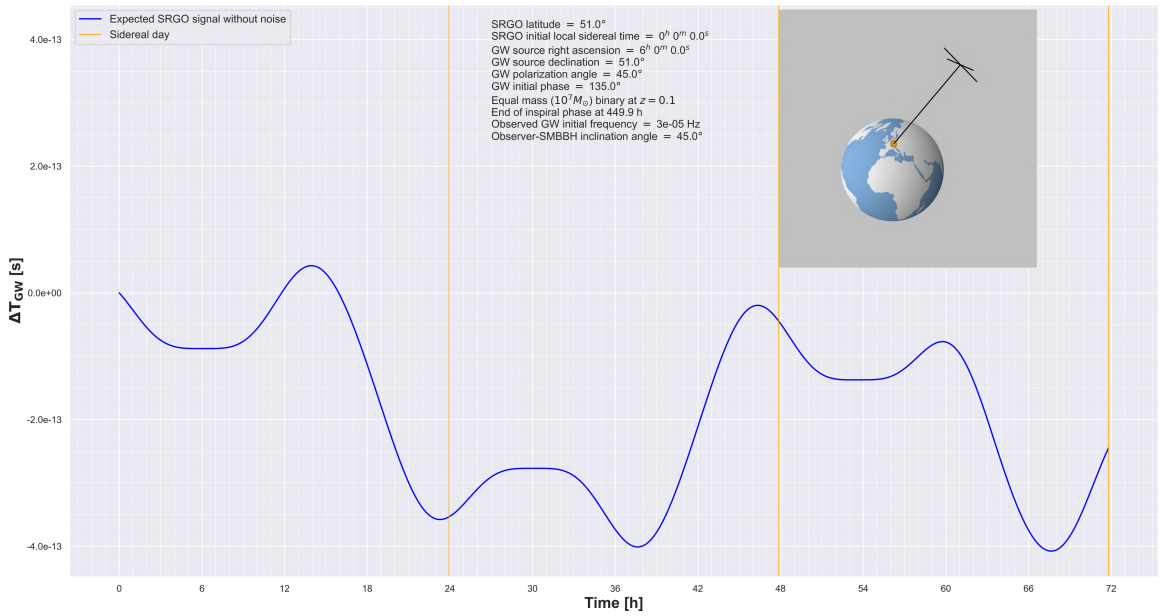

(b) Dec $= 51°$, $\delta = 135°$

Figure A.2: The SRGO response signals (without noise) corresponding to the parameters mentioned within the figures, with the difference between the left and right panels being that the initial phase of the GW is changing. Notably, both panels correspond to a GW source declination of $51°$, which is equal to the latitude of the storage ring.

difference between the two frequencies. The overall periodicity of the response is not clearly equal to either the GW or the Earth's frequency.

Appendix B

Conventional Approach to GW Sensitivity Curves

As briefly discussed in Chap. 7, Sec. 7.6.2, conventionally, a GW sensitivity curve plot contains two elements: First, colored regions are shown corresponding to various astrophysical GW sources. These regions are computed solely from GW strain models of the sources, and their extent is determined by astronomical constraints applied to the model parameters. Second, a curve is overplotted over these regions, which is constructed by modeling the experimentally measured detector noise data as a strain, using the response model of the GW detector. Since this plot is in the frequency space, which is integrated over all time, the ratio of a point in the colored region to a point on the curve, at a given frequency, directly gives the integrated signal-to-noise ratio at that frequency. This allows us to directly read off the signal-to-noise ratio by eye from such a plot. However, for computing the sensitivity curve, an averaging over the antenna pattern of the GW detector is involved. For LIGO and other high frequency GW detectors, the averaging of the antenna pattern is time-independent and trivial, because the antenna pattern is practically stationary over the duration of the GW. For millihertz GWs, which is our region of interest for an SRGO, the antenna pattern is not stationary due to Earth's rotation, making such an averaging time-dependent and difficult.

In this section, we analytically show what is meant by the above discussion. Let the time series of the measured data in an SRGO experiment be called ΔT_{data}. We can write

$$\Delta T_{data}(T) = \Delta T_{GW}(T) + \Delta T_{noise}(T). \tag{B.1}$$

The amplitude spectral density (ASD) of the noise is

$$ASD_{noise} = \lim_{T_{obs}\to\infty} \frac{|\Delta\tilde{T}_{noise}(f)|}{\sqrt{T_{obs}}} = \lim_{T_{obs}\to\infty} \frac{\frac{1}{2}\left(1-\frac{v_0^2}{2c^2}\right)\left|\mathcal{F}\left(\int_0^T h_n(t)dt\right)\right|}{\sqrt{T_{obs}}}, \tag{B.2}$$

where we have used the response of the detector, Eq. (7.4), to model the noise as a characteristic strain, $h_n = F_+ h_{n+} + F_\times h_{n\times}$. Now, we resolve the Fourier transform of the integral in the above equation using the unit step function, $u(t)$, and the convolution property of the Fourier transform,

$$\mathcal{F}\left(\int_0^T h_n(t)dt\right) = \mathcal{F}\left(\int_{-\infty}^{\infty} h_n(t)u(T-t)dt\right) = \mathcal{F}\left(h_n(T) \circledast u(T)\right) = \tilde{h}_n(f)\left(\frac{1}{if} + \pi\delta(f)\right). \tag{B.3}$$

For $f \neq 0$, the Dirac delta function vanishes. Substituting the result in the expression for ASD_{noise}, Eq. (B.2), we get,

$$ASD_{noise} = \lim_{T_{obs}\to\infty} \frac{\frac{1}{2}\left(1 - \frac{v_0^2}{2c^2}\right)|\tilde{h}_n(f)|}{f\sqrt{T_{obs}}}. \tag{B.4}$$

Comparing Eq. (B.2) and Eq. (B.4), we see that

$$ASD_{h_n} = \lim_{T_{obs}\to\infty} \frac{|\tilde{h}_n(f)|}{\sqrt{T_{obs}}} = \lim_{T_{obs}\to\infty} \frac{f.|\Delta\tilde{T}_{noise}(f)|}{\frac{1}{2}\left(1 - \frac{v_0^2}{2c^2}\right)\sqrt{T_{obs}}}. \tag{B.5}$$

Mathematically, in the definition of the ASD, the Fourier transform is a continuous-time Fourier transform. However, the experimentally measured noise data (in the absence of GWs), $\Delta T_{noise}(T)$, is a discrete time series, and we would therefore take a Discrete Fourier Transform (DFT) of it. We can use a relation between the DFT and continuous-time Fourier transform to correct the above formula, which becomes

$$ASD_{h_n} = \lim_{\substack{T_{obs}\to\infty \\ f_{sample}\to\infty}} \frac{f.|\Delta\tilde{T}_{noise}(f)|}{\frac{1}{2}\left(1 - \frac{v_0^2}{2c^2}\right) f_{sample}\sqrt{T_{obs}}}, \tag{B.6}$$

where the Fourier transform of the noise data, $\Delta\tilde{T}_{noise}(f)$, is now a DFT, and the factor f_{sample} is the data sampling rate.

However, this is not the final result that we need to plot the sensitivity curve. As mentioned earlier, $h_n = F_+ h_{n+} + F_\times h_{n\times}$, is the noise modeled as a characteristic strain. But we actually need the ASD of h_{n+} instead. This would be trivial to obtain from Eq. (B.6) by substituting the expression for the characteristic strain, then averaging over the stationary antenna pattern functions F_+ and $F_\times$ over all angles, and knowing that the Fourier transforms of h_{n+} and $h_{n\times}$ would be the same after averaging over other parameters.

However, for an SRGO, the antenna pattern functions are not stationary, and are functions of time due to Earth's rotation, making it difficult to obtain the desired result in the conventional way. Hence, we have used an alternate, semi-analytical way to derive and compute the GW sensitivity curve for an SRGO in Sec. 7.6.2.

Appendix C

Specifications of Computing Facilities

The simulation results shown in this dissertation were generated using the computing facilities of the Hamburg Observatory (Hamburger Sternwarte).

The Observatory's computing facilities include single-node workstations for serial and multithreaded applications. They are shared-memory systems with powerful multi-core processors for post-processing and data analysis. Some of them also operate as file servers.

The workstations used for the simulation results of this dissertation had Intel Xeon E5-2680 CPUs, with a total of 24 cores, and 252 GB memory.

Some of the results shown in this dissertation that involved averaging over several model parameters, such as Fig. (7.5), or that involved MCMC procedures applied to complex models, such as those shown in Sec. (7.11), took several days to a week to generate.

List of Figures

Bibliography

[1] B. P. Abbott, R. Abbott, T. D. Abbott, F. Acernese, K. Ackley, C. Adams, T. Adams, P. Addesso, R. X. Adhikari, and V. B. Adya *et al.* Tests of general relativity with gw170817. *Phys. Rev. Lett.*, 123:011102, Jul 2019.

[2] The LIGO Scientific Collaboration, the Virgo Collaboration, the KAGRA Collaboration, R. Abbott, H. Abe, F. Acernese, K. Ackley, N. Adhikari, R. X. Adhikari, and V. K. Adkins *et al.* Tests of general relativity with gwtc-3, 2021.

[3] B. P. Abbott, R. Abbott, T. D. Abbott, F. Acernese, K. Ackley, C. Adams, T. Adams, P. Addesso, R. X. Adhikari, and V. B. Adya *et al.* On the progenitor of binary neutron star merger gw170817. *The Astrophysical Journal Letters*, 850(2):L40, dec 2017.

[4] R. Abbott, T. D. Abbott, S. Abraham, F. Acernese, K. Ackley, C. Adams, R. X. Adhikari, V. B. Adya, C. Affeldt, and M. Agathos *et al.* Gw190521: A binary black hole merger with a total mass of $150\ M_{\odot}$. *Phys. Rev. Lett.*, 125:101102, Sep 2020.

[5] R. Abbott, H. Abe, F. Acernese, K. Ackley, N. Adhikari, R. X. Adhikari, V. K. Adkins, V. B. Adya, C. Affeldt, and D. Agarwal *et al.* Constraints on the cosmic expansion history from gwtc–3. *The Astrophysical Journal*, 949(2):76, jun 2023.

[6] M. M. Kasliwal, E. Nakar, L. P. Singer, D. L. Kaplan, D. O. Cook, A. Van Sistine, R. M. Lau, C. Fremling, O. Gottlieb, J. E. Jencson, S. M. Adams, U. Feindt, K. Hotokezaka, S. Ghosh, D. A. Perley, P.-C. Yu, T. Piran, J. R. Allison, G. C. Anupama, A. Balasubramanian, K. W. Bannister, J. Bally, J. Barnes, S. Barway, E. Bellm, V. Bhalerao, D. Bhattacharya, N. Blagorodnova, J. S. Bloom, P. R. Brady, C. Cannella, D. Chatterjee, S. B. Cenko, B. E. Cobb, C. Copperwheat, A. Corsi, K. De, D. Dobie, S. W. K. Emery, P. A. Evans, O. D. Fox, D. A. Frail, C. Frohmaier, A. Goobar, G. Hallinan, F. Harrison, G. Helou, T. Hinderer, A. Y. Q. Ho, A. Horesh, W.-H. Ip, R. Itoh, D. Kasen, H. Kim, N. P. M. Kuin, T. Kupfer, C. Lynch, K. Madsen, P. A. Mazzali, A. A. Miller, K. Mooley, T. Murphy, C.-C. Ngeow, D. Nichols, S. Nissanke, P. Nugent, E. O. Ofek, H. Qi, R. M. Quimby, S. Rosswog, F. Rusu, E. M. Sadler, P. Schmidt, J. Sollerman, I. Steele, A. R. Williamson, Y. Xu, L. Yan, Y. Yatsu, C. Zhang, and W. Zhao. Illuminating gravitational waves: A concordant picture of photons from a neutron star merger. *Science*, 358(6370):1559–1565, 2017.

[7] Darach Watson, Camilla J. Hansen, Jonatan Selsing, Andreas Koch, Daniele B. Malesani, Anja C. Andersen, Johan P. U. Fynbo, Almudena Arcones, Andreas Bauswein, Stefano Covino, Aniello Grado, Kasper E. Heintz, Leslie Hunt, Chryssa Kouveliotou, Giorgos Leloudas, Andrew J. Levan, Paolo Mazzali, and

Elena Pian. Identification of strontium in the merger of two neutron stars. *Nature*, 574(7779):497–500, Oct 2019.

[8] Mansi M Kasliwal, Daniel Kasen, Ryan M Lau, Daniel A Perley, Stephan Rosswog, Eran O Ofek, Kenta Hotokezaka, Ranga-Ram Chary, Jesper Sollerman, Ariel Goobar, and David L Kaplan. Spitzer mid-infrared detections of neutron star merger GW170817 suggests synthesis of the heaviest elements. *Monthly Notices of the Royal Astronomical Society: Letters*, 510(1):L7–L12, 01 2019.

[9] B. P. Abbott, R. Abbott, T. D. Abbott, F. Acernese, K. Ackley, C. Adams, T. Adams, P. Addesso, R. X. Adhikari, and V. B. Adya *et al.* A gravitational-wave standard siren measurement of the hubble constant. *Nature*, 551(7678):85–88, Nov 2017.

[10] B. P. Abbott *et al.*, LIGO Scientific Collaboration, and Virgo Collaboration. Observation of gravitational waves from a binary black hole merger. *Physical Review Letters*, 116(6):061102, Feb 2016.

[11] B. P. Abbott et al. Gw170817: Observation of gravitational waves from a binary neutron star inspiral. *Physical Review Letters*, 119(16):161101, 2017.

[12] B. P. Abbott, R. Abbott, T. D. Abbott, F. Acernese, K. Ackley, C. Adams, T. Adams, P. Addesso, R. X. Adhikari, and V. B. Adya *et al.* Multi-messenger observations of a binary neutron star merger*. *The Astrophysical Journal Letters*, 848(2):L12, oct 2017.

[13] B. P. Abbott, R. Abbott, T. D. Abbott, F. Acernese, K. Ackley, C. Adams, T. Adams, P. Addesso, R. X. Adhikari, and V. B. Adya *et al.* Gravitational waves and gamma-rays from a binary neutron star merger: Gw170817 and grb 170817a. *The Astrophysical Journal Letters*, 848(2):L13, oct 2017.

[14] Geoffrey Mo, Rahul Jayaraman, Danielle Frostig, Michael M. Fausnaugh, Erik Katsavounidis, and George R. Ricker. Multi-messenger astrophysics in the gravitational-wave era, 2023.

[15] B. P. Abbott, R. Abbott, T. D. Abbott, S. Abraham, F. Acernese, K. Ackley, C. Adams, R. X. Adhikari, V. B. Adya, and C. Affeldt *et al.* Low-latency gravitational-wave alerts for multimessenger astronomy during the second advanced ligo and virgo observing run. *The Astrophysical Journal*, 875(2):161, apr 2019.

[16] A. Gunny, D. Rankin, J. Krupa, et al. Hardware-accelerated inference for real-time gravitational-wave astronomy. *Nature Astronomy*, 6:529–536, 2022.

[17] A. L. Miller et al. Enabling multi-messenger astronomy with continuous gravitational waves: early warning and sky localization of binary neutron stars in einstein telescope. *arXiv*, 2023.

[18] B. P. Abbott *et al.*, LIGO Scientific Collaboration, and Virgo Collaboration. Ligo: the laser interferometer gravitational-wave observatory. *Reports on Progress in Physics*, 72(7):076901, Jun 2009.

[19] T Accadia, F Acernese, M Alshourbagy, P Amico, F Antonucci, S Aoudia, N Arnaud, C Arnault, K G Arun, and P Astone *et al.* Virgo: a laser interferometer to detect gravitational waves. *Journal of Instrumentation*, 7(03):P03012, mar 2012.

[20] T. Akutsu, M. Ando, K. Arai, Y. Arai, S. Araki, A. Araya, N. Aritomi, H. Asada, Y. Aso, and S. Atsuta *et al.* Kagra: 2.5 generation interferometric gravitational wave detector. *Nature Astronomy*, 3(1):35–40, Jan 2019.

[21] B P Abbott, R Abbott, T D Abbott, M R Abernathy, K Ackley, C Adams, P Addesso, R X Adhikari, V B Adya, and C Affeldt *et al.* Exploring the sensitivity of next generation gravitational wave detectors. *Classical and Quantum Gravity*, 34(4):044001, jan 2017.

[22] Stefano Bagnasco. The ligo-virgo-kagra computing infrastructure for gravitational-wave research, 2023.

[23] R. Abbott, T. D. Abbott, F. Acernese, K. Ackley, C. Adams, N. Adhikari, R. X. Adhikari, V. B. Adya, C. Affeldt, and D. Agarwal *et al.* Gwtc-3: Compact binary coalescences observed by ligo and virgo during the second part of the third observing run. *Phys. Rev. X*, 13:041039, Dec 2023.

[24] R. Abbott, T. D. Abbott, F. Acernese, K. Ackley, C. Adams, N. Adhikari, R. X. Adhikari, V. B. Adya, C. Affeldt, and D. Agarwal *et al.* Population of merging compact binaries inferred using gravitational waves through gwtc-3. *Phys. Rev. X*, 13:011048, Mar 2023.

[25] Pia Jakobus, Bernhard Müller, Alexander Heger, Shuai Zha, Jade Powell, Anton Motornenko, Jan Steinheimer, and Horst Stöcker. Gravitational waves from a core g mode in supernovae as probes of the high-density equation of state. *Phys. Rev. Lett.*, 131:191201, Nov 2023.

[26] Lorenzo Speri, Andrea Antonelli, Laura Sberna, Stanislav Babak, Enrico Barausse, Jonathan R. Gair, and Michael L. Katz. Probing accretion physics with gravitational waves. *Phys. Rev. X*, 13:021035, Jun 2023.

[27] B. Haskell and M. Bejger. Astrophysics with continuous gravitational waves. *Nature Astronomy*, 7(10):1160–1170, Oct 2023.

[28] Pau Amaro-Seoane *et al.* Laser Interferometer Space Antenna. *arXiv e-prints*, page arXiv:1702.00786, February 2017.

[29] Aniello Grado. Einstein telescope, the future generation of ground based gravitational wave detectors. *Journal of Physics: Conference Series*, 2429(1):012041, feb 2023.

[30] Matthew Evans, Rana X Adhikari, Chaitanya Afle, Stefan W. Ballmer, Sylvia Biscoveanu, Ssohrab Borhanian, Duncan A. Brown, Yanbei Chen, Robert Eisenstein, Alexandra Gruson, Anuradha Gupta, Evan D. Hall, Rachael Huxford, Brittany Kamai, Rahul Kashyap, Jeff S. Kissel, Kevin Kuns, Philippe Landry, Amber Lenon, Geoffrey Lovelace, Lee McCuller, Ken K. Y. Ng, Alexander H.

Nitz, Jocelyn Read, B. S. Sathyaprakash, David H. Shoemaker, Bram J. J. Slagmolen, Joshua R. Smith, Varun Srivastava, Ling Sun, Salvatore Vitale, and Rainer Weiss. A horizon study for cosmic explorer: Science, observatories, and community, 2021.

[31] Gabriella Agazie, Akash Anumarlapudi, Anne M. Archibald, Zaven Arzoumanian, Paul T. Baker, Bence Bécsy, Laura Blecha, Adam Brazier, Paul R. Brook, and Sarah Burke-Spolaor *et al.* The nanograv 15 yr data set: Evidence for a gravitational-wave background. *The Astrophysical Journal Letters*, 951(1):L8, jun 2023.

[32] Adeela Afzal, Gabriella Agazie, Akash Anumarlapudi, Anne M. Archibald, Zaven Arzoumanian, Paul T. Baker, Bence Bécsy, Jose Juan Blanco-Pillado, Laura Blecha, and Kimberly K. Boddy *et al.* The nanograv 15 yr data set: Search for signals from new physics. *The Astrophysical Journal Letters*, 951(1):L11, jun 2023.

[33] M. Bailes, B. K. Berger, P. R. Brady, M. Branchesi, K. Danzmann, M. Evans, K. Holley-Bockelmann, B. R. Iyer, T. Kajita, S. Katsanevas, M. Kramer, A. Lazzarini, L. Lehner, G. Losurdo, H. Lück, D. E. McClelland, M. A. McLaughlin, M. Punturo, S. Ransom, S. Raychaudhury, D. H. Reitze, F. Ricci, S. Rowan, Y. Saito, G. H. Sanders, B. S. Sathyaprakash, B. F. Schutz, A. Sesana, H. Shinkai, X. Siemens, D. H. Shoemaker, J. Thorpe, J. F. J. van den Brand, and S. Vitale. Gravitational-wave physics and astronomy in the 2020s and 2030s. *Nature Reviews Physics*, 3(5):344–366, May 2021.

[34] Nigel T. Bishop. *Introduction to Gravitational Wave Astronomy*, pages 1–31. Springer Singapore, Singapore, 2020.

[35] Albert Einstein. Die grundlage der allgemeinen relativitätstheorie. *Annalen der Physik*, 354(7):769–822, 1916.

[36] Daniel Kennefick. *Traveling at the Speed of Thought: Einstein and the Quest for Gravitational Waves*. Princeton University Press, 2007.

[37] Russell A Hulse and Joseph H Taylor. Discovery of a pulsar in a binary system. *The Astrophysical Journal*, 195:L51–L53, 1975.

[38] B. P. Abbott et al. Observation of gravitational waves from a binary black hole merger. *Physical Review Letters*, 116(6):061102, 2016.

[39] F. Acernese et al. Advanced virgo: a second-generation interferometric gravitational wave detector. *Classical and Quantum Gravity*, 32(2):024001, 2015.

[40] Denis V Martynov et al. Gw150914: The advanced ligo detectors in the era of first discoveries. *Physical Review Letters*, 116(13):131103, 2016.

[41] B. P. Abbott et al. Gwtc-1: A gravitational-wave transient catalog of compact binary mergers observed by ligo and virgo during the first and second observing runs. *Physical Review X*, 9(3):031040, 2019.

[42] Pau Amaro-Seoane et al. Laser interferometer space antenna. *arXiv preprint arXiv:1702.00786*, 2020.

[43] Alexandre Le Tiec and Jérôme Novak. *Theory of Gravitational Waves*, chapter Chapter 1, pages 1–41.

[44] T. Futamase and Y. Itoh. *The Post-Newtonian Approximation for Relativistic Compact Binaries*. Cambridge University Press, 2007.

[45] Luc Blanchet. Gravitational radiation from post-newtonian sources and inspiralling compact binaries. *Living Reviews in Relativity*, 17(1):2, 2014.

[46] Frans Pretorius. Evolution of binary black-hole spacetimes. *Physical Review Letters*, 95(12):121101, 2005.

[47] Joan Centrella, John G. Baker, Bernard J. Kelly, and James R. van Meter. Black-hole binaries, gravitational waves, and numerical relativity. *Reviews of Modern Physics*, 82(4):3069, 2010.

[48] Kostas D. Kokkotas and Bernd G. Schmidt. Quasinormal modes of stars and black holes. *Living Reviews in Relativity*, 2(1):2, 1999.

[49] Emanuele Berti, Vitor Cardoso, and Andrei O. Starinets. Quasinormal modes of black holes and black branes. *Classical and Quantum Gravity*, 26(16):163001, 2009.

[50] A. Buonanno and T. Damour. Effective one-body approach to general relativistic two-body dynamics. *Physical Review D*, 59(8):084006, 1999.

[51] Yi Pan, Alessandra Buonanno, Michael Boyle, Luisa T. Buchman, Lawrence E. Kidder, Harald P. Pfeiffer, and Mark A. Scheel. Inspiral-merger-ringdown waveforms for black-hole binaries with nonprecessing spins. *Physical Review D*, 84(12):124052, 2011.

[52] P. Ajith et al. Inspiral-merger-ringdown waveforms for black-hole binaries with non-precessing spins. *Physical Review Letters*, 106(24):241101, 2011.

[53] Pau Amaro-Seoane, Jonathan R. Gair, Marc Freitag, M. Coleman Miller, Ilya Mandel, Curt J. Cutler, and Stanislav Babak. Intermediate and extreme mass-ratio inspirals—astrophysics, science applications and detection using lisa. *Classical and Quantum Gravity*, 24(17):R113, 2007.

[54] Jonathan R. Gair, Leor Barack, Teviet Creighton, Curt Cutler, Shane L. Larson, E. Sterl Phinney, and Michele Vallisneri. Event rate estimates for lisa extreme mass ratio capture sources. *Classical and Quantum Gravity*, 21(20):S1595, 2004.

[55] Ezra Newman and Roger Penrose. An approach to gravitational radiation by a method of spin coefficients. *Journal of Mathematical Physics*, 3(3):566–578, 1962.

[56] J. N. Goldberg, A. J. Macfarlane, E. T. Newman, F. Rohrlich, and E. C. G. Sudarshan. Spin-s spherical harmonics and ð. *Journal of Mathematical Physics*, 8(11):2155–2161, 1967.

[57] Ernazar Abdikamalov, Giulia Pagliaroli, and David Radice. *Gravitational Waves from Core-Collapse Supernovae*, pages 1–37. Springer Singapore, Singapore, 2020.

[58] John Baker *et al.* The Laser Interferometer Space Antenna: Unveiling the Millihertz Gravitational Wave Sky. *arXiv e-prints*, page arXiv:1907.06482, July 2019.

[59] Stefano Bondani, Francesco Haardt, Alberto Sesana, Enrico Barausse, and Massimo Dotti. Detectability of gravitational waves from primordial black holes orbiting sgr A^*. *Phys. Rev. D*, 106:043015, Aug 2022.

[60] Bernard J. Kelly, John G. Baker, Zachariah B. Etienne, Bruno Giacomazzo, and Jeremy Schnittman. Prompt electromagnetic transients from binary black hole mergers. *Phys. Rev. D*, 96:123003, Dec 2017.

[61] M. J. Graham, K. E. S. Ford, B. McKernan, N. P. Ross, D. Stern, K. Burdge, M. Coughlin, S. G. Djorgovski, A. J. Drake, D. Duev, M. Kasliwal, A. A. Mahabal, S. van Velzen, J. Belecki, E. C. Bellm, R. Burruss, S. B. Cenko, V. Cunningham, G. Helou, S. R. Kulkarni, F. J. Masci, T. Prince, D. Reiley, H. Rodriguez, B. Rusholme, R. M. Smith, and M. T. Soumagnac. Candidate electromagnetic counterpart to the binary black hole merger gravitational-wave event s190521g. *Phys. Rev. Lett.*, 124:251102, Jun 2020.

[62] Tomas Tamfal, Pedro R. Capelo, Stelios Kazantzidis, Lucio Mayer, Douglas Potter, Joachim Stadel, and Lawrence M. Widrow. Formation of LISA black hole binaries in merging dwarf galaxies: The imprint of dark matter. *The Astrophysical Journal*, 864(1):L19, aug 2018.

[63] Emma Jane Weller, Fabio Pacucci, Lars Hernquist, and Sownak Bose. Dynamics of intermediate-mass black holes wandering in the milky way galaxy using the illustris TNG50 simulation. *Monthly Notices of the Royal Astronomical Society*, 511(2):2229–2238, 01 2022.

[64] Giacomo Fragione, Idan Ginsburg, and Bence Kocsis. Gravitational waves and intermediate-mass black hole retention in globular clusters. *The Astrophysical Journal*, 856(2):92, mar 2018.

[65] Giacomo Fragione, Nathan W. C. Leigh, Idan Ginsburg, and Bence Kocsis. Tidal disruption events and gravitational waves from intermediate-mass black holes in evolving globular clusters across space and time. *The Astrophysical Journal*, 867(2):119, nov 2018.

[66] Monica Colpi, Kelly Holley-Bockelmann, Tamara Bogdanovic, Priya Natarajan, Jillian Bellovary, Alberto Sesana, Michael Tremmel, Jeremy Schnittman, Julia Comerford, and Enrico Barausse *et al.* Astro2020 science white paper: The gravitational wave view of massive black holes, 2019.

[67] J Antoniadis, Z Arzoumanian, S Babak, M Bailes, A-S Bak Nielsen, P T Baker, C G Bassa, B Bécsy, A Berthereau, and M Bonetti *et al.* The International Pulsar Timing Array second data release: Search for an isotropic gravitational wave

background. *Monthly Notices of the Royal Astronomical Society*, 510(4):4873–4887, 01 2022.

[68] Francois Foucart. A brief overview of black hole-neutron star mergers. *Frontiers in Astronomy and Space Sciences*, 7, 2020.

[69] C. Barbieri, O. S. Salafia, A. Perego, M. Colpi, and G. Ghirlanda. Electromagnetic counterparts of black hole–neutron star mergers: dependence on the neutron star properties. *The European Physical Journal A*, 56(1):8, Jan 2020.

[70] David Falta, Robert Fisher, and Gaurav Khanna. Gravitational wave emission from the single-degenerate channel of type ia supernovae. *Phys. Rev. Lett.*, 106:201103, May 2011.

[71] Ivo R. Seitenzahl, Matthias Herzog, Ashley J. Ruiter, Kai Marquardt, Sebastian T. Ohlmann, and Friedrich K. Röpke. Neutrino and gravitational wave signal of a delayed-detonation model of type ia supernovae. *Phys. Rev. D*, 92:124013, Dec 2015.

[72] Tomoya Kinugawa, Hiroki Takeda, Ataru Tanikawa, and Hiroya Yamaguchi. Probe for type ia supernova progenitor in decihertz gravitational wave astronomy. *The Astrophysical Journal*, 938(1):52, oct 2022.

[73] Maselli, A., Marassi, S., and Branchesi, M. Binary white dwarfs and decihertz gravitational wave observations: From the hubble constant to supernova astrophysics. *AA*, 635:A120, 2020.

[74] Rui-Nan Li, Zhen-Yin Zhao, Zhifu Gao, and Fa-Yin Wang. Fast radio bursts: Electromagnetic counterparts to extreme mass-ratio inspirals. *The Astrophysical Journal Letters*, 956(1):L2, oct 2023.

[75] Chang-Qing Ye, Hui-Min Fan, Alejandro Torres-Orjuela, Jian dong Zhang, and Yi-Ming Hu. Identification of gravitational-waves from extreme mass ratio inspirals, 2023.

[76] Ritam Mallick, Shailendra Singh, and Prasad R. Gravitational wave signature from phase transition of a combusting neutron star to quark star. *Monthly Notices of the Royal Astronomical Society*, 507(1):1318–1328, 08 2021.

[77] The LIGO Scientific Collaboration, the Virgo Collaboration, the KAGRA Collaboration, R. Abbott, H. Abe, F. Acernese, K. Ackley, N. Adhikari, R. X. Adhikari, V. K. Adkins, V. B. Adya, C. Affeldt, and D. Agarwal *et al.* Search for gravitational-wave transients associated with magnetar bursts in advanced ligo and advanced virgo data from the third observing run, 2022.

[78] Karl Wette. Searches for continuous gravitational waves from neutron stars: A twenty-year retrospective. *Astroparticle Physics*, 153:102880, 2023.

[79] R. Abbott, H. Abe, F. Acernese, K. Ackley, N. Adhikari, R. X. Adhikari, V. K. Adkins, V. B. Adya, C. Affeldt, and D. Agarwal *et al.* All-sky search for continuous gravitational waves from isolated neutron stars using advanced ligo and advanced virgo o3 data. *Phys. Rev. D*, 106:102008, Nov 2022.

[80] B. P. Abbott, R. Abbott, T. D. Abbott, M. R. Abernathy, F. Acernese, K. Ackley, C. Adams, T. Adams, P. Addesso, and R. X. Adhikari *et al.* Search for continuous gravitational waves from neutron stars in globular cluster ngc 6544. *Phys. Rev. D*, 95:082005, Apr 2017.

[81] Paul D. Lasky. Gravitational waves from neutron stars: A review. *Publications of the Astronomical Society of Australia*, 32:e034, 2015.

[82] Pedro H B Rossetto, Jörg Frauendiener, Ryan Brunet, and Andrew Melatos. Magnetically confined mountains on accreting neutron stars in general relativity. *Monthly Notices of the Royal Astronomical Society*, 526(2):2058–2066, 09 2023.

[83] P. B. Covas, M. A. Papa, R. Prix, and B. J. Owen. Constraints on r-modes and mountains on millisecond neutron stars in binary systems. *The Astrophysical Journal Letters*, 929(2):L19, apr 2022.

[84] Chiara Caprini and Daniel G Figueroa. Cosmological backgrounds of gravitational waves. *Classical and Quantum Gravity*, 35(16):163001, jul 2018.

[85] Nelson Christensen. Stochastic gravitational wave backgrounds. *Reports on Progress in Physics*, 82(1):016903, nov 2018.

[86] Arianna I. Renzini, Boris Goncharov, Alexander C. Jenkins, and Patrick M. Meyers. Stochastic gravitational-wave backgrounds: Current detection efforts and future prospects. *Galaxies*, 10(1), 2022.

[87] Valerie Domcke and Camilo Garcia-Cely. Potential of radio telescopes as high-frequency gravitational wave detectors. *Phys. Rev. Lett.*, 126:021104, Jan 2021.

[88] Paul D. Lasky, Chiara M. F. Mingarelli, Tristan L. Smith, John T. Giblin, Eric Thrane, Daniel J. Reardon, Robert Caldwell, Matthew Bailes, N. D. Ramesh Bhat, Sarah Burke-Spolaor, Shi Dai, James Dempsey, George Hobbs, Matthew Kerr, Yuri Levin, Richard N. Manchester, Stefan Osłowski, Vikram Ravi, Pablo A. Rosado, Ryan M. Shannon, Renée Spiewak, Willem van Straten, Lawrence Toomey, Jingbo Wang, Linqing Wen, Xiaopeng You, and Xingjiang Zhu. Gravitational-wave cosmology across 29 decades in frequency. *Phys. Rev. X*, 6:011035, Mar 2016.

[89] Anupam Mazumdar and Graham White. Review of cosmic phase transitions: their significance and experimental signatures. *Reports on Progress in Physics*, 82(7):076901, jun 2019.

[90] Yanou Cui and Evangelos I. Sfakianakis. Detectable gravitational wave signals from inflationary preheating. *Physics Letters B*, 840:137825, 2023.

[91] Md Riajul Haque, Debaprasad Maity, Tanmoy Paul, and L. Sriramkumar. Decoding the phases of early and late time reheating through imprints on primordial gravitational waves. *Phys. Rev. D*, 104:063513, Sep 2021.

[92] David I. Dunsky, Anish Ghoshal, Hitoshi Murayama, Yuki Sakakihara, and Graham White. Guts, hybrid topological defects, and gravitational waves. *Phys. Rev. D*, 106:075030, Oct 2022.

[93] Wilfried Buchmüller, Valerie Domcke, and Kai Schmitz. Stochastic gravitational-wave background from metastable cosmic strings. *Journal of Cosmology and Astroparticle Physics*, 2021(12):006, dec 2021.

[94] Kazunori Nakayama, Fuminobu Takahashi, and Norimi Yokozaki. Gravitational waves from domain walls and their implications. *Physics Letters B*, 770:500–506, 2017.

[95] Carmelita Carbone, Carlo Baccigalupi, and Sabino Matarrese. Stochastic gravitational wave background from cold dark matter halos. *Phys. Rev. D*, 73:063503, Mar 2006.

[96] Anish Ghoshal and Alessandro Strumia. Probing the dark matter density with gravitational waves from super-massive binary black holes, 2023.

[97] Otto A. Hannuksela, Kaze W. K. Wong, Richard Brito, Emanuele Berti, and Tjonnie G. F. Li. Probing the existence of ultralight bosons with a single gravitational-wave measurement. *Nature Astronomy*, 3(5):447–451, May 2019.

[98] Gabriele Franciolini, Antonio Junior Iovino, Ville Vaskonen, and Hardi Veermäe. Recent gravitational wave observation by pulsar timing arrays and primordial black holes: The importance of non-gaussianities. *Phys. Rev. Lett.*, 131:201401, Nov 2023.

[99] C J Moore, R H Cole, and C P L Berry. Gravitational-wave sensitivity curves. *Classical and Quantum Gravity*, 32(1):015014, dec 2014.

[100] P. Astone, M. Bassan, P. Bonifazi, P. Carelli, M. G. Castellano, G. Cavallari, E. Coccia, C. Cosmelli, V. Fafone, S. Frasca, E. Majorana, I. Modena, G. V. Pallottino, G. Pizzella, P. Rapagnani, F. Ricci, and M. Visco. Long-term operation of the rome "explorer" cryogenic gravitational wave detector. *Physical Review D*, 47(362), 1993.

[101] Adele La Rana and Leopoldo Milano. The early history of gravitational wave detection in italy: from the first resonant bars to the beginning of the virgo collaboration. *Conference Paper at XXXVI Convegno annuale della SISFA*, 2017.

[102] P. Astone, M. Bassan, P. Bonifazi, P. Carelli, E. Coccia, V. Fafone, S. Frasca, Y. Minenkov, I. Modena, P. Modestino, A. Moleti, G. V. Pallottino, G. Pizzella,

R. Terenzi, and M. Visco. Upper limit at 1.8 kHz for a gravitational-wave stochastic background with the it ALTAIR resonant-mass detector. , 343:19–22, March 1999.

[103] P. Astone, M. Bassan, P. Bonifazi, P. Carelli, E. Coccia, C. Cosmelli, V. Fafone, S. Frasca, K. Geng, W. O. Hamilton, W. W. Johnson, E. Mauceli, M. P. McHugh, S. Merkowitz, I. Modena, G. Modestino, A. Morse, G. V. Pallottino, M. A. Papa, G. Pizzella, N. Solomonson, R. Terenzi, M. Visco, and N. Zhu. Search for gravitational radiation with the allegro and explorer detectors. *Phys. Rev. D*, 59:122001, May 1999.

[104] Carlos Frajuca and Fabio Da Silva Bortoli. Limitation of Gravitational Wave Detector Niobè Sensitivity by the Frequency Tracking Noise. In *International Journal of Modern Physics Conference Series*, volume 45 of *International Journal of Modern Physics Conference Series*, page 1760017, January 2017.

[105] P. Astone, M. Bassan, E. Coccia, S. D'Antonio, V. Fafone, G. Giordano, A. Marini, Y. Minenkov, I. Modena, and A. Moleti *et al.* Analysis of 3 years of data from the gravitational wave detectors EXPLORER and NAUTILUS. *Phys. Rev. D*, 87:082002, Apr 2013.

[106] J-P Zendri, L Baggio, M Bignotto, M Bonaldi, M Cerdonio, L Conti, M De Rosa, P Falferi, P L Fortini, M Inguscio, A Marin, F Marin, R Mezzena, A Ortolan, G A Prodi, E Rocco, F Salemi, G Soranzo, L Taffarello, G Vedovato, A Vinante, and S Vitale. Status report and near future prospects for the gravitational wave detector auriga. *Classical and Quantum Gravity*, 19(7):1925, mar 2002.

[107] V. Liccardo, C. H. Lenzi, R. M. Marinho, O. D. Aguiar, C. Frajuca, F. da Silva Bortoli, and C. A. Costa. The design strain sensitivity of the schenberg spherical resonant antenna for gravitational waves. *Scientific Reports*, 13(1):17706, Oct 2023.

[108] L. Gottardi, A. de Waard, O. Usenko, G. Frossati, M. Podt, J. Flokstra, M. Bassan, V. Fafone, Y. Minenkov, and A. Rocchi. Sensitivity of the spherical gravitational wave detector minigrail operating at 5 k. *Phys. Rev. D*, 76:102005, Nov 2007.

[109] Masaki Ando, Koji Arai, Ryutaro Takahashi, Gerhard Heinzel, Seiji Kawamura, Daisuke Tatsumi, Nobuyuki Kanda, Hideyuki Tagoshi, Akito Araya, and Hideki Asada *et al.* Stable operation of a 300-m laser interferometer with sufficient sensitivity to detect gravitational-wave events within our galaxy. *Phys. Rev. Lett.*, 86:3950–3954, Apr 2001.

[110] J. Abadie, B. P. Abbott, R. Abbott, T. D. Abbott, M. Abernathy, C. Adams, R. Adhikari, C. Affeldt, B. Allen, and G. S. Allen *et al.* A gravitational wave observatory operating beyond the quantum shot-noise limit. *Nature Physics*, 7(12):962–965, Dec 2011.

[111] James Lough, Emil Schreiber, Fabio Bergamin, Hartmut Grote, Moritz Mehmet, Henning Vahlbruch, Christoph Affeldt, Marc Brinkmann, Aparna Bisht, Volker

Kringel, Harald Lück, Nikhil Mukund, Severin Nadji, Borja Sorazu, Kenneth Strain, Michael Weinert, and Karsten Danzmann. First demonstration of 6 db quantum noise reduction in a kilometer scale gravitational wave observatory. *Phys. Rev. Lett.*, 126:041102, Jan 2021.

[112] S Miyoki, T Uchiyama, K Yamamoto, H Hayakawa, K Kasahara, H Ishitsuka, M Ohashi, K Kuroda, D Tatsumi, S Telada, M Ando, T Tomaru, T Suzuki, N Sato, T Haruyama, Y Higashi, Y Saito, A Yamamoto, T Shintomi, A Araya, S Takemoto, T Higashi, H Momose, J Akamatsu, and W Morii. Status of the clio project. *Classical and Quantum Gravity*, 21(5):S1173, feb 2004.

[113] EPTA Collaboration and InPTA Collaboration:, J Antoniadis, P Arumugam, S Arumugam, S Babak, M Bagchi, A-S Bak Nielsen, C G Bassa, A Bathula, and Berthereau *et al.* The second data release from the european pulsar timing array. *Astron. Astrophys.*, 678:A50, October 2023.

[114] Daniel J. Reardon, Andrew Zic, Ryan M. Shannon, George B. Hobbs, Matthew Bailes, Valentina Di Marco, Agastya Kapur, Axl F. Rogers, Eric Thrane, Jacob Askew, N. D. Ramesh Bhat, Andrew Cameron, Małgorzata Curyło, William A. Coles, Shi Dai, Boris Goncharov, Matthew Kerr, Atharva Kulkarni, Yuri Levin, Marcus E. Lower, Richard N. Manchester, Rami Mandow, Matthew T. Miles, Rowina S. Nathan, Stefan Osłowski, Christopher J. Russell, Renée Spiewak, Songbo Zhang, and Xing-Jiang Zhu. Search for an isotropic gravitational-wave background with the parkes pulsar timing array. *The Astrophysical Journal Letters*, 951(1):L6, jun 2023.

[115] Pratik Tarafdar, K Nobleson, Prerna Rana, Jaikhomba Singha, M. A. Krishnakumar, Bhal Chandra Joshi, Avinash Kumar Paladi, Neel Kolhe, Neelam Dhanda Batra, Nikita Agarwal, and et al. The indian pulsar timing array: First data release. *Publications of the Astronomical Society of Australia*, 39:e053, 2022.

[116] Seiji Kawamura, Masaki Ando, Naoki Seto, Shuichi Sato, Mitsuru Musha, Isao Kawano, Jun'ichi Yokoyama, Takahiro Tanaka, Kunihito Ioka, Tomotada Akutsu, Takeshi Takashima, Kazuhiro Agatsuma, Akito Araya, Naoki Aritomi, Hideki Asada, Takeshi Chiba, Satoshi Eguchi, Motohiro Enoki, Masa-Katsu Fujimoto, Ryuichi Fujita, Toshifumi Futamase, Tomohiro Harada, Kazuhiro Hayama, Yoshiaki Himemoto, Takashi Hiramatsu, Feng-Lei Hong, Mizuhiko Hosokawa, Kiyotomo Ichiki, Satoshi Ikari, Hideki Ishihara, Tomohiro Ishikawa, Yousuke Itoh, Takahiro Ito, Shoki Iwaguchi, Kiwamu Izumi, Nobuyuki Kanda, Shinya Kanemura, Fumiko Kawazoe, Shiho Kobayashi, Kazunori Kohri, Yasufumi Kojima, Keiko Kokeyama, Kei Kotake, Sachiko Kuroyanagi, Kei-ichi Maeda, Shuhei Matsushita, Yuta Michimura, Taigen Morimoto, Shinji Mukohyama, Koji Nagano, Shigeo Nagano, Takeo Naito, Kouji Nakamura, Takashi Nakamura, Hiroyuki Nakano, Kenichi Nakao, Shinichi Nakasuka, Yoshinori Nakayama, Kazuhiro Nakazawa, Atsushi Nishizawa, Masashi Ohkawa, Kenichi Oohara, Norichika Sago, Motoyuki Saijo, Masaaki Sakagami, Shinichiro Sakai, Takashi Sato, Masaru Shibata, Hisaaki Shinkai, Ayaka Shoda, Kentaro Somiya, Hajime Sotani, Ryutaro Takahashi, Hirotaka Takahashi, Takamori

Akiteru, Keisuke Taniguchi, Atsushi Taruya, Kimio Tsubono, Shinji Tsujikawa, Akitoshi Ueda, Ken-ichi Ueda, Izumi Watanabe, Kent Yagi, Rika Yamada, Shuichiro Yokoyama, Chul-Moon Yoo, and Zong-Hong Zhu. Current status of space gravitational wave antenna DECIGO and B-DECIGO. *Progress of Theoretical and Experimental Physics*, 2021(5):05A105, 02 2021.

[117] Jianwei Mei, Yan-Zheng Bai, Jiahui Bao, Enrico Barausse, Lin Cai, Enrico Canuto, Bin Cao, Wei-Ming Chen, Yu Chen, Yan-Wei Ding, Hui-Zong Duan, Huimin Fan, Wen-Fan Feng, Honglin Fu, Qing Gao, TianQuan Gao, Yungui Gong, Xingyu Gou, Chao-Zheng Gu, De-Feng Gu, Zi-Qi He, Martin Hendry, Wei Hong, Xin-Chun Hu, Yi-Ming Hu, Yuexin Hu, Shun-Jia Huang, Xiang-Qing Huang, Qinghua Jiang, Yuan-Ze Jiang, Yun Jiang, Zhen Jiang, Hong-Ming Jin, Valeriya Korol, Hong-Yin Li, Ming Li, Ming Li, Pengcheng Li, Rongwang Li, Yuqiang Li, Zhu Li, Zhulian Li, Zhu-Xi Li, Yu-Rong Liang, Zheng-Cheng Liang, Fang-Jie Liao, Qi Liu, Shuai Liu, Yan-Chong Liu, Li Liu, Pei-Bo Liu, Xuhui Liu, Yuan Liu, Xiong-Fei Lu, Yang Lu, Ze-Huang Lu, Yan Luo, Zhi-Cai Luo, Vadim Milyukov, Min Ming, Xiaoyu Pi, Chenggang Qin, Shao-Bo Qu, Alberto Sesana, Chenggang Shao, Changfu Shi, Wei Su, Ding-Yin Tan, Yujie Tan, Zhuangbin Tan, Liang-Cheng Tu, Bin Wang, Cheng-Rui Wang, Fengbin Wang, Guan-Fang Wang, Haitian Wang, Jian Wang, Lijiao Wang, Panpan Wang, Xudong Wang, Yan Wang, Yi-Fan Wang, Ran Wei, Shu-Chao Wu, Chun-Yu Xiao, Xiao-Shi Xu, Chao Xue, Fang-Chao Yang, Liang Yang, Ming-Lin Yang, Shan-Qing Yang, Bobing Ye, Hsien-Chi Yeh, Shenghua Yu, Dongsheng Zhai, Caishi Zhang, Haitao Zhang, Jian-dong Zhang, Jie Zhang, Lihua Zhang, Xin Zhang, Xuefeng Zhang, Hao Zhou, Ming-Yue Zhou, Ze-Bing Zhou, Dong-Dong Zhu, Tie-Guang Zi, and Jun Luo. The TianQin project: Current progress on science and technology. *Progress of Theoretical and Experimental Physics*, 2021(5):05A107, 08 2020.

[118] Wen-Hong Ruan, Zong-Kuan Guo, Rong-Gen Cai, and Yuan-Zhong Zhang. Taiji program: Gravitational-wave sources. *International Journal of Modern Physics A*, 35(17):2050075, June 2020.

[119] Curt Cutler and Daniel E. Holz. Ultrahigh precision cosmology from gravitational waves. *Phys. Rev. D*, 80:104009, Nov 2009.

[120] Xuefei Gong, Yun-Kau Lau, Shengnian Xu, Pau Amaro-Seoane, Shan Bai, Xing Bian, Zhoujian Cao, Gerui Chen, Xian Chen, Yanwei Ding, Peng Dong, Wei Gao, Gerhard Heinzel, Ming Li, Shuo Li, Fukun Liu, Ziren Luo, Mingxue Shao, Rainer Spurzem, Baosan Sun, Wenlin Tang, Yan Wang, Peng Xu, Pin Yu, Yefei Yuan, Xiaomin Zhang, and Zebing Zhou. Descope of the alia mission. *Journal of Physics: Conference Series*, 610(1):012011, apr 2015.

[121] C. S. Unnikrishnan. Ligo-india: A decadal assessment on its scope, relevance, progress, and future, 2023.

[122] L. Badurina, E. Bentine, D. Blas, K. Bongs, D. Bortoletto, T. Bowcock, K. Bridges, W. Bowden, O. Buchmueller, and C. Burrage *et al.* AION: an atom interferom-

eter observatory and network. *Journal of Cosmology and Astroparticle Physics*, 2020(05):011–011, may 2020.

[123] B. Canuel, A. Bertoldi, L. Amand, E. Pozzo di Borgo, T. Chantrait, C. Danquigny, M. Dovale Álvarez, B. Fang, A. Freise, and R. Geiger *et al.* Exploring gravity with the MIGA large scale atom interferometer. *Scientific Reports*, 8(1):14064, Sep 2018.

[124] B. Canuel *et al.* ELGAR—a european laboratory for gravitation and atom-interferometric research. *Classical and Quantum Gravity*, 37(22):225017, oct 2020.

[125] Abe Mahiro *et al.* Matter-wave atomic gradiometer interferometric sensor (MAGIS-100). *Quantum Science and Technology*, 6(4):044003, July 2021.

[126] Nancy Aggarwal, George P. Winstone, Mae Teo, Masha Baryakhtar, Shane L. Larson, Vicky Kalogera, and Andrew A. Geraci. Searching for new physics with a levitated-sensor-based gravitational-wave detector. *Phys. Rev. Lett.*, 128:111101, Mar 2022.

[127] Tomofumi Shimoda, Satoru Takano, Ching Pin Ooi, Naoki Aritomi, Ayaka Shoda, Yuta Michimura, and Masaki Ando. Torsion-bar antenna: a ground-based mid-frequency and low-frequency gravitational wave detector, 2019.

[128] Yeukuang Hwu and Giorgio Margaritondo. Synchrotron radiation and X-ray free-electron lasers (X-FELs) explained to all users, active and potential. *Journal of Synchrotron Radiation*, 28(3):1014–1029, May 2021.

[129] Helmut 1938 Wiedemann. *Particle Accelerator Physics*. Graduate texts in Physics. Springer, 4th ed. edition, 2015.

[130] Milton Stanley Livingston and John P. Blewett. *Particle Accelerators: From Big Bang Physics to Hadron Therapy*. World Scientific, 2014.

[131] Soontaree Seangsri, Thanasak Wanglomklang, Nopparut Khaewnak, Nattawat Yachum, and Jiraphon Srisertpol. Optimizing ultra-high vacuum control in electron storage rings using fuzzy control and estimation of pumping speed by neural networks with molflow+. *Systems*, 11(3), 2023.

[132] Alexander Gabovich. Vacuum technology in accelerators: State of the art and future prospects. *Physics-Uspekhi*, 62(5):487–501, 2019.

[133] VAC AERO International. The fundamentals of vacuum theory, 2018.

[134] J. P. Hobson. The future of vacuum technology. *Journal of Vacuum Science Technology A*, 2(2):144–149, 04 1984.

[135] Giacomo Apollinari, Oliver Brüning, Tiziano Camporesi, and Lucio Rossi. The high luminosity large hadron collider: The new machine for illuminating the mysteries of universe. *The European Physical Journal Plus*, 132(3):1–40, 2017.

[136] Helmut Wiedemann. *Particle Accelerator Physics*. Springer, 4 edition, 2015.

[137] Lucio Rossi and Ezio Todesco. High-temperature superconducting magnets for next generation storage rings. *IEEE Transactions on Applied Superconductivity*, 31(5), 2021.

[138] Patric Muggli and Tor O. Raubenheimer. Advances in beam cooling techniques. *Physical Review Accelerators and Beams*, 23(4):041002, 2020.

[139] S. Chatrchyan, V. Khachatryan, A.M. Sirunyan, A. Tumasyan, W. Adam, E. Aguilo, T. Bergauer, M. Dragicevic, J. Erö, C. Fabjan, and M. Friedl et al. Observation of a new boson at a mass of 125 gev with the cms experiment at the lhc. *Physics Letters B*, 716(1):30–61, 2012.

[140] G. Aad, T. Abajyan, B. Abbott, J. Abdallah, S. Abdel Khalek, A.A. Abdelalim, O. Abdinov, R. Aben, B. Abi, and M. Abolins et al. Observation of a new particle in the search for the standard model higgs boson with the atlas detector at the lhc. *Physics Letters B*, 716(1):1–29, 2012.

[141] Mark E. Johnson and Melissa A. Bell. Synchrotron radiation in environmental science: Detection of atmospheric particles. *Environmental Science Technology*, 52(12):6653–6660, 2018.

[142] Joris Dik et al. Revealing hidden details in cultural heritage objects with synchrotron radiation. *Journal of Synchrotron Radiation*, 25:1467–1471, 2018.

[143] Vladimir Shiltsev and Frank Zimmermann. Modern and future colliders. *Reviews of Modern Physics*, 93(1):015006, 2020.

[144] R. Joel England et al. Dielectric laser accelerators. *Reviews of Modern Physics*, 86(4):1337–1389, 2014.

[145] Suvrat Rao, Marcus Brüggen, and Jochen Liske. Detection of gravitational waves in circular particle accelerators. *Phys. Rev. D*, 102:122006, Dec 2020.

[146] B. S. Sathyaprakash and Bernard F. Schutz. Physics, astrophysics and cosmology with gravitational waves. *Living Reviews in Relativity*, 12(1):2, Dec 2009.

[147] Lyndon Evans and Philip Bryant. Lhc machine. *Journal of Instrumentation*, 3(08):S08001–S08001, Aug 2008.

[148] Felix A. E. Pirani. Republication of: On the physical significance of the riemann tensor. *General Relativity and Gravitation*, 41(5):1215–1232, May 2009.

[149] F. A. E. Pirani. Invariant formulation of gravitational radiation theory. *Phys. Rev.*, 105:1089–1099, Feb 1957.

[150] C. J. Moore, R. H. Cole, and Christopher Philip Luke Berry. Gravitational-wave sensitivity curves. *Classical and Quantum Gravity*, 32(1), January 2015.

[151] T. Mastorides, C. Rivetta, J. D. Fox, D. Van Winkle, and P. Baudrenghien. Rf system models for the cern large hadron collider with application to longitudinal dynamics. *Physical Review Special Topics - Accelerators and Beams*, 13(10):102801, Oct 2010.

[152] Scott A. Hughes and Kip S. Thorne. Seismic gravity-gradient noise in interferometric gravitational-wave detectors. *Phys. Rev. D*, 58:122002, Nov 1998.

[153] Kip S. Thorne and Carolee J. Winstein. Human gravity-gradient noise in interferometric gravitational-wave detectors. *Phys. Rev. D*, 60:082001, Sep 1999.

[154] L. Arnaudon, B. Dehning, A. Hofmann, P. Grosse-Wiesmann, R. Jacobsen, J. P. Koutchouk, J. Miles, R. Olsen, M. Placidi, and R. Schmidt *et al.* Effects of terrestrial tides on the lep beam energy. *Nuclear Instruments and Methods in Physics Research Section A: Accelerators, Spectrometers, Detectors and Associated Equipment*, 357(2):249–252, Apr 1995.

[155] E. Todesco and J. Wenninger. Large hadron collider momentum calibration and accuracy. *Physical Review Accelerators and Beams*, 20(8):081003, Aug 2017.

[156] Philippe Baudrenghien, Gregoire Hagmann, John Cornelis Molendijk, Ragnar Olsen, Anton Rohlev, Vittorio Rossi, Donat Stellfeld, Daniel Valuch, and Urs Wehrle. The LHC Low Level RF. (LHC-PROJECT-Report-906. CERN-LHC-Project-Report-906):4 p, Jul 2006. revised version submitted on 2006-08-28 14:51:11.

[157] Davide Gamba, Roberto Corsini, Michael Guinchard, Michaela Schaumann, and Jorg Wenninger. Estimated Impact of Ground Motion on HL-LHC Beam Orbit. (CERN-ACC-2018-132):THPAF040. 4 p, 2018.

[158] Ralph J Steinhagen, S Redaelli, and J Wenninger. Analysis of Ground Motion at SPS and LEP - Implications for the LHC. Technical Report CERN-AB-2005-087, CERN, Geneva, Nov 2005.

[159] L Vos. Effect of very low frequency ground motion on the LHC. (LHC-Project-Report-192. CERN-LHC-Project-Report-192):4 p, Jun 1998.

[160] L Vos. Ground motion in LEP and LHC; 1994 ed. *Part. Accel.*, 50(CERN-SL-94-69-BI. LHC-NOTE-299. CERN-LHC-Note-299):221–231. 19 p, Nov 1994.

[161] T. Accadia *et al.* and Virgo Collaboration. The seismic superattenuators of the virgo gravitational waves interferometer. *Journal of Low Frequency Noise, Vibration and Active Control*, 30(1):63–79, Mar 2011.

[162] S. Baron, T. Mastoridis, J. Troska, and P. Baudrenghien. Jitter impact on clock distribution in lhc experiments. *Journal of Instrumentation*, 7(12):C12023–C12023, Dec 2012.

[163] A. Jeff, M. Andersen, A. Boccardi, S. Bozyigit, E. Bravin, T. Lefevre, A. Rabiller, F. Roncarolo, C. P. Welsch, and A. S. Fisher. Longitudinal density monitor for the lhc. *Phys. Rev. ST Accel. Beams*, 15:032803, Mar 2012.

[164] Boris Korzh, Qing-Yuan Zhao, Jason P. Allmaras, Simone Frasca, Travis M. Autry, Eric A. Bersin, Andrew D. Beyer, Ryan M. Briggs, Bruce Bumble, and Marco Colangelo *et al.* Demonstration of sub-3 ps temporal resolution with a superconducting nanowire single-photon detector. *Nature Photonics*, 14(4):250–255, Apr 2020.

[165] W. Zhang, J. Huang, C. Zhang, L. You, C. Lv, L. Zhang, H. Li, Z. Wang, and X. Xie. A 16-pixel interleaved superconducting nanowire single-photon detector array with a maximum count rate exceeding 1.5 ghz. *IEEE Transactions on Applied Superconductivity*, 29(5):1–4, 2019.

[166] Hiroyuki Shibata, Kaoru Shimizu, Hiroki Takesue, and Yasuhiro Tokura. Ultimate low system dark-count rate for superconducting nanowire single-photon detector. *Optics Letters*, 40(14):3428–3431, Jul 2015.

[167] Dileep V. Reddy, Adriana E. Lita, Sae Woo Nam, Richard P. Mirin, and Varun B. Verma. Achieving 98% system efficiency at 1550 nm in superconducting nanowire single photon detectors. In *Rochester Conference on Coherence and Quantum Optics (CQO-11)*, OSA Technical Digest, page W2B.2, Rochester, New York, Aug 2019. Optical Society of America.

[168] Iman Esmaeil Zadeh, Johannes W. N. Los, Ronan B. M. Gourgues, Violette Steinmetz, Gabriele Bulgarini, Sergiy M. Dobrovolskiy, Val Zwiller, and Sander N. Dorenbos. Single-photon detectors combining high efficiency, high detection rates, and ultra-high timing resolution. *APL Photonics*, 2(11):111301, Nov 2017.

[169] Hao Li, Yong Wang, Lixing You, Heqing Wang, Hui Zhou, Peng Hu, Weijun Zhang, Xiaoyu Liu, Xiaoyan Yang, and Lu Zhang *et al.* . Supercontinuum single-photon detector using multilayer superconducting nanowires. *Photonics Research*, 7(12):1425–1431, Dec 2019.

[170] T. Polakovic, W. R. Armstrong, V. Yefremenko, J. E. Pearson, K. Hafidi, G. Karapetrov, Z.-E. Meziani, and V. Novosad. Superconducting nanowires as high-rate photon detectors in strong magnetic fields. *Nuclear Instruments and Methods in Physics Research Section A: Accelerators, Spectrometers, Detectors and Associated Equipment*, 959:163543, Apr 2020.

[171] G. Edward Marti, Ross B. Hutson, Akihisa Goban, Sara L. Campbell, Nicola Poli, and Jun Ye. Imaging optical frequencies with $100\ \mu\mathrm{Hz}$ precision and $1.1\ \mu\mathrm{m}$ resolution. *Phys. Rev. Lett.*, 120:103201, Mar 2018.

[172] A. Berlin, M. Brüggen, O. Buchmueller, P. Chen, R. T. D'Agnolo, R. Deng, J. R. Ellis, S. Ellis, G. Franchetti, and A. Ivanov *et al.* Storage rings and gravitational waves: Summary and outlook, 2021.

[173] B. P. Abbott *et al.*, LIGO Scientific Collaboration, Virgo Collaboration, and KAGRA Collaboration. Prospects for observing and localizing gravitational-wave transients with advanced ligo, advanced virgo and kagra. *Living Reviews in Relativity*, 21(1):3, Apr 2018.

[174] Wen-Hong Ruan, Chang Liu, Zong-Kuan Guo, Yue-Liang Wu, and Rong-Gen Cai. The lisa–taiji network. *Nature Astronomy*, 4(2):108–109, Feb 2020.

[175] Suvrat Rao, Julia Baumgarten, Jochen Liske, and Marcus Brüggen. Detection of gravitational waves in circular particle accelerators ii. response analysis and parameter estimation using synthetic data, 2023.

[176] D Zer-Zion. On the detection of gravitational waves through their interaction with particles in storage rings. Technical report, CERN, Geneva, Mar 1998.

[177] J. W. van Holten. Cyclotron motion in a gravitational-wave background, 1999.

[178] A. N. Ivanov, A. P. Kobushkin, and M. Wellenzohn. Storage rings as detectors for relic gravitational-wave background ?, 2002.

[179] D. Dong. Study of Charged Particle Storage Ring as Detector of Gravitational Waves. *eConf*, C0211115:030, 2002.

[180] Manfried Faber and Martin Suda. Influence of gravitational waves on circular moving particles. *Journal of Modern Physics*, 09(04):651–668, 2018.

[181] Pravin Kumar Dahal. Review of pulsar timing array for gravitational wave research. *Journal of Astrophysics and Astronomy*, 41(1), March 2020.

[182] Remi Geiger. Future gravitational wave detectors based on atom interferometry. In *An Overview of Gravitational Waves*, pages 285–313. WORLD SCIENTIFIC, February 2017.

[183] D Habs and R Grimm. Crystalline ion beams. *Annual Review of Nuclear and Particle Science*, 45(1):391–428, December 1995.

[184] T. Schätz, U. Schramm, and D. Habs. Crystalline ion beams. *Nature*, 412(6848):717–720, August 2001.

[185] U. Schramm, T. Schätz, and D. Habs. Bunched crystalline ion beams. *Phys. Rev. Lett.*, 87:184801, Oct 2001.

[186] Sergei Nagaitsev, Anatoli Arodzero, Ihar Lobach, Alex Murokh, Alexander Romanov, Marcos Ruelas, Timur Shaftan, and Giulio Stancari. Experimental study of a single electron in a storage ring via undulator radiation. In *Proc. 10th International Particle Accelerator Conference (IPAC'19), Melbourne, Australia, 19-24 May 2019*, number 10 in International Particle Accelerator Conference, pages 781–784, Geneva, Switzerland, Jun. 2019. JACoW Publishing. https://doi.org/10.18429/JACoW-IPAC2019-MOPRB089.

[187] Josef Frisch. Beam Arrival Time Monitors. In *4th International Beam Instrumentation Conference*, page TUALA01, 2016.

[188] J. Weber. Observation of the thermal fluctuations of a gravitational-wave detector. *Phys. Rev. Lett.*, 17:1228–1230, Dec 1966.

[189] J. Weber. Gravitational radiation. *Phys. Rev. Lett.*, 18:498–501, Mar 1967.

[190] E. Mauceli, Z. K. Geng, W. O. Hamilton, W. W. Johnson, S. Merkowitz, A. Morse, B. Price, and N. Solomonson. The Allegro gravitational wave detector: Data acquisition and analysis. *Phys. Rev. D*, 54:1264–1275, Jul 1996.

[191] Suvrat Rao. Storage Ring Gravitational-wave Observatory (SRGO) simulation code, doi:10.5281/zenodo.7485016, 12 2022.

[192] Luc Blanchet, Bala R Iyer, Clifford M Will, and Alan G Wiseman. Gravitational waveforms from inspiralling compact binaries to second-post-newtonian order. *Classical and Quantum Gravity*, 13(4):575–584, apr 1996.

[193] Ue-Li Pen. Analytical fit to the luminosity distance for flat cosmologies with a cosmological constant. *The Astrophysical Journal Supplement Series*, 120(1):49–50, jan 1999.

[194] Eric Thrane and Colm Talbot. An introduction to bayesian inference in gravitational-wave astronomy: Parameter estimation, model selection, and hierarchical models. *Publications of the Astronomical Society of Australia*, 36:e010, 2019.

[195] P.V. Ubale. Numerical solution of boole's rule in numerical integration by using general quadrature formula. *The Bulletin of Society for Mathematical Services and Standards*, 2:1–4, June 2012.

[196] Don van Ravenzwaaij, Pete Cassey, and Scott D. Brown. A simple introduction to markov chain monte–carlo sampling. *Psychonomic Bulletin & Review*, 25(1):143–154, March 2016.

[197] Joshua S. Speagle. A conceptual introduction to markov chain monte carlo methods, 2019.

[198] David Luengo, Luca Martino, Mónica Bugallo, Víctor Elvira, and Simo Särkkä. A survey of monte carlo methods for parameter estimation. *EURASIP Journal on Advances in Signal Processing*, 2020(1), May 2020.

[199] Cajo J. F. Ter Braak. A markov chain monte carlo version of the genetic algorithm differential evolution: easy bayesian computing for real parameter spaces. *Statistics and Computing*, 16(3):239–249, Sep 2006.

[200] John Salvatier, Thomas V. Wiecki, and Christopher Fonnesbeck. Probabilistic programming in python using PyMC3. *PeerJ Computer Science*, 2:e55, April 2016.

[201] Pourbaix, D., Tokovinin, A. A., Batten, A. H., Fekel, F. C., Hartkopf, W. I., Levato, H., Morrell, N. I., Torres, G., and Udry, S. Sb9: The ninth catalogue of spectroscopic binary orbits. *A&A*, 424(2):727–732, 2004.

[202] T. Prusti *et al.*, Gaia Collaboration. The gaia mission. *A&A*, 595:A1, 2016.

[203] C. Babusiaux, C. Fabricius, S. Khanna, T. Muraveva, C. Reylé, F. Spoto, and A. Vallenari. Gaia data release 3. catalogue validation. *A&A*, June 2022.

[204] A. Vallenari, A.G.A. Brown, and T. Prusti. Gaia data release 3. Summary of the content and survey properties. *A&A*, June 2022.

[205] Nicholas Farrow, Xing-Jiang Zhu, and Eric Thrane. The mass distribution of galactic double neutron stars. *The Astrophysical Journal*, 876(1):18, apr 2019.

[206] T. M. Tauris, M. Kramer, P. C. C. Freire, N. Wex, H.-T. Janka, N. Langer, Ph. Podsiadlowski, E. Bozzo, S. Chaty, and M. U. Kruckow *et al.* Formation of double neutron star systems. *The Astrophysical Journal*, 846(2):170, sep 2017.

[207] A D Cameron, D J Champion, M Kramer, M Bailes, E D Barr, C G Bassa, S Bhandari, N D R Bhat, M Burgay, and S Burke-Spolaor *et al.* The High Time Resolution Universe Pulsar Survey – XIII. PSR J17571854, the most accelerated binary pulsar. *Monthly Notices of the Royal Astronomical Society: Letters*, 475(1):L57–L61, 01 2018.

[208] K. Stovall, P. C. C. Freire, S. Chatterjee, P. B. Demorest, D. R. Lorimer, M. A. McLaughlin, N. Pol, J. van Leeuwen, R. S. Wharton, and B. Allen *et al.* PALFA discovery of a highly relativistic double neutron star binary. *The Astrophysical Journal*, 854(2):L22, feb 2018.

[209] Ryan S. Lynch, Joseph K. Swiggum, Vlad I. Kondratiev, David L. Kaplan, Kevin Stovall, Emmanuel Fonseca, Mallory S. E. Roberts, Lina Levin, Megan E. DeCesar, and B. Cui *et al.* The Green Bank North Celestial Cap pulsar survey. III. 45 new pulsar timing solutions. *The Astrophysical Journal*, 859(2):93, may 2018.

[210] David L. Kaplan, Jason Boyles, Bart H. Dunlap, Shriharsh P. Tendulkar, Adam T. Deller, Scott M. Ransom, Maura A. McLaughlin, Duncan R. Lorimer, and Ingrid H. Stairs. A $1.05 m_\odot$ companion to PSR J2222—0137: The coolest known white dwarf? *The Astrophysical Journal*, 789(2):119, jun 2014.

[211] A. G. Lyne, M. Burgay, M. Kramer, A. Possenti, R.N. Manchester, F. Camilo, M. A. McLaughlin, D. R. Lorimer, N. D'Amico, and B. C. Joshi *et al.* A double-pulsar system: A rare laboratory for relativistic gravity and plasma physics. *Science*, 303(5661):1153–1157, 2004.

[212] M. Kramer, I. H. Stairs, R. N. Manchester, N. Wex, A. T. Deller, W. A. Coles, M. Ali, M. Burgay, F. Camilo, and I. Cognard *et al.* Strong-field gravity tests with the double pulsar. *Phys. Rev. X*, 11:041050, Dec 2021.

[213] A Lamberts, S Garrison-Kimmel, P F Hopkins, E Quataert, J S Bullock, C-A Faucher-Giguère, A Wetzel, D Kereš, K Drango, and R E Sanderson. Predicting the binary black hole population of the Milky Way with cosmological simulations. *Monthly Notices of the Royal Astronomical Society*, 480(2):2704–2718, 07 2018.

[214] Alberto Sesana, Astrid Lamberts, and Antoine Petiteau. Finding binary black holes in the Milky Way with LISA. *Monthly Notices of the Royal Astronomical Society: Letters*, 494(1):L75–L80, 03 2020.

[215] Kailash C. Sahu, Jay Anderson, Stefano Casertano, Howard E. Bond, Andrzej Udalski, Martin Dominik, Annalisa Calamida, Andrea Bellini, Thomas M. Brown, and M. Rejkuba *et al.* An isolated stellar-mass black hole detected through astrometric microlensing*. *The Astrophysical Journal*, 933(1):83, jul 2022.

[216] Angelo Ricarte, Michael Tremmel, Priyamvada Natarajan, and Thomas Quinn. Unveiling the population of wandering black holes via electromagnetic signatures. *The Astrophysical Journal Letters*, 916(2):L18, aug 2021.

[217] Event Horizon Telescope Collaboration and Kazunori Akiyama *et al.* First sagittarius a* event horizon telescope results. i. the shadow of the supermassive black hole in the center of the milky way. *The Astrophysical Journal Letters*, 930(2):L12, may 2022.

[218] Emanuele Berti. LISA observations of massive black hole mergers: event rates and issues in waveform modelling. *Classical and Quantum Gravity*, 23(19):S785–S797, sep 2006.

[219] Ralf Bender, John Kormendy, Gary Bower, Richard Green, Jens Thomas, Anthony C. Danks, Theodore Gull, J. B. Hutchings, C. L. Joseph, M. E. Kaiser, Tod R. Lauer, Charles H. Nelson, Douglas Richstone, Donna Weistrop, and Bruce Woodgate. Hst stis spectroscopy of the triple nucleus of m31: Two nested disks in keplerian rotation around a supermassive black hole. *The Astrophysical Journal*, 631(1):280, sep 2005.

[220] Andrea Merloni and Sebastian Heinz. A synthesis model for AGN evolution: supermassive black holes growth and feedback modes. *Monthly Notices of the Royal Astronomical Society*, 388(3):1011–1030, 07 2008.

[221] Mélanie Habouzit, Yuan Li, Rachel S Somerville, Shy Genel, Annalisa Pillepich, Marta Volonteri, Romeel Davé, Yetli Rosas-Guevara, Stuart McAlpine, and Peirani Sébastien *et al.* Supermassive black holes in cosmological simulations I: MBH – $M_\star$ relation and black hole mass function. *Monthly Notices of the Royal Astronomical Society*, 503(2):1940–1975, 02 2021.

[222] Alex Sicilia, Andrea Lapi, Lumen Boco, Francesco Shankar, David M. Alexander, Viola Allevato, Carolin Villforth, Marcella Massardi, Mario Spera, and Alessandro Bressan *et al.* The black hole mass function across cosmic time. II. heavy seeds and (super)massive black holes. *The Astrophysical Journal*, 934(1):66, jul 2022.

[223] Karina T. Voggel, Anil C. Seth, Holger Baumgardt, Bernd Husemann, Nadine Neumayer, Michael Hilker, Renuka Pechetti, Steffen Mieske, Antoine Dumont, and Iskren Georgiev. First direct dynamical detection of a dual supermassive black hole system at sub-kiloparsec separation. *A&A*, 658:A152, 2022.

[224] Peter R. Saulson. Gravitational wave detection: Principles and practice. *Comptes Rendus Physique*, 14(4):288–305, 2013. Gravitational waves / Ondes gravitationnelles.

[225] Renjie Wang and Bin Hu. Litepig: A lite parameter inference system for the gravitational wave in the millihertz band, 2022.

[226] Vijay Varma, Ryuichi Fujita, Ashok Choudhary, and Bala R. Iyer. Comparison of post-newtonian templates for extreme mass ratio inspirals. *Phys. Rev. D*, 88:024038, Jul 2013.

[227] Carl L. Rodriguez, Benjamin Farr, Will M. Farr, and Ilya Mandel. Inadequacies of the fisher information matrix in gravitational-wave parameter estimation. *Phys. Rev. D*, 88:084013, Oct 2013.

[228] G. Bernardi, E. Brost, D. Denisov, G. Landsberg, M. Aleksa, D. d'Enterria, P. Janot, M. L. Mangano, M. Selvaggi, and Frank Zimmermann *et al.* The future circular collider: a summary for the us 2021 snowmass process, 2022.

[229] L. Piro, M. Colpi, J. Aird, A. Mangiagli, A. C. Fabian, M. Guainazzi, S. Marsat, A. Sesana, P. McNamara, and M. Bonetti *et al.* Chasing super-massive black hole merging events with $athena$ and lisa, 2022.

[230] John Baker, Zoltan Haiman, Elena Maria Rossi, Edo Berger, Niel Brandt, Elme Breedt, Katelyn Breivik, Maria Charisi, Andrea Derdzinski, and Daniel J. D'Orazio *et al.* Multimessenger science opportunities with mHz gravitational waves. *Bulletin of the AAS*, 51(3), may 31 2019. https://baas.aas.org/pub/2020n3i123.

[231] Michael Eracleous, Suvi Gezari, Alberto Sesana, Tamara Bogdanovic, Morgan MacLeod, Nathaniel Roth, and Lixin Dai. An Arena for Multi-Messenger Astrophysics: Inspiral and Tidal Disruption of White Dwarfs by Massive Black Holes. *Bulletin of the AAS*, 51(3), may 31 2019. https://baas.aas.org/pub/2020n3i010.

[232] Mark B. Villarino. Ramanujan's perimeter of an ellipse, 2005.

[233] Hanno Essén and Miguel C. N. Fiolhais. Meissner effect, diamagnetism, and classical physics—a review. *American Journal of Physics*, 80(2):164–169, 02 2012.

[234] Marc Favata. The gravitational-wave memory effect. *Classical and Quantum Gravity*, 27(8):084036, apr 2010.